FIRST-PRINCIPLES STUDY OF ELECTRONIC STRUCTURE AND DEFECT PHYSICS IN PHOTOVOLTAIC AND NEUROMORPHIC MATERIALS

A Dissertation

by

BAIYU ZHANG

Submitted to the Office of Graduate and Professional Studies of
Texas A&M University
in partial fulfillment of the requirements for the degree of

DOCTOR OF PHILOSOPHY

Chair of Committee,	Xiaofeng Qian
Committee Members,	Tahir Cagin
	Hong-Cai Joe Zhou
	Zi Jing Wong
Head of Department,	Ibrahim Karaman

May 2021

Major Subject: Materials Science and Engineering

Copyright 2021 Baiyu Zhang

ABSTRACT

The last decade has witnessed the increasing demand for renewable energy and new information technology, largely due to the reduction in the conventional non-renewable energy resources and the von Neumann bottleneck in the classical computing architecture for data storage, transfer, and processing. While a wide range of materials have been explored for thin-film photovoltaics, each of these solar absorbers suffers from different kinds of issues. In contrast, initial neural circuits based on conventional complementary metal-oxide-semiconductor processors are energy inefficient for neuromorphic computing. Materials with dynamic behavior such as nonlinear conductance switch could directly emulate neural elements.

In this dissertation, the fundamental physical and chemical properties of several emerging functional materials were investigated, including quasi-one-dimensional antimony chalcogenides as solar absorbers for photovoltaic applications, and strongly correlated transition metal oxides and two-dimensional transition metal dichalcogenides as phase-change materials for neuromorphic computing. The competing superior electronic structure and complex defect chemistry in antimony chalcogenides were systematically studied. Furthermore, antimony chalcogenide thin-film solar cell via close space sublimation is compatible with the current thin-film manufacturing process. The power conversion efficiency of Sb_2Se_3 with graphite as electrodes has been improved from 4% to 7% via interfacial engineering.

The second part of the dissertation is focused on the fundamental understanding and rational design of neuromorphic materials using first-principles approaches. Comprehensive study has demonstrated VO_2 devices closely emulated neural circuits due to the metal-insulator transition (MIT). However, the mechanism of its MIT is still under debate and the phase transition temperature is too low for practical applications. To understand the MIT in VO_2, we studied the structural, electronic and magnetic properties of both the semiconducting (M1) and metallic (R) phases based on different DFT functionals. We then investigated the intrinsic and extrinsic defects in M1 VO_2. Based on theoretical findings, we rationalized materials design rule for further modulating its transition temperature in VO_2. The last part of the dissertation is focused on the theoretical study on the few-layer transition metal dichalcogenides, where we revealed the role of interlayer sliding in the piezoelectric and ferroelectric effect in 2D semimetals with potential application in low-power neuromorphic computing.

DEDICATION

This dissertation is dedicated to my grandmother, who is forever alive in our love.

ACKNOWLEDGEMENTS

First and foremost, I would like to express my deep and sincere thanks to my supervisor Dr. Xiaofeng Qian for his invaluable guidance, unlimited encouragement, continuous support, and endless patience during the past 5 years. His dynamism, vision, high academic standards, and motivation have inspired me in all the time of my academic research and daily life. He not only sets up a positive example in science, but also taught me the methodology to carry out the research. It was such a great privilege to work and study under his supervision. Hopefully, his deep insights on scientific problems would pass on me.

I would like to thank my committee members, Prof. Tahir Cagin, Prof. Hong-Cai Joe Zhou, and Prof. Zi Jing Wong. I wouldn't have gone this far without their help and guidance. Their encouragement, insightful comments and guidance benefit me a lot for the completion and success of this study.

I am very grateful to Prof. Sarbajit Banerjee, Prof. Patrick Shamberger, Prof. Matt Pharr, Prof. Feng Yan, Prof. Michael J. Demkowicz, Prof. Jingshan Qi, Liping Guo, Erick Braham, and Diane Sellers for all the insightful discussions and wonderful collaborations.

Thanks also go to my lab mates: Dr. Hua Wang, Daniel Willhelm, Nathan Wilson, Dr. Yang Yang, Xiuyu Tang, Alex Strasser, and Jaybelle Dannah Pranada. I wouldn't be able to work in a warm and family-like vibes without any of you. I'm also very grateful for support by Shangran Qiu, Mark Miao, and Chenyue Liu. Although we now have different aims in life, I will always cherish the time spent with all of you.

Last but by no means the least, as cliché as it may sound, this journey would really not be possible without the support and understanding of my family: my parents, my grandparents, my aunts, and my younger cousins. They provided me with not only financial supports that have allowed me to explore life and gain knowledge abroad, but also the mental strength that I sought during many tough times. Their enduring encouragement, and positive belief in my success keep me going regardless of the challenges and obstacles that I come across. My three little cousins fill my life with sunshine, joy and love. I still remember when I was in high school, my uncle Dr. Fucheng Zhang led me to his materials science lab. Watching him doing the research and operating the experimental facilities, I have been intrigued by the fascinating world of materials science and decided to pursue my career in this field, despite my having to find my own path at times. I appreciate his enduring support and guidance throughout every stage of my life. No matter how far I go in life, my research work will always be less important than the love of my family, and even less important than every meal they cooked for me when I was a little child.

CONTRIBUTORS AND FUNDING SOURCES

Contributors

This work was supervised by a dissertation committee consisting of Professor Xiaofeng Qian (advisor) of the Department of Materials Science and Engineering, Professor Tahir Cagin (member) of the Department of Materials Science and Engineering, Professor Hong-Cai Joe Zhou (member), joint appointed in the Department of Chemistry and the Department of Materials Science and Engineering, and Professor Zi Jing Wong (member), joint appointed in the Department of Aerospace Engineering and the Department of Materials Science and Engineering.

The experimental work in Chapter 3, including thin-film deposition and characterization and solar cell device fabrication and measurement (except the SIMS study), were conducted by Professor Feng Yan's group in the Department of Metallurgical and Materials Engineering at the University of Alabama. The theoretical investigation of B-doped VO_2 configurations and relative total energies in Chapter 4 was conducted by Dr. Ruben Villarreal in the Department of Mechanical Engineering at Texas A&M University. All other work conducted for the dissertation was completed by myself independently.

Funding Sources

Graduate study was supported by Texas A&M University President's Excellence Fund X-Grants Program, T3 Program, and NSF under Award Number DMR-1753054. Theoretical calculations were carried out at the advanced computing resources provided by Texas A&M High Performance Research Computing.

NOMENCLATURE

1D	One-Dimensional
2D	Two-Dimensional
3D	Three-Dimensional
ALD	Atomic Layer Deposition
ANNs	Artificial Neural Networks
BEC	Born Effective Charge
CBM	Conduction Band Minimum
CIGS	Copper Indium Gallium Selenide
CMOS	Complementary Metal-Oxide-Semiconductor
CSS	Close Space Sublimation
CZTS	Copper Zinc Tin Sulfide
DFT	Density Functional Theory
DOS	Density of States
EQE	External Quantum Efficiency
ETL	Electron Transport Layer
FeFET	Ferroelectric Field Effect Transistor
FF	Fill Factor
GGA	Generalized Gradient Approximation
HSE	Heyd-Scuseria-Ernzerhof
HTL	Hole Transport Layer

*h*BN	Hexagonal Boron Nitride
J_{sc}	Short Circuit Current
mBJ	Modified Becke-Johnson
MIT	Metal-to-Insulator Transition
ML	Machine Learning
PAW	Projector Augmented Wave
PBE	Perdew-Burke-Ernzerhof
PCE	Power Conversion Efficiency
PCMs	Phase-Change Materials
PV	Photovoltaics
R_{oc}	Series Resistance
R_{sh}	Shunt Resistance
RTE	Rapid Thermal Evaporation
T_c	Transition Temperature
TMDCs	Transition Metal Dichalcogenides
SPT	Structural Phase Transition
VASP	Vienna Ab initio Simulation Package
VBM	Valance Band Maximum
vdW	van der Waals
V_{oc}	Open-Circuit Voltage
VTD	Vapor Transport Deposition

TABLE OF CONTENTS

Page

ABSTRACT ii

DEDICATION iv

ACKNOWLEDGEMENTS v

CONTRIBUTORS AND FUNDING SOURCES vii

NOMENCLATURE viii

TABLE OF CONTENTS x

LIST OF FIGURES xiii

LIST OF TABLES xviii

1. INTRODUCTION 1

1.1. Thin-Film Solar Cells 2
1.1.1. Introduction of Thin-Film Solar Cells 2
1.1.2. Antimony Chalcogenide Thin-Film Solar Cells 3
1.2. Neuron-Inspired Computing 4
1.2.1. Introduction of Neuromorphic Computing 4
1.2.2. Phase-Change VO_2 as Potential Neuromorphic Materials 6
1.2.3. 2D Materials as Potential Neuromorphic Materials 6

2. FIRST-PRINCIPLES METHODS FOR POINT DEFECT CALCULATIONS 8

2.1. Defect Formation Energy 8
2.2. Supercell Approach for Dilute Limit 9
2.3. Transition Levels of Charged Defect 10
2.4. Equilibrium Fermi Level, Defect Concentration, and Carrier Density 11

3. ANTIMONY CHALCOGENIDES THIN-FILM PHOTOVOLTAICS 13

3.1. Electronic Structures and Defect Chemistry in Antimony Chalcogenides 13
3.1.1. Introduction 13
3.1.2. Computational Details 16
3.1.3. Crystal and Electronic Structure of Quasi-1D Antimony Chalcogenides 17

3.1.4. Anisotropic Dielectric Properties of Quasi-1D Antimony Chalcogenides 20
3.1.5. Low Exciton Binding Energy for Efficient Electron-Hole Separation 22
3.1.6. Defect Formation Energy and Transition Levels 24
3.1.7. Defect Concentration, Carrier Density, and Their Implication on *p*-/*n*-Typeness 30
3.1.8. Conclusions 33
3.2. Impact of Quasi-1D Nature on Photovoltaic Performance 35
3.2.1. Introduction 35
3.2.2. Computational Details 36
3.2.3. Orientation-Dependent Transport Behavior and Optical Absorption 36
3.2.4. Orientation-Dependent Device Performance 39
3.2.5. Conclusions 41
3.3. Interface Engineering via Sputtered Oxygenated CdS:O Window Layer..........42
3.3.1. Introduction 42
3.3.2. Computational Details 45
3.3.3. Interdiffusion and Defect Chemistry Associated with CdS:O 46
3.3.4. Improved Device Performance with Sputtered Oxygenated CdS:O 51
3.3.5. Conclusions 56
3.4. Sb_2S_3 Solar Cell Device Performance 57
3.4.1. Introduction 57
3.4.2. Electronic Structure and Optical Property from First-Principles Calculations 58
3.4.3. Performance of CSS-Deposited Sb_2S_3 Solar Cells..........59
3.4.4. Conclusions 60

4. PHASE-CHANGE VANADIUM DIOXIDES FOR NEUROMORPHIC COMPUTING 62

4.1. Introduction 62
4.1.1. Crystal Structure of Vanadium Dioxides 63
4.1.2. Phase Transition Mechanism: Peierls vs. Mott Scenarios..........64
4.1.3. Modulation of MIT in VO_2 68
4.1.4. Application of VO_2 in Neuromorphic Computing..........68
4.2. Assessment of DFT Functionals for Predictions of VO_2 Properties 69
4.3. Native Defects in M1 VO_2 73
4.4. Extrinsic Doping in VO_2 76
4.4.1. Extrinsic Defects in B-doped VO_2 77
4.4.2. Extrinsic Defects in Ge-doped VO_2 84
4.5. Conclusions 85

5. FERROELECTRIC AND PIEZOELECTRIC FEW-LAYER TRANSITION METAL DICHALCOGENIDES 87

5.1. Ferroelectric Materials for Neuro-Inspired Computing 87

5.2. Ferroelectricity in Few-Layer WTe_2 88
5.2.1. Origin of Ferroelectricity in Few-Layer WTe_2 from Group Theory 88
5.2.2. Ferroelectric Transition in Few-Layer WTe_2 90
5.3. Piezoelectricity in Few-Layer WTe_2 91
5.3.1. Piezoelectricity in 2D Materials 91
5.3.2. Polarization Change Upon Out-of-Plane Strain 93
5.4. Conclusions and Outlook 99

6. SUMMARY AND OUTLOOK 101

REFERENCES 104

LIST OF FIGURES

Page

Figure 1.1. A typical thin-film solar cell device structure, with a metal electrode, a hole (HTL) and electron transport layer (ETL), and a glass substrate. 3

Figure 3.1. (a) Crystal structure of antimony chalcogenides Sb_2Se_3 and Sb_2S_3. (b) and (d) Calculated electronic band structures of Sb_2Se_3 and Sb_2S_3. Red circles indicate VBM and CBM. (c) Calculated optical absorption spectra. 18

Figure 3.2. Defect formation energy diagrams of Sb_2Se_3 under (a) Se rich and (b) Se poor conditions. (c) Defect transition levels in Sb_2Se_3. The formation energies of native point defects in Sb_2Se_3 is plotted as a function of the Fermi level with VBM as reference. The bandgap adopted here is calculated by HSE06. The slope of each line indicates the most favorable charge state at the corresponding Fermi level. Positive and negative charge state indicate the donor and acceptor, respectively. The red and blue colors in (c) indicate the donor and acceptor transition levels, respectively. 26

Figure 3.3. Defect formation energy diagrams of Sb_2S_3 under (a) S rich and (b) S poor conditions. (c) Defect transition levels in Sb_2S_3. The formation energies of native point defects in Sb_2S_3 are plotted as a function of the Fermi level with VBM as reference. The bandgap adopted here is calculated by HSE06. The red and blue colors in (c) indicate the donor and acceptor transition levels, respectively. 28

Figure 3.4. Atomic structures of V_{Se2} with +1 and +2 charge states, respectively. The color of the atoms indicates the electron depletion (blue) or accumulation (red) with respect to V_{Se2} with +0 and +1 charge states. 29

Figure 3.5. (a) and (c) Fermi level of Sb_2Se_3 at synthesis and equilibrium temperatures as a function of synthesis temperature under Se rich and Se poor conditions, respectively. (b) and (e) Electron and hole densities at equilibrium temperature as a function of synthesis temperature under Se rich and Se poor conditions, respectively. (c) and (f) The concentration of dominant defects as a function of synthesis temperature under Se rich and Se poor conditions, respectively. The dashed line indicates the melting temperature of Sb_2Se_3 at 885 K. 31

Figure 3.6. (a) and (c) Fermi level of Sb_2S_3 at synthesis and equilibrium temperatures as a function of synthesis temperature under S rich and S poor conditions, respectively. (b) and (e) Electron and hole densities at equilibrium temperature as a function of synthesis temperature under S rich and S poor conditions, respectively. (c) and (f) Concentration of dominant defects as a

function of synthesis temperature under S rich and S poor conditions, respectively. The dashed line indicates the melting temperature of Sb_2S_3 at 823 K. 32

Figure 3.7. Sb_2Se_3 van der Waals crystals with tunable ribbons $(Sb_4Se_6)_n$ showing anisotropic transport behavior. (a) and (b) Atomic configuration from the side and top view, respectively. (c)-(e) Atomic structures of [120]-, [211]-, and [221]-oriented Sb_2Se_3 ribbons on the CdS-coated FTO glass substrate. (f) and (g) Comparison between [211]- and [221]-oriented grains on CdS substrate. The ribbons in the [211]-oriented grains are aligned closer to the plane normal compared to the ribbons in the [221]-oriented ones, suggesting a more facile carrier transport along [211]-oriented grains. 38

Figure 3.8. Orientation-dependent optical absorption coefficient from (a) theoretical calculations, and (b) UV-vis absorbance spectra for the films with [120]-, [221]-, and [211]-oriented grains. 39

Figure 3.9. Device performance of the Sb_2Se_3 cells. (a) Schematic solar cell geometry. (b) Energy level diagram of the layers in the cells. (c) and (d) the current density-voltage (J-V curve) and EQE spectra of the orientation dependent films. The inset of (c) illustrates the films with different ribbon orientation. The inset of (d) shows the histogram of device efficiencies from various fabricated devices. 41

Figure 3.10. Calculated Cd and O diffusion pathways and energy barriers in Sb_2Se_3. (a) Cd and (b) O diffusion along with ribbons. (c) Diffusion energy barrier along with ribbons. (d) Cd and (e) O diffusion across ribbons. (f) Diffusion energy barrier across ribbons. Symmetrically inequivalent Sb and Se sites are labeled in (e), including Sb1, Sb2, Se1, Se2, and Se3. 47

Figure 3.11. Defect analysis of Sb_2Se_3 thin-film solar cells and interface engineering with CdS:O window layer. (a) and (b) The calculated formation energy of point defects as a function of Fermi level for Sb-rich and Se-poor condition, respectively. (c) Transition levels of potential extrinsic point defects in the Sb_2Se_3 absorbers. (d) Band alignment diagram for interfacial engineering with sputtered oxygenated CdS:O at 0%, 1%, 2%, and 3% oxygen partial pressure. 48

Figure 3.12. (a) UV-Vis absorbance spectra for the oxygenated CdS and the inset shows the oxygenated CdS:O samples with increasing oxygen partial pressure of 0%, 1%, 2%, 3% O_2 during deposition. (b) Absorption coefficient extracted from the optical transmittance. (c) XRD pattern of the CSS deposited Sb_2Se_3 films. (d) Texture coefficient determined from the Sb_2Se_3 films grown on oxygenated CdS:O window layer. 52

Figure 3.13. (a) J-V curves and (b) EQE curves of FTO/CdS:O/Sb_2Se_3/graphite/Ag solar cells with sputtered oxygenated CdS:O window layers grown in the O_2/Ar+O_2 ratio at 0%, 1%, 2% and 3% at ambient temperature. 53

Figure 3.14. (a) and (b) Top view of the SEM images with EDS spectra in the inset of Sb_2Se_3 with the CBD deposited CdS and sputtered oxygenated CdS:O window layer, respectively. (c) Cross-sectional SEM images of the oxygenated CdS:O buffered Sb_2Se_3 with EDS mapping for the selected area. (d) Histogram distribution of grain size for CBD and Sputtered oxygenated CdS buffered Sb_2Se_3 film. (e) and (f) XPS data for the Sb *3d* and Se *3d* in the oxygenated CdS/Sb_2Se_3 film; and (g)-(h) SIMS spectra for the sputtered oxygenated and CBD CdS based Sb_2Se_3 devices, respectively.......................55

Figure 3.15. Electronic structure and optical absorption of Sb_2S_3. (a) Crystal structure of Sb_2S_3 with *Pnma* space group. (b) Electronic structure and orbital-resolved projected density of states calculated by DFT-mBJ functional. (c) The direct and indirect bandgaps extracted from the optical spectra. (d) Optical absorption coefficients of Sb_2S_3 calculated by DFT-mBJ functional..............59

Figure 3.16. Device performance of the Sb_2S_3 solar cells. (a) Illustrative energy level diagram of the layers in the cells. (b) and (c) The *J-V* curve and EQE spectra. 60

Figure 4.1. Crystal structures of different polymorphs of VO_2. (a) Low-temperature insulating M1 phase. (b) High-temperature metallic R phase. (c) Intermediate M2 and (d) M3 phases with alternating dimerized/undimerized V-V chains. .63

Figure 4.2. Schematic of the electronic band structures of R-VO_2 and M1-VO_2 based on Goodenough's model...66

Figure 4.3. Native defect diagrams under (a) O-rich and (b) O-poor conditions. The grey line indicates where Fermi level is pinned by the native defects. 75

Figure 4.4. Illustration of energy landscape of the MIT transition as a function of temperature of the system and diffusion of B atoms between interstitial sites. 78

Figure 4.5. Energetics of boron interstitial sites in VO_2 and delineation of spectroscopic signatures. (a)−(c) DFT calculated coordination environments for B-doped VO_2, illustrating the most thermodynamically favorable interstitial sites for B incorporation for R (A, R(1)), quenched M1 (B, M1(6)), and relaxed M1 (C, M1(1)). Vanadium atoms are depicted as blue spheres, oxygen atoms as red spheres, and B atoms as green spheres. (d) Overlay of quenched (inverted) and relaxed (blue/red/green) states to illustrate distortion (e) Normalized formation energies of B incorporation into different interstitial location

within the R (red), metastable M1 (violet), and relaxed M1 (blue) supercells. Panels (f) and (g) display the formation energies of charged defects for oxygen rich and oxygen poor conditions, respectively. The energies were calculated for substitutional boron defects at the oxygen sites (B_o), substitutional boron defects at the vanadium sites (B_v), and interstitial boron defects (B_i). For both oxygen-rich and oxygen-poor environments, the most stable defect at the calculated Fermi level (Figure 4.3) of ϵ_F = 0.48 and 0.62 is a 2+ interstitial boron defect B_i. 81

Figure 4.6. Density of states for (a) M1 and (b) R phases respectively, using a U value of 3.4 eV, which captures the insulating nature of the M1 polymorph and the metallic nature of the rutile polymorph. Charge density of the highest energy valence states for (c) B_V and (d) B_O defects with various charge states. In all cases, the charge is delocalized on V and O atoms instead of being localized around the B atom, which is expected from shallow defects. Purple circles indicate the electron density on oxygen atoms in the B_V defect cell. Analogous to the discussion of the B_V defect, the charges associated with B_O defect are delocalized also indicated in the also the 0 charge state orbital-resolved DOS plots for (e)-(f) B_V and (g)-(h) B_O defects. Hence, no significant lattice distortion is observed in proximity of the B atom. (f) and (h) are respective magnified views of (e) and (g) orbital-resolved projected DOS plots. The electronic states associated with the boron atom are mainly located within the deep valence band around -8 to -6 eV below the Fermi level, making it unlikely to induce significant electron density around the B atom near the Fermi level. This is consistent with Figure 4.3 where the top valence electrons are mostly delocalized across the V and O atoms instead of the B defects. 83

Figure 4.7. (a) and (b) Defect formation energy diagrams of Ge associated extrinsic defects under O-rich and O-poor poor growth conditions, respectively. (c) and (d) show the impact of Ge_V on the formation energy of oxygen vacancy (vac_O). 85

Figure 5.1. Crystal structures of few-layer 1T' WTe_2. (a) Top view of monolayer WTe_2 crystal structure with M_y mirror plane. (b) Side view of bilayer and trilayer WTe_2 crystal structure without inversion symmetry. The red arrow indicates the applied strain. The orange arrow indicates the polarization direction, which is out-of-plane. D is the interlayer spacing. 89

Figure 5.2. Ferroelectric transition in (a) bilayer and (b) trilayer WTe_2. The two FE states with opposite polarization direction can be transformed through interlayer sliding as indicated by the red arrow. The intermediate state with polarization vanishing appears when two dashed lines (red and blue) superimposed. 90

Figure 5.3. Change of out-of-plane polarization with externally applied strain. (a) and (c) Relaxed-ion case for bilayer and trilayer, respectively. (b) and (d) Clamped-ion case for bilayer and trilayer, respectively. 93

Figure 5.4. (a) Total energy of bilayer WTe_2 with respect to out-of-plane interlayer displacement. (b) Total energy of trilayer WTe_2 with respect to out-of-plane interlayer displacement. (b) and (c) Displacement of W and Te atoms along z direction for bilayer. (e) and (f) The displacement of W and Te atoms along z direction for trilayer. 95

Figure 5.5. Charge redistribution analysis for bilayer WTe_2. (a) Isosurface of charge density difference when the interlayer distance along the z direction is reduced by 0.1 Å (*i.e.* displacement d_z = -0.1 Å) and increased by 0.1 Å (*i.e.* displacement d_z = 0.1 Å), respectively. The label for each atom is indicated in (a). In (a), blue indicates the charge depletion, while yellow indicates the charge accumulation. The isosurface value is 0.00025 e/$Bohr^3$. (b) 2D (010) cross-section of charge density difference with the displacement d_z of -0.1 and 0.1 Å along the z direction, respectively. Here the (010) plane is cutting through W1 and W3 atoms. 96

Figure 5.6. (a) Bader charge difference between top layer and bottom layer as a function of displacement. (b) The change of Bader charge as a function of the displacement of each Te atom. (c) The change of Bader charge as a function of the displacement of each W atom. 96

Figure 5.7. Interlayer gliding d_x along the x direction induced by out-of-plane strain in the (a) bilayer and (b) trilayer case. The inset pictures illustrate the interlayer gliding. 99

LIST OF TABLES

Page

Table 3.1. Lattice constants of Sb_2Se_3 and Sb_2S_3 in Pbnm (#62) space group calculated by DFT with different exchange-correlation energy functionals. 19

Table 3.2. Calculated band gaps of Sb_2Se_3 and Sb_2S_3 using different exchange-correlation functionals. 20

Table 3.3. Dielectric constants along three principle directions. Ionic and electronic contributions are calculated using DFT-PBE and DFT-HSE06 functionals, respectively. 21

Table 3.4. Effective masses of holes and electrons in the unit of free electron mass (m_0) in bulk Sb_2Se_3 and Sb_2S_3. 23

Table 3.5. Born effective charge for symmetry-inequivalent atoms of Sb_2Se_3 and Sb_2S_3 calculated by DFT-PBE. 23

Table 3.6. Device performance parameters of champion device with varying ribbon orientations. 41

Table 3.7. Diffusion energy barrier for Cd and O across and along with the $(Sb_4Se_6)_n$ ribbons. 49

Table 3.8. Device performance parameters of FTO/CdS:O/Sb_2Se_3/graphite/Ag solar cells with sputtered oxygenated CdS:O window layers grown in the O_2/Ar+O_2 ratio at 0%, 1%, 2% and 3% at ambient temperature. 54

Table 3.9. Sb_2S_3 solar cell device performance parameters of champion device grown by CSS. 60

Table 4.1. PBE+U method calculated lattice constants, electronic bandgaps, and magnetic orders of monoclinic (M1) and rutile (R) VO_2 with and without spin polarization compared to experiments. 70

Table 4.2. Calculated V-V bond lengths compared to experimental data. 71

Table 4.3. Lattice constants, electronic bandgaps, and magnetic orders of monoclinic (M1) and rutile (R) VO_2 calculated by PBE0 with 7% Hartree-Fock exchange functional. 73

Table 5.1. Piezoelectric coefficient $e33$ in the unit of 10^{-12} C/m for bilayer and trilayer, respectively. It is obtained by a linear fitting of the polarization change with respect to $\epsilon33$.....94

Table 5.2. Bader charge of each atom in the optimized bilayer WTe_2.....98

1. INTRODUCTION

Energy and information technology have continuously improved the quality of life of human-beings and accelerated the development of economics and industry. As the conventional non-renewable energy resources such as fossil fuels are running out, renewable energy such as photovoltaics are expected to provide the next generation of safe, sustainable, environmentally friendly and affordable energy. At the same time, we are in the era of "big data" and the demand of data collection and analysis has increased exponentially. Nevertheless, in the current computing architecture, data are processed and stored separately, which is limited by the data transfer speed between the memory and processor, i.e. the so-called von Neumann bottleneck. Therefore, a more powerful computing paradigm is highly desired for storing, processing and transmitting complex information with minimal energy consumption. Inspired by human brain, neuromorphic computing has emerged as a promising alternative to conventional binary von Neumann computing architecture.

The development of both photovoltaics and neuromorphic computing relies on the discovery and design of novel functional materials. A wide range of materials have been explored for thin-film photovoltaics, such as silicon, CdTe, copper-indium-gallium-selenium (CIGS), copper zinc tin sulfide (CZTS), and perovskites.[1-3] However, each of these solar absorbers suffer from different challenges, such as stability in perovskites, high cost in Si-based solar cells, toxicity of Cd, and complex defects in CZTS. In recent years, emerging photovoltaic technologies, including quantum dots,[4] organic electronics,[5]

antimony chalcogenides,[3] and dye-sensitized solar cells[6] have drawn growing interest, due to their promise for achieving low cost and high efficiency. In contrast to the successful commercialization of photovoltaics, the research of neuromorphic computing is in its early stage. Initial neural circuits based on conventional complementary metal-oxide-semiconductor processors are energy inefficient for neuromorphic computing. Materials with dynamic behavior such as nonlinear conductance switch could directly emulate neural elements, and circuits built from those materials could outperform the nonlinear system made of thousands of transistors. Such materials candidates include phase-change materials, resistive-switching oxides, ferroelectric materials, two-dimensional (2D) materials, and organic materials.[7, 8]

In this dissertation, we investigated three emerging classes of functional materials, including (1) low-dimensional antimony chalcogenides as solar absorbers for photovoltaic applications, and (2) correlated transition metal oxides and (3) ferroelectric 2D transition metal dichalcogenides as phase-change materials for neuromorphic computing. The main focus was placed on the fundamental understanding of electronic structure and defect physics using various first-principles theoretical approaches.

1.1. Thin-Film Solar Cells

1.1.1. Introduction of Thin-Film Solar Cells

Photovoltaics, converting solar energy to electric power, provides one of the most efficient approaches to harvest renewable, affordable and environment friendly energy. A typical solar cell architecture has three components: an absorber layer where photo-excited electron-hole pairs are generated, electron and hole transport layers which allow the

transport of the separated charge carriers with opposite charges, and an extraction layer to collect carriers towards an external circuit (see Figure 1.1). A variety of solar absorbers have been used in different commercial thin-film solar cells. For example, silicon-, CdTe- and CIGS-based solar cells dominate the commercial photovoltaics production with the certified power conversion efficiency (PCE) over 22%, due to the low cost and desirable efficiency.[9, 10] In recent years, huge effort has been made to develop new photovoltaics. The emerging photovoltaic materials include copper zinc tin sulfide,[11] organic solar cells,[12] perovskites,[13] and quantum dot solar cells.[14] With the rapid progress in solar technology, photovoltaics play a more and more important role in the world renewable energy industry.

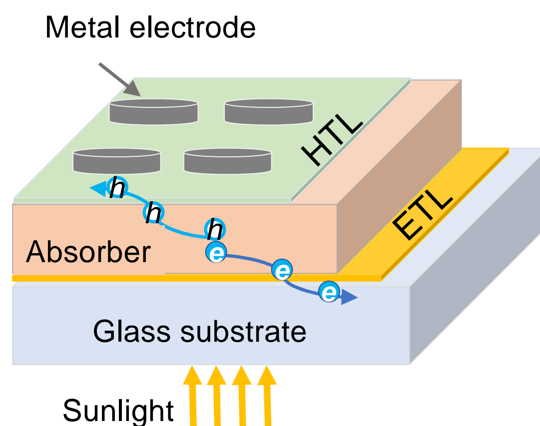

Figure 1.1. A typical thin-film solar cell device structure, with a metal electrode, a hole (HTL) and electron transport layer (ETL), and a glass substrate.

1.1.2. Antimony Chalcogenide Thin-Film Solar Cells

The very first antimony chalcogenide based solar cell device can be traced back to 1982, where the antimony selenide (Sb_2Se_3) thin film was deposited by chemical batch

deposition, and a 0.06% of PCE was yielded.[15] Then in 1993, an antimony sulfide (Sb_2S_3) solar cell was proposed using same deposition method with a structure of Au-Al/*p*-Si/Sb_2S_3/grid-Cu-graphite and a PCE of 5.1%.[16] In the recent decade, there is an obvious increase in antimony chalcogenide solar cell research, and remarkable achievements have been made. In 2015, Zhou *et al.* successfully obtained a PCE of 5.6% in Sb_2Se_3 solar cells by growing the $(Sb_4Se_6)_n$ ribbons vertically with respect to the CdS window layer.[17] They further promoted the efficiency above 6% by replacing the CdS to ZnO as window layers.[18] The idea of tuning the one-dimensional (1D) ribbon orientation during growth has been proved as a powerful approach to improve the device performance. In 2019, a PCE of 9.2% was achieved by Li *et al.*, with the high-quality Sb_2Se_3 nanorods vertically grown along [001]-direction.[19] This year, a highest device efficiency of 10% has been reported in antimony selenosulfide ($Sb_2(S, Se)_3$) thin film solar cells, demonstrating the potential of the alloyed-type solar absorbers based on antimony chalcogenides.[20] There is still plenty of room for improvement in these materials. Continuous investigation will bring us closer to the future practical uses of antimony chalcogenides in next-generation photovoltaic device applications.

1.2. Neuron-Inspired Computing

1.2.1. Introduction of Neuromorphic Computing

In the past decades, the electronic and computing revolution has driven the advancement in information technology industry and improved the efficiency in every other industry. As the so-called “information age” has arrived, we are facing more data intensive tasks than before.[21] Additionally, the reduction of device size improves the

fabrication cost and power consumption, impeding the physical limit. Modern computers are widely based on *von Neumann* architecture, where processing and storing data are accomplished in separate parts within the computers.[22] And the bus between the memory and processor limits the data transfer rate, referred to as *von Neumann bottleneck*. To improve the computing performance in the era of "*Big Data*", we need to reshape the computing paradigm for better information harvesting, storing, processing and transmission.

The human brain provides a powerful architecture for data-centric computing, where the information processing, storing and transmission are performed using the same neurons and synapses with minimal energy dissipation.[23, 24] Moreover, a variety of data-centric computing methods, such as machine learning (ML) using artificial neural networks (ANNs), are considered brain-inspired. In this sense, neuromorphic computing will not only outperform conventional *von Neumann* architectures, but also offers new opportunities for artificial intelligence.

To exploit the functionalities and capabilities of the human brain, we need to design the artificial neurons and synapses that mimic the biological ones and exhibit sharp spiking behavior. One approach is to build up nonlinearly dynamical devices using linear conductance switching, however thousands of transistors with linear conductance switching are required. An alternative approach is to develop novel materials with intrinsic nonlinearity, based on which new circuit elements can be built.

1.2.2. Phase-Change VO_2 as Potential Neuromorphic Materials

Materials for neuro-inspired computing have been gradually expanding, including phase-change materials (PCMs),[25-27] resistive-switching oxides,[28-30] spintronic materials,[31, 32] ferroelectric materials, 2D and heterostructure materials,[33, 34] and organic materials.[35] Among them, phase-change materials are a leading candidate. VO_2 and NbO_2 have been favorite materials owing to their pronounced metal-insulator transition (MIT) by strong electronic correlation accompanied by a structural phase change. Their capability of emulating neural circuits has been demonstrated through both experiments and simulations very recently.[36-39] Compared to NbO_2 with MIT temperature as high as 1081 K, the MIT in VO_2 occurs at a more accessible temperature of around 340 K. However, the MIT temperature in VO_2 is too low for practical device application, while the MIT temperature in NbO_2 is too high. Hence, there is a critical need to explore different modulation methods and understand the microscopic mechanism via, for examples, element doping, strain, interfacial charge and external field.

1.2.3. 2D Materials as Potential Neuromorphic Materials

The experimental realizations of neural circuits are largely explored in three-dimensional (3D) systems. Recently, two-dimensional (2D) materials attract more and more attention due to their intriguing electronic, photonic, optoelectronic, and mechanical properties. As electrical conductance in some of the 2D materials also exhibits nonlinear dynamics, they may provide another potential platform for developing neuromorphic computing. In principle, 2D materials based neural circuits not only scale down the device size, but also improve the tunability. In general, the current 2D-material memristive

systems are mainly based on two types of mechanisms: (1) inhomogeneities-induced conductance change,[34, 40, 41] and (2) electronically driven spiking behavior.[42] The former usually involves in the formation of metallic filament, inhomogeneous stress, and ion diffusion, and the latter often relies on conductance change by varying external control parameters, such as temperature, voltage, external field, *etc*. Here we focus on the electronically driven memristors as they may provide better control with low energy dissipation. 2D transition metal dichalcogenides (TMDCs) and their alloys have shown both semiconducting and metallic phases, demonstrated by experiments and first-principles calculations.[43-46] It was found that the MIT can be triggered via charge doping or electrostatic gating.[47, 48] 2D ferromagnetic and ferroelectric materials have also attracted tremendous interests in the field of nonvolatile memories and memristors.[49] Despite the issues of small polarization value and scalable production, they gain advantages over traditional 3D materials, such as the tunability and flexibility. Several device models have been proposed recently, such as HfO_2 or ZrO_2 based thin-film ferroelectric field effect transistor (FeFET) and tunnel juctions.[50] In summary, their neuroemulative behaviors underpin the nonlinear dynamical property that could be utilized for nonlinear switching and memory functions.

2. FIRST-PRINCIPLES METHODS FOR POINT DEFECT CALCULATIONS

Defects, especially point defects, play a significant role in both solar absorbers and neuromorphic materials. Point defects can involve various types of species with different charge states and spin states. Probing and characterizing point defects require extensive and careful experimental measurements. In parallel, first-principles density functional theory (DFT)[51, 52] becomes a powerful tool to predict the point defect properties in semiconductors and guide the experimental design of semiconductor devices. In this chapter, the key concept and first-principles methods will be introduced for point defect calculations and analyses.

2.1. Defect Formation Energy

The formation energy of charged defect is defined as,

$$\Delta E^f(D,q) = E(D,q) - E(bulk) - \Sigma n_i \mu_i + q\epsilon_F + E_{corr},$$

where $E(bulk)$ and $E(D,q)$ are the total energy of the pristine host cell and the supercell with defect *D* in the charge state q, respectively.[53] μ_i refers to the chemical potential of atomic species i, and n_i is the number of atoms added ($n_i > 0$) or removed ($n_i < 0$). $q\epsilon_F$ represents the chemical potential of electron reservoir, where ϵ_F is the Fermi level. ϵ_F is conventionally referenced to the valence band maximum (VBM) in the perfect cell and varies between the VBM and conduction band minimum (CBM). The chemical potential corresponds to the energy of exchanging atoms between the defect and the element reservoir. μ_i can be split into two parts as $\mu_i = \mu_i^o + \Delta\mu_i$. μ_i^o represents the chemical potential of the reference, associated with the elemental phases of each species, and $\Delta\mu_i$

is the allowed chemical potential variation. $\Delta\mu_i$ is constrained by the rule that our targeted compound must be more stable than any other competing phase. For example, in the calculations of antimony chalcogenide Sb_2X_3 (X = Se, S), we only consider two extreme cases, *i.e.* the X rich (Sb poor) and X poor (Sb rich) condition. We therefore have the following set of constraints on $\Delta\mu_{Sb}$ and $\Delta\mu_{Se/S}$:

$$\Delta\mu_{Sb} < 0,$$

$$\Delta\mu_{Se/S} < 0,$$

$$2\Delta\mu_{Sb} + 3\Delta\mu_{Se/S} = \Delta\mu_{Sb_2X_3},$$

where $\Delta\mu_{Sb_2Se_3}$ is the formation energy of Sb_2X_3. Here, the formation of Sb and Se/S is prohibited.

E_{corr} is a correction to the formation energy to account for the spurious image charge interaction due to the finite supercell formalism for simulating the dilute defect limit. Specifically, E_{corr} addresses two issues: (1) the interaction between the defect and its images under periodic boundary condition, and (2) the electrostatic potential alignment between the defect supercell and the pristine bulk.[54]

2.2. Supercell Approach for Dilute Limit

In first-principles study using plane-wave DFT approach, the calculations are conducted in a supercell with the periodic boundary condition. The supercell size depends on the characteristics of the system and defects as well as the computational cost. However, in reality, the defect is often in the dilute limit. In order to model dilute defects using the supercell approach, a posteriori correction for electrostatic potential is necessary for each single supercell calculation.

Several correction schemes have been proposed in the past decade. Initially, a periodic array of point charges was considered, which was associated with a Madelung energy.[55] This correction scheme has a simple formula of

$$E_{\mathrm{M}} = \frac{q^2\alpha}{2\varepsilon L},$$

where α is the appropriate Madelung constant, q is the point charge, ε is the dielectric constant, and L is the lattice parameter of periodic array. Based on this point charge correction, Makov and Payne derived the next leading order term to the interaction potential. This results in a term that scales as $(aL^{-1} + bL^{-3})$.[56] Freysoldt *et al.* developed a correction method which treats the long-range and short-range interactions between charged defects separately[57] where an isotropic dielectric constant was used. Kumagai and Oba extended this method to anisotropic systems by using full dielectric tensor.[58] Given the high anisotropic feature in Sb_2X_3, we adopt the correction method proposed by Kumagai *et al.* in our study.

2.3. Transition Levels of Charged Defect

The formation energy of charged defects can be further used to compute defect transition level, $\epsilon(q/q')$, It is defined as the Fermi level for which the formation energy of a charge state q is equal to the formation energy of a charge state q', indicating the relative stability of defect in charge state q. It is given by,

$$\epsilon(q/q') = \frac{E_f^{D,q}(E_F=0) - E_f^{D,q'}(E_F=0)}{q'-q}.$$

Shallow transition levels located near the band edges are associated with *n*- or *p*-type doping, while deep transition levels usually act as carrier recombination centers, referred

to as trap states. These are the transition levels in thermodynamic equilibrium where atoms and electrons in defect systems are fully relaxed to their equilibrium state, different from the transition levels upon optical absorption where no structural relaxation involves in the charge transition process.[59]

2.4. Equilibrium Fermi Level, Defect Concentration, and Carrier Density

Based on the defect formation energy, the equilibrium Fermi level at a given temperature, charged defect concentration and carrier density can be obtained by solving a set of self-consistent equations under the charge neutrality condition.[60] Assuming the entropy and pressure contributions to the Gibbs free energy are negligible, then the defect concentration in charge state q is given by

$$c_{D,q}(E_F,T) = N_{site}\mathrm{e}^{-\frac{E_f^{D,q}(E_F)}{k_B T}},$$

where N_{site} is the number of sites per volume available for defect *D* with charge state q, and k_B is the Boltzmann constant. The concentration in this case is determined by the Fermi level E_F and the synthesis temperature *T*. The charge neutrality condition yields:

$$-n_e(E_F,T) + n_h(E_F,T) + \sum_D \sum_q q_D \cdot c_{D,q}(E_F,T) = 0.$$

Here, n_e and n_h are free electron and hole concentrations at temperature *T*. n_e and n_h can be calculated by integrating the product of electron/hole density of states (DOS) and electron/hole Fermi-Dirac distribution function:

$$n_e(E_F,T) = \int_{CBM}^{+\infty} g_e(E) f(E - E_F, T) dE,$$

and

$$n_h(E_F,T) = \int_{-\infty}^{VBM} g_h(E)\big(1 - f(E - E_F,T)\big)dE.$$

$f(E - E_F, T)$ is the Fermi-Dirac distribution. $g_e(E)$ and $g_h(E)$ are the DOS of electrons and holes, respectively, which are approximated as

$$g_{e,h} = \frac{1}{4\pi^2}\left(\frac{2m_{e,h}^*}{\hbar^2}\right)^{\frac{3}{2}}\sqrt{E}.$$

$m_{e,h}^*$ are the electron and hole effective masses and can be obtained from the parabolicfitting of the curvature of band energy at the CBM and VBM, that is

$$m_{e,h}^* = \left(\frac{1}{\hbar^2}\frac{\partial^2 E_{e,h}(\boldsymbol{k})}{\partial^2 \boldsymbol{k}}\right)^{-1}.$$

For a given chemical potential and synthesis temperature, the Fermi level at equilibrium, defect concentrations, and carrier densities are determined as the self-consistent solution to the above equations. Moreover, as the synthesis temperature is often different from operating temperature, we also calculate the corresponding values at room temperature (*i.e.* 300K in the present work) by assuming that the defect concentrations remain the same during quenching and only the charge state of defects will re-equilibrate under the dilute limit. In this case, the densities of different charge states of the same defect type redistribute by following Boltzmann statistics.

3. ANTIMONY CHALCOGENIDES THIN-FILM PHOTOVOLTAICS*

3.1. Electronic Structures and Defect Chemistry in Antimony Chalcogenides

3.1.1. Introduction

Photovoltaics (PV) convert solar energy to electricity and provide renewable and environment friendly energy. A variety of solar cells have been developed in the past using different absorbers, including silicon, cadmium telluride (CdTe), copper zinc tin sulfide (CZTS), copper-indium-gallium-selenium (CIGS), organic/polymer, and perovskite solar cells.[1-3] Among them, silicon, CdTe and CIGS based solar cells are dominating the current commercial PV market.[9, 10] However, the current PV technologies still face some issues. For example, crystalline silicon (c-Si) solar cells suffer from high cost. The toxicity of Cd and the scarcity of Te are two notable issues of CdTe solar cell. The complexity of defect control hinders the further improvement of power conversion efficiency (PCE) in CZTS solar cell.[61] Perovskites have attracted tremendous attention in the last decade, and their PCE is approaching 25%, making them promising for commercialization.[62, 63] Nevertheless, several challenges such as stability and toxicity of Pb-based perovskites need to be addressed.[64] Alternative stable, cost-effective and scalable PV absorbers are hence highly desired.

*Part of this chapter was reprinted with permission from "Tunable Quasi-One-dimensional Ribbon Enhanced Light Absorption in Sb_2Se_3 Thin-film Solar Cells Grown by Close Space Sublimation" by L. Guo, B. Zhang, Y. Qin, D. Li, L. Li, X. Qian, and F. Yan. Solar RRL 2, 1800128 (2018), Copyright © 2018, John Wiley and Sons; "Sputtered Oxygenated CdS Window Layers for Sb_2Se_3 Thin Film Solar Cells with 7% Efficiency " by L. Guo, B. Zhang, A. Montgonery, S. Saurav, L. Li, X. Qian, and F, Yan.. Solar RRL 3, 1900225 (2019), Copyright © 2019, John Wiley and Sons; and "Scalable and Efficient Sb_2S_3 Thin Film Solar Cells Fabricated by Close Space Sublimation" by L. Guo, B. Zhang, S. Li, Q. Zhang, M. Buettner, L. Li, X. Qian, and F. Yan, APL Materials 7, 041105 (2019), Copyright © 2019, AIP Publishing LLC.

Recently, antimony chalcogenides (Sb_2X_3, where X=Se, S) have attracted great attention.[17] Sb_2X_3 possess quasi-one-dimensional (1D) ribbon-like structures, *i.e.* $(Sb_4X_6)n$, which are bonded by weak van der Waals (vdW) interaction. Their suitable bandgaps (~1.2 eV for Sb_2Se_3, ~1.7 eV for Sb_2S_3), high optical absorption coefficient (~10^5 cm^{-1}), low cost, good stability, and earth abundant Sb and Se/S endow antimony chalcogenides with great potential in solar energy applications. Owing to the unique 1D vdW structures, antimony chalcogenides have benign grain boundaries with highly anisotropic transport property, very different from conventional bulk solar cell materials such as CdTe where the untreated grain boundaries often serve as carrier recombination centers and significantly limit the device performance. Different growth techniques have been employed, such as rapid thermal deposition (RTD),[65] close space sublimation (CSS),[66-69] vapor transport deposition (VTD),[70] and atomic layer deposition (ALD),[71] to improve the quality of the absorber layer and achieve scalable production with controllable synthesis parameters. Besides, various device structures have been fabricated to suppress the interfacial diffusion and boost carrier separation.[18, 72] Significant progress has been made on improving the device performance. For example, a high PCE of 9.2% was recently achieved by tuning Sb_2X_3 ribbons vertically aligned with the substrate.[19] Very recently, Tang *et al.* achieved a record high PCE of 10% with antimony selenosulfide $Sb_2(S,Se)_3$ using an optimized hydrothermal deposition technique,[20] showing great promise of antimony chalcogenide based solar cells.

Defect tolerance is a crucial characteristic of excellent photovoltaic absorber. Native defects determine the carrier mobility, lifetime, recombination rate, and doping

limit. Recently, Savory *et al*. calculated the formation energies of native defects and found that Se-on-Sb (Se_{Sb}) antisites with mid-gap transition levels were most likely to form, suggesting they may be the major obstacle to further improve the open-circuit voltage (V_{oc}).[73] Huang and co-workers demonstrated Sb_2Se_3 is intrinsically p-type under Se-rich condition[74] due to Se_{Sb} and even 2Se-on-Sb ($2Se_{Sb}$) antisites, and n-type under Sb-rich condition due to the low formation energies of donor defects such as V_{Se} and Sb_{Se} antisites. In both reports, the calculations were conducted using first-principles DFT[51, 52] with HSE06 hybrid exchange-correlation energy functional[75] and D3 Grimme dispersion correction,[76] while different approaches were employed to correct the finite size effect on the charged defect formation energy calculations within the dilute defect limit. Besides the study of intrinsic defects, Stoliaroff *et al*. suggests several possible dopants in Sb_2Se_3 to either enhance the native *p*-typeness or induce *n*-type doping.[77] Cai *et al*. pointed out that the compensation of the intrinsic donor and acceptor defects limit the electrical conductivity in Sb_2S_3 and proposed a two-step doping strategy to improve the efficiency.[78] These studies revealed that the native defects play critical roles in both Sb_2Se_3 and Sb_2S_3. Recently, Hobson *et al*. carried out a deep level transient spectroscopy study of deep level defects in Sb_2Se_3 and revealed the presence of traps in the 358-690 meV range below the conduction band edge, while the grain boundary is relatively benign.[79]

Using first-principles theoretical calculations, here we demonstrate that quasi-1D Sb_2Se_3 and Sb_2S_3 possess unique electronic structures and defect chemistry which eventually determines their superior optical and dielectric properties. Their important

implications on the photovoltaic performance as light absorbers will be discussed. We further calculate the formation energies of a variety of intrinsic defects and defect transition levels in Sb_2X_3 and subsequently the equilibrium Fermi level, free carrier densities, and defect concentrations. Our results provide a theoretical interpretation of the observed *p*-type conductivity in Sb_2Se_3 and nearly intrinsic semiconductor behavior in Sb_2S_3. These theoretical findings not only offer microscopic understandings of the electronic structure and native defects in Sb_2X_3 photovoltaic absorber, but also may provide valuable guidance to further advance antimony chalcogenides based solar cells.

3.1.2. Computational Details

First-principles DFT calculations were performed using the Vienna Ab Initio Simulation Package (VASP) .[80] We employed the Perdew-Burke-Ernzerhof (PBE)[81] form of exchange-correlation energy functional within the generalized gradient approximation (GGA)[82] and a Γ-centered Monkhorst-Pack[83] k-point sampling for Brillouin zone integration. A plane wave basis set with a 400eV energy cutoff and a 4×4×12 k-point grid were used for structure optimization and electronic relaxation. As DFT-GGA often underestimates the band gap, we applied the modified Becke-Johnson (mBJ)[84, 85] exchange potential for electronic structure and optical property calculations. Frequency dependent dielectric function was calculated in the independent particle approximation with a dense k-point sampling of 10×10×30. The convergence criteria for electronic relaxation was set to 10^{-6} eV, and the maximal residual force for structure optimization was less than 0.01 eV $Å^{-1}$.

As the accuracy of formation energies is important for defect calculations, we employed the HSE06 hybrid exchange-correlation functional to further relax bulk and defect structures and calculate the total energies. This approach was previously shown to provide accurate prediction for the atomic and electronic structures in defective systems.[86, 87] Savory *et al*. and Huang *et al*. reported that the DFT calculations with HSE06 functional yield good agreement with experiments.[73, 74] Different vdW corrections were tested and compared, including optB86-vdW non-local correlation functional[88-90] and D3 dispersion correction,[76] and the lattice constants of Sb_2Se_3 are best reproduced by HSE06-D3. Therefore, we used HSE06-D3 for all defect calculations with a supercell of 1×1×3 containing 60 atoms for both Sb_2Se_3 and Sb_2S_3 to mimic the dilute defect limit. In addition, spin polarization was considered in our calculations.

3.1.3. Crystal and Electronic Structure of Quasi-1D Antimony Chalcogenides

Antimony chalcogenides, Sb_2Se_3 and Sb_2S_3, possess a very unique structure, as shown in Figure 3.1a. Their ground state structures are formed by quasi-1D ribbons which are weakly bonded by vdW interaction, while within the ribbon Sb-Se (or S) are bonded by strong valence bonds, forming infinite one-dimensional ribbons (*i.e.* $(Sb_4X_6)_n$). Their unit cell contains 20 atoms, where there are three symmetry-inequivalent types of Se/S atoms and two symmetry-inequivalent types of Sb, as indicated in Figure 3.1a. Furthermore, Table 3.1 summarizes the lattice parameters calculated by DFT with different exchange-correlation energy functionals as well as the experimental values. Hybrid functional HSE06-D3 outperforms other functionals in the relaxed geometry, and the obtained lattice constants are in very good agreement with the experiment data. Thus,

all the following DFT calculations including electronic and optical properties and defect calculations were carried out with the HSE06-D3 relaxed structures.

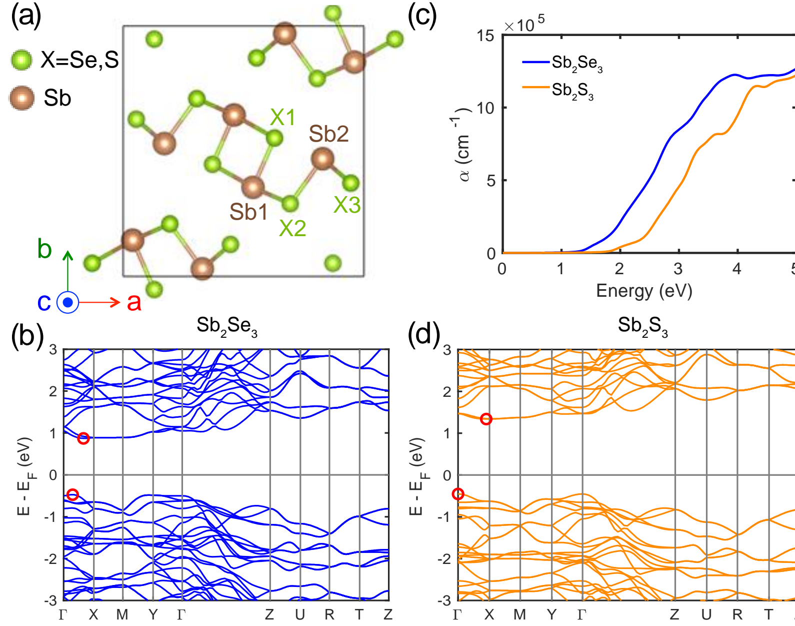

Figure 3.1. (a) Crystal structure of antimony chalcogenides Sb_2Se_3 and Sb_2S_3. (b) and (d) Calculated electronic band structures of Sb_2Se_3 and Sb_2S_3. Red circles indicate VBM and CBM. (c) Calculated optical absorption spectra.

The electronic band structures of Sb_2Se_3 and Sb_2S_3 along the high symmetry points in the Brillouin zone are shown in Figure 3.1b and d. As DFT-PBE often underestimates band gap and DFT-HSE06 calculations are usually expensive, we compute the band structures along the full k-paths by using the modified Becke-Johnson (mBJ) exchange functional, which is known to provide accurate electronic structures comparable to hybrid functional and many-body perturbation theory with GW approximation.[84, 85] The electronic bands of Sb_2Se_3 and Sb_2S_3 along ΓZ are more dispersed than those along ΓY and ΓX, indicating the higher group velocity and more facile electron transport along the

ribbons (c axis) than across ribbons (a/b axes). Moreover, the mBJ and HSE06 calculated bandgaps of Sb_2Se_3 and Sb_2S_3 are summarized in Table 3.2. Both Sb_2Se_3 and Sb_2S_3 have indirect gaps located along ΓX. The calculated band gaps in Sb_2Se_3 and Sb_2S_3 are 1.35 and 1.79 eV, respectively, making them good photovoltaic absorber candidates. The results are in reasonable agreement with GW quasiparticle bandgap (1.3 eV for Sb_2Se_3, and 1.5 for Sb_2S_3).[91] Furthermore, small electron/hole effective mass (*e.g.* $< 0.5\ m_0$, where m_0 is the free electron mass) is often beneficial for carrier transport.[92, 93] Here we calculated electron and hole effective masses using a parabolic fitting at the CBM and VBM, and the results are presented in Table 3.4. The calculated hole effective masses of Sb_2Se_3 and Sb_2S_3 are $0.3m_0$ and $0.5m_0$ which are indeed reasonably small and desired for *p*-type semiconductors.

Table 3.1. Lattice constants of Sb_2Se_3 and Sb_2S_3 in Pbnm (#62) space group calculated by DFT with different exchange-correlation energy functionals.

		Sb_2Se_3			Sb_2S_3		
lattice parameters		a	b	c	a	b	c
DFT	PBE+vdW-optB86	11.45	11.89	4.01	11.06	11.32	3.86
	PBE+ vdW-D3	11.48	12.02	4.02	11.11	11.43	3.86
	HSE06+ vdW-optB86	11.95	12.26	4.01	11.66	11.51	3.85
	HSE06+ vdW-D3	11.50	11.96	3.95	11.17	11.42	3.80
Exp.[94, 95]		11.62	11.77	3.96	11.23	11.31	3.84

Table 3.2. Calculated band gaps of Sb_2Se_3 and Sb_2S_3 using different exchange-correlation functionals.

		Direct gap (eV)	Indirect gap (eV)
Sb_2Se_3	Exp.[67]	1.20	1.15
	DFT-HSE06	1.43	1.39
	DFT-mBJ	1.38	1.35
Sb_2S_3	Exp.[66]	1.56	1.71
	DFT-HSE06	1.93	1.79
	DFT-mBJ	1.90	1.79

3.1.4. Anisotropic Dielectric Properties of Quasi-1D Antimony Chalcogenides

Besides the suitable electronic band gap and small hole effective mass, the dielectric constant of Sb_2X_3 is quite large. A large dielectric constant usually leads to strong screening to charges and defects, thereby suppressing carrier scattering and recombination. Typically the macroscopic dielectric constant of 10 or higher, including the electronic and ionic contributions, will enhance electron-hole pair dissociation, or exciton dissociation into free charge carriers in photovoltaics.[92, 96] The electronic contribution comes from the polarization by redistribution of electronic density, while the ionic part is associated with the polarization by ionic motion. The calculated dielectric tensors for Sb_2Se_3 and Sb_2S_3 are summarized in Table 3.3, where the ionic part is computed by DFT-PBE, and electronic part is computed using the HSE06 functional since

it is sensitive to the band gap. The dielectric tensors of both compounds show significant anisotropy where the dielectric constants along ribbons are much higher than the other two directions. The large dielectric constants of Sb_2X_3 indicate that the charge carriers are subject to enhanced screening when transporting along the ribbons, thereby reducing carrier scattering.

Table 3.3. Dielectric constants along three principle directions. Ionic and electronic contributions are calculated using DFT-PBE and DFT-HSE06 functionals, respectively.

	Direction	ε_{ion}	ε_{elec}
Sb_2Se_3	xx	76.97	15.43
	yy	97.56	15.46
	zz	3.94	10.69
Sb_2S_3	xx	66.08	11.06
	yy	90.39	11.63
	zz	4.025	8.28

To understand the large dielectric constants in Sb_2X_3, we further investigate the corresponding Born effective charge (BEC). The BEC tensors of symmetry-inequivalent Sb and Se/S atoms are calculated using DFT-PBE. The results are listed in Table 3.5. The valence of Sb and Se/S elements are +3 and -2. However, in Sb_2Se_3, the ions present a maximum effective charge of +7.22 e on Sb1, +7.49 e on Sb2, -4.19 e on Se1, -4.01 e on Se2, and -4.93 e on Se3, much higher than their nominal ionic charges. A similar trend was also observed in Sb_2S_3, with the BEC of 6.86 e on Sb1, 6.38 e on Sb2, -3.86 e on S1, -3.75 e on S2, and -4.59 e on S3. The large BEC implies strong lattice polarization with atom displacements. In ionic crystals, the charges of atoms will be close to their nominal

charges in the compound formed by ionic bonds. On the other hand, in covalent crystals, the presence of covalent bonds leads to significant charge transfer when atoms are displaced from their original positions. Therefore, the large BEC reveals the mixed ionic-covalent Sb-Se/S bonds in Sb_2Se_3 and Sb_2S_3, and eventually results in large dielectric constants.

3.1.5. Low Exciton Binding Energy for Efficient Electron-Hole Separation

Based on the effective mass and dielectric constant, we can estimate the exciton binding energy E_b using the hydrogenic model:

$$E_b = \frac{\mu}{m_0 \epsilon^2} R_H,$$

where R_H is the Rydberg constant of hydrogen atom (13.6 eV), and ϵ is the average dielectric constant. μ is the effective reduced mass of the exciton, obtained by

$$\frac{1}{\mu} = \frac{1}{m_h^*} + \frac{1}{m_e^*}.$$

The calculated effective reduced exciton mass is $0.22m_0$ and $0.38m_0$ for Sb_2Se_3 and Sb_2S_3, respectively. Consequently, the exciton binding energy is low, only 15 meV and 48 meV, comparable with the thermal energy (*i.e.* k_BT, 25 meV at room temperature). The low exciton binding energy suggests efficient dissociation of photoexcited electron and hole pairs into free carriers.

Finally, we also calculated another important physical property for photovoltaic absorber, *i.e.* optical absorption spectra of Sb_2X_3 using DFT-mBJ. The frequency-dependent averaged optical absorption coefficient is shown in Figure 3.1c, and the calculated values agree with the experimental measurement of 10^4~10^5 cm^{-1} for Sb_2S_3

and >10^5 cm^{-1} for Sb_2Se_3 in the visible region,[67] demonstrating antimony chalcogenides are indeed good solar absorbers.

Table 3.4. Effective masses of holes and electrons in the unit of free electron mass (m_0) in bulk Sb_2Se_3 and Sb_2S_3.

Effective mass	Sb_2Se_3	Sb_2S_3
m_h	0.3	0.5
m_e	0.8	1.5
μ	0.22	0.38

Table 3.5. Born effective charge for symmetry-inequivalent atoms of Sb_2Se_3 and Sb_2S_3 calculated by DFT-PBE.

	Ion	Zxx	Zxy	Zxz	Zyx	Zyy	Zyz	Zzx	Zzy	Zzz
Sb_2Se_3	*Sb1*	4.38	0.00	0.00	0.44	2.63	0.00	0.00	0.00	7.22
	Sb2	7.49	-1.86	0.00	-0.19	2.15	0.00	0.00	0.00	5.80
	Se1	-4.19	-1.19	0.00	-1.04	-1.76	0.00	0.00	0.00	-4.08
	Se2	-3.33	1.51	0.00	0.03	-1.58	0.00	0.00	0.00	-4.01
	Se3	-4.35	-0.06	0.00	-0.18	-1.44	0.00	0.00	000	-4.93
Sb_2S_3	*Sb1*	3.95	0.35	0.00	0.27	2.83	0.00	0.00	0.00	6.86
	Sb2	6.38	-1.47	0.00	0.01	1.96	0.00	0.00	0.00	5.36
	S1	-3.44	-0.83	0.00	-0.84	-2.00	0.00	0.00	0.00	-3.86
	S2	-3.24	1.28	0.00	-0.05	-1.39	0.00	0.00	0.00	-3.75
	S3	-3.65	0.35	0.00	0.37	-1.39	0.00	0.00	0.00	-4.59

The above theoretical investigations of electronic, optical, and dielectric properties show that Sb_2Se_3 and Sb_2S_3 have several nice characteristics, including suitable bandgap, small effective hole mass, small exciton binding energy, large dielectric constants, hence

strong screening, and high optical absorption coefficient. These superior electronic structures endow Sb_2Se_3 and Sb_2S_3 with great potential as light absorbers for thin-film PV applications.

3.1.6. Defect Formation Energy and Transition Levels

Experiments have shown that Sb_2X_3 solar cells suffer from low V_{oc}, which is often caused by high recombination rate due to the presence of the mid-gap trap states. In order to understand the types of defects that may generate mid-gap levels, we conducted a study of intrinsic point defects of Sb_2X_3. Here we consider five types of intrinsic defects, namely vacancy (V_{Sb}, $V_{Se/S}$), interstitial (S_i, Se_i, and Sb_i), and Sb and Se/S antisites (Sb_S and Se_{Sb}/S_{Sb}) for all symmetry-inequivalent atomic sites with different charge states.

Based on the approach described in Chapter 2, we first investigated the intrinsic defects of Sb_2Se_3. Due to the anisotropic structure, defects behave differently at symmetry-inequivalent sites. The formation energy as a function of the Fermi level (E_F) is plotted in Figure 3.2a and b for Se rich and Se poor conditions, respectively. The antisite (Se_{Sb1}, Se_{Sb2}, Sb_{Se1}, Sb_{Se2}, and Sb_{Se3}) and interstitial (Se_i and Sb_i) defects are likely to act as donors/acceptors depending on the Fermi level. When the Fermi level is near VBM, those defects donate electrons and exhibit positive charge states. When the Fermi level is close to CBM, they accept electrons and are negatively charged. The formation of defects can be regulated by controlling the chemical potentials of the associated elements. In Se rich condition, acceptor-like defects V_{Se2} and V_{Se3} have negative formation energy when the Fermi level is located at VBM ($i.e.\ E_F = 0$). In addition, when $E_F = 0$, Sb interstitials also have low formation energy, and Se_{Sb1}, and Se_{Sb2} have formation energy close to zero.

Therefore, when the Fermi level is close to VBM, the Se vacancies, Sb interstitials, and Se_{Sb} antisite defects are the dominant defects in Se rich condition. As shown in Figure 3.2c, those defects create mid-gap trap states. As E_F increases, V_{Sb} becomes more likely to form due to the decrease of its formation energy. Among all the defects, when the Fermi level is close to VBM, the donor defect V_{Se2} with charge state q=+2 has the lowest formation energy, contributing free electrons to the conduction bands and making it n-type. On the other hand, when the Fermi level is close to CBM, the acceptor defect Se_{Sb2} with charge state q=-1 and V_{Sb} with charge state q=-3 have the lowest formation energies, donating free holes to the valence bands and making the system p-type. V_{Se2} (q=+2) and Se_{Sb2} (q=-1) have the same formation energy at $E_F = 0.4$ eV under Se-rich condition. Thus, the Fermi level will be pinned at around 0.4 eV. Under Se-poor condition, Sb_{Se}, V_{Se} and Sb_i have even lower formation energy while V_{Sb}, Se_{Sb} and Se_i have higher formation energy at $E_F = 0$ eV, compared wth Se rich condition. The easier formation of the hole killers will restrain the free carriers in the p-type Sb_2Se_3. Therefore, Se rich condition is recommended during growth. The Fermi level in this case is pinned at around 0.7 eV by donor defect V_{Se2} and acceptor defect Sb_{Se1}.

Sb_2S_3 exhibits the similar behavior as Sb_2Se_3, as shown in Figure 3.3a-c. The antisite (S_{Sb1}, S_{Sb2}, Sb_{S1}, Sb_{S2}, and Sb_{S3}) defects possess positive charge states when the Fermi energy moves towards VBM, while they exhibit accept-like defects with negative charges as Fermi energy is close to CBM. V_{S2}, V_{S3}, Sb_i, S_{Sb2} and S_{Sb1} are dominant defects with negative formation energy at $E_F = 0$ under S-rich condition. S-on-Sb antisites possess low formation energy, suggesting antisite defects in Sb_2S_3 are easy to form in the

quasi-1D structure. The Sb-on-S antisites can be more easily to form under S poor conditions. Comparing the formation energies under two extreme conditions, the donor defect concentration is higher under S poor condition, due to the significant decrease of the formation energy of Sb-on-S antisites, Sb interstitials and S vacancies. Those defects will be detrimental to the free carrier concentration and trap the carriers. The Fermi levels are pinned at 0.75 eV by S_{Sb2} (q=+1) and V_{Sb2} (q=-3) in S rich condition, and at 0.85 eV by V_{S2} (q=+2) and V_{Sb2} (q=-3) in S poor condition.

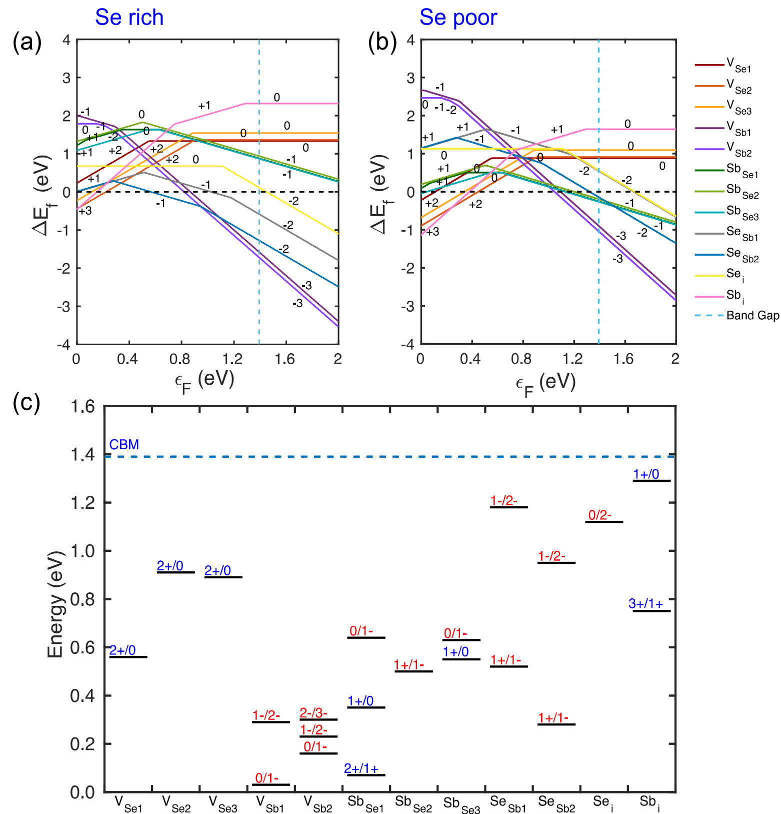

Figure 3.2. Defect formation energy diagrams of Sb_2Se_3 under (a) Se rich and (b) Se poor conditions. (c) Defect transition levels in Sb_2Se_3. The formation energies of native point defects in Sb_2Se_3 is plotted as a function of the Fermi level with VBM as reference. The bandgap adopted here is calculated by HSE06. The slope of each line indicates the most favorable charge state at the corresponding Fermi level. Positive and negative charge state indicate the donor and acceptor, respectively. The red and blue colors in (c) indicate the donor and acceptor transition levels, respectively.

To further increase the carrier density of Sb_2X_3, extrinsic doping is a feasible approach. We then investigate the dopability of Sb_2Se_3 and Sb_2S_3. Dopability refers to the domain of the Fermi energy accessible through doping.[97] When acceptor-like defects are doped into the system, the Fermi energy is shifted towards the valence band, and the acceptor formation energy decreases with ϵ_F. With increasing hole doping, the Fermi energy will decrease and shift towards VBM. Subsequently the formation energy of hole killers will also decrease, and at certain point they will form spontaneously. Across this point, further doping is inhibited because the formation of the hole killers (e.g. V_{Se2}^{+2}) will negate the acceptors. As mentioned above, the doping limit of Sb_2Se_3 occurs at 0.4 eV and 0.7 eV for Se-rich and Se-poor growth conditions, respectively, and the doping limit of Sb_2S_3 occurs at 0.75 eV and 0.85 eV for S-rich and S-poor growth conditions, respectively. The Se/S-rich condition destabilizes the donor defects (hole killers), hence facilitate *p*-type doping. Hence, Sb_2Se_3 has better *p*-type doping capability than Sb_2S_3, and the doping limit can be further overcome by passivating the killer defects.

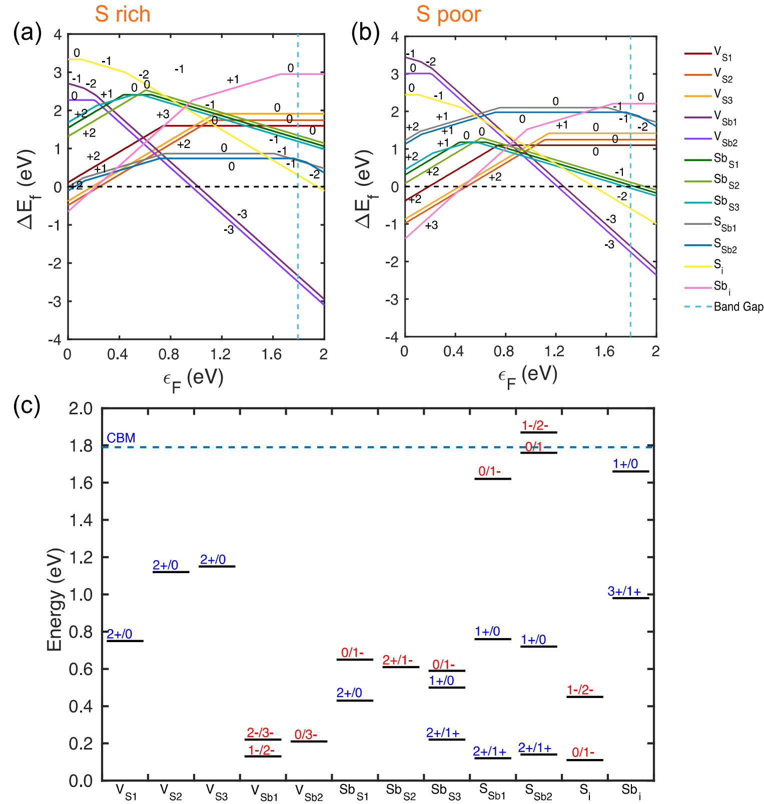

Figure 3.3. Defect formation energy diagrams of Sb_2S_3 under (a) S rich and (b) S poor conditions. (c) Defect transition levels in Sb_2S_3. The formation energies of native point defects in Sb_2S_3 are plotted as a function of the Fermi level with VBM as reference. The bandgap adopted here is calculated by HSE06. The red and blue colors in (c) indicate the donor and acceptor transition levels, respectively.

We notice that some of the defects exhibit negative U behavior.[98, 99] For example, V_{Se} and V_S with +1 charge state are unstable at any value of the Fermi level. Its formation energy is always higher than that of 0 and +2 charge states. This character is related to strong electron-lattice interaction, which leads to significant atomic relaxation. Figure 3.4 illustrates the local lattice relaxations of V_{Se2} with +1 and +2 charge states, *i.e.* V_{Se2}^{+1} and V_{Se2}^{+2}, and the color of the atoms represents charge transfer with respect to V_{Se2}^{0}

and V_{Se2}^{+1}, respectively, obtained from Bader charge analysis.[100, 101] The formation of +2 charge state, V_{Se2}^{+2}, is accompanied by a large outward relaxation away from Se vacancy. In fact, the nearest-neighbor Sb atoms relax away from the vacancy by -19%, -5% and 21% of the equilibrium V_{Se2}-Sb bond length (*i.e.* the bond between Se vacancy and its nearest Sb atom) for the +0, +1, and +2 charge states with respect to the Se-Sb bond length in the pristine bulk. The released energy due to large local lattice relaxation overcompensates the electron Coulombic interaction energy. Since antimony chalcogenides have soft quasi-1D ribbon-like structures with weak interchain interaction, they are able to accommodate larger lattice relaxation than conventional 3D bulk crystals, thereby exhibiting negative U behavior in these defect structures.

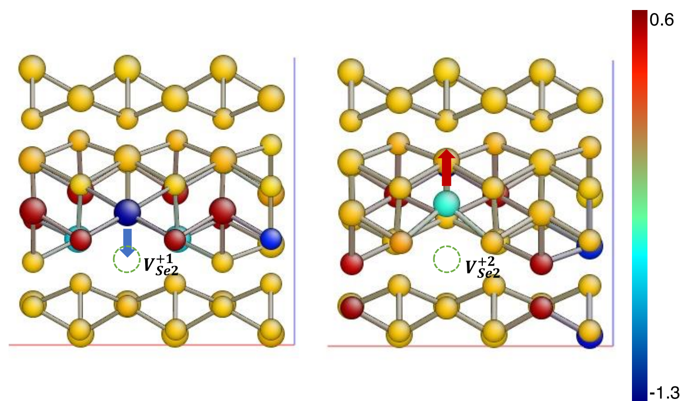

Figure 3.4. Atomic structures of V_{Se2} with +1 and +2 charge states, respectively. The color of the atoms indicates the electron depletion (blue) or accumulation (red) with respect to V_{Se2} with +0 and +1 charge states.

3.1.7. Defect Concentration, Carrier Density, and Their Implication on *p*-/*n*-Typeness

Using the method described in Chapter 2, we first calculate the carrier density and defect concentrations in Sb_2Se_3 based on the defect formation energy. Figure 3.5a and d show the Fermi level under synthesis temperature ($E_{F,\mathrm{syn}}$) and equilibrium temperature ($E_{F,\mathrm{eq}}$) as a function of synthesis temperature from 300 to 1000 K. The melting temperature of Sb_2Se_3 is 885 K, below 1000K, as indicated by the dashed line in Figure 3.5. The corresponding Fermi level is calculated by assuming that the system is quenched from synthesis temperature to room temperature, and during annealing the defect concentrations remain the same but the charge state of each defect type can change and re-equilibrate. The calculated $E_{F,\mathrm{eq}}$ decreases as the temperature increases. Under Se rich condition, the equilibrium Fermi level is around 0.3-0.34 eV within the synthesis temperature range, which is close to VBM, showing a *p*-type nature. The dominant carrier is hole, as shown in Figure 3.5c, with the concentration on the order of 10^{13} cm^{-3}, in agreement with the experiment, which is majorly contributed by the dominant defect Se_{Sb1}^{-1} (Figure 3.5b). In Se-poor condition, the equilibrium Fermi level is located near the half of the bandgap, suggesting the weak *p*-typeness and low hole density. It is attributed to the formation of donor defects V_{Se2}^{+2} and V_{Se3}^{+2}, although there is still high concentration of acceptor defects Sb_{Se1}^{-1} and Sb_{Se3}^{-1}, as shown in Figure 3.5e. Figure 3.5f shows the calculated the hole and electron density. The hole density is only on the order of 10^{7} cm^{-3} and increases with the temperature. The electron density is on the order of 10^{6} cm^{-3} and

decreases with the temperature. Our calculations therefore confirm that Sb_2Se_3 is an intrinsic *p*-type semiconductor, and the Se-rich growth condition is desired.

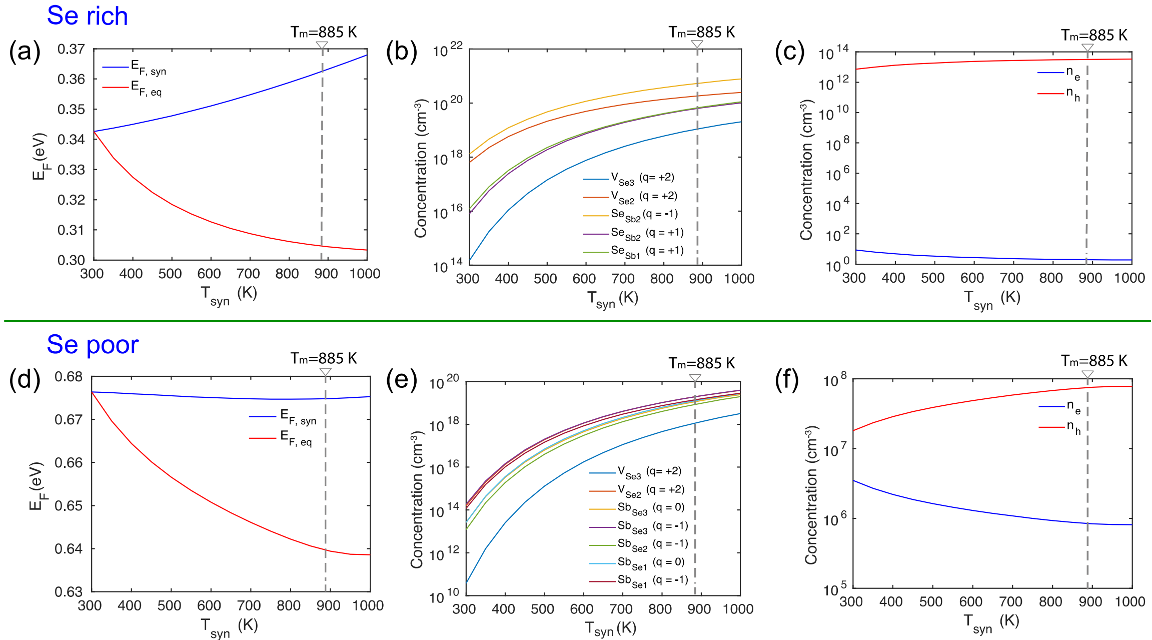

Figure 3.5. (a) and (c) Fermi level of Sb_2Se_3 at synthesis and equilibrium temperatures as a function of synthesis temperature under Se rich and Se poor conditions, respectively. (b) and (e) Electron and hole densities at equilibrium temperature as a function of synthesis temperature under Se rich and Se poor conditions, respectively. (c) and (f) The concentration of dominant defects as a function of synthesis temperature under Se rich and Se poor conditions, respectively. The dashed line indicates the melting temperature of Sb_2Se_3 at 885 K.

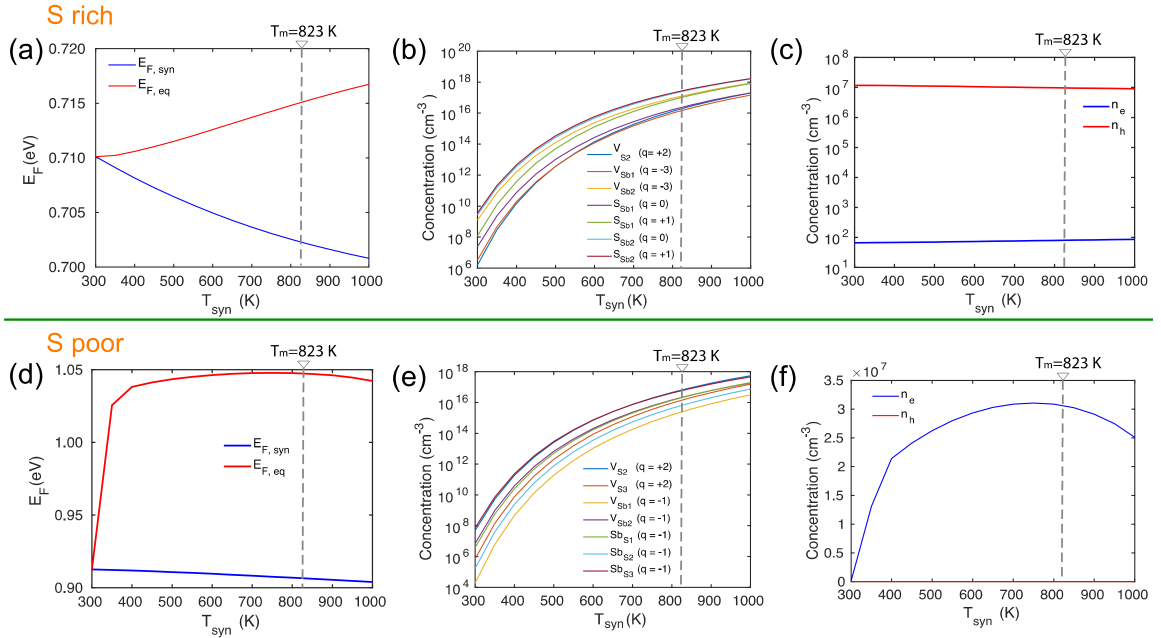

Figure 3.6. (a) and (c) Fermi level of Sb_2S_3 at synthesis and equilibrium temperatures as a function of synthesis temperature under S rich and S poor conditions, respectively. (b) and (e) Electron and hole densities at equilibrium temperature as a function of synthesis temperature under S rich and S poor conditions, respectively. (c) and (f) Concentration of dominant defects as a function of synthesis temperature under S rich and S poor conditions, respectively. The dashed line indicates the melting temperature of Sb_2S_3 at 823 K.

The same approach was applied to study Sb_2S_3. The results are presented in Figure 3.6. The melting point of Sb_2S_3 is also indicated by dashed line at 823K. In S rich condition, the equilibrium Fermi energy is around 0.7 eV, at which donor defects S_{Sb1}^{+1} and S_{Sb2}^{+1} have high concentrations. However, the acceptor defect V_{Sb2}^{-3} also has high concentration but possesses higher charge state, thereby donating holes to valence bands and leading to the *p*-type in Sb_2S_3 with hole density on the order of 10^7 cm^{-3}. The competition between the donors and acceptors in leads to minimal change in the hole density as the temperature increases. On the other hand, Sb_2S_3 is a weak intrinsic *n*-type under S poor condition,

caused by the donor V_{S2}^{+2} and V_{S3}^{+2}. However, V_{Sb2}^{-1}, Sb_{S3}^{-1} and Sb_{S1}^{-1} compete with the donors and their concentration increases as the temperature is elevated. Therefore, the electron density decreases at high temperature (Figure 3.6f). The Fermi energy is pinned above the mid-gap, as seen in Figure 3.6d, reflecting the *n*-type nature. In general, the carrier density in Sb_2S_3 is significantly lower than that in Sb_2Se_3, which is consistent with experiment findings. Sb_2Se_3 is intrinsically *p*-type, while Sb_2S_3 is almost intrinsic semiconductor. Further strategies, such as introducing certain dopants, may be conducted to suppress the donor-like defects in order to increase the carrier density.

3.1.8. Conclusions

In summary, we systematically investigate the electronic structure and native defects in antimony chalcogenides using first-principles DFT. On one hand, the unique quasi-1D ribbons in Sb_2Se_3 and Sb_2S_3 lead to anisotropic transport with higher group velocity along the ribbon. More importantly, they possess suitable bandgap and high optical absorption that are desirable for photovoltaics. The large Born effective charge and large dielectric constant suggest strong charge screening, thereby reducing carrier scattering and recombination. Besides, the dispersed band structure near VBM and CBM leads to small hole and electron effective masses. The small effective mass and large dielectric constant result in small exciton binding energy, suggesting efficient exciton dissociation and formation of free charge carriers in antimony chalcogenides. Since antimony chalcogenides have soft quasi-1D ribbon-like structures with weak interchain interaction, they are able to accommodate larger lattice relaxation than conventional 3D bulk crystals, thereby exhibiting negative U behavior in these defect structures.

On the other hand, Sb_2Se_3 and Sb_2S_3 exhibit complex defect chemistry competing with the above superior electronic structure of pristine Sb_2Se_3 and Sb_2S_3. The dominating defects include antisite defects, anion vacancies, and interstitial defects. Anion vacancies have low formation energy even under anion-rich condition. The weak vdW interlayer interaction leads to the low formation energy of interstitial defects between Sb_2X_3 ribbons. These defects can create mid-gap transition levels, which may explain the low V_{oc} observed in experiments. In order to improve the V_{oc}, it is necessary to suppress the defects, for example, by optimizing growth condition, post-annealing, or introducing extrinsic dopant. Regarding the doping limit of Sb_2Se_3 and Sb_2S_3, the *p*-type doping for Sb_2Se_3 under Se-rich condition is quite accessible since the pinned Fermi energy is close to VBM, but it will be difficult under Se-poor condition due to the low formation energy of Se vacancies. In contrast, Sb_2S_3 has limited *p*- and *n*-type dopability under both S-rich and S-poor condition. From the defect concentration and carrier density calculations, we found that Sb_2Se_3 under Se rich condition is *p*-type and the dominant defect is Se_{Sb2} with charge state of -1. Compared to Sb_2Se_3, carrier density in Sb_2S_3 is relatively low, exhibiting intrinsic semiconductor behavior.

Our present work provides microscopic understanding of electronic, dielectric, and optical properties of antimony chalcogenides, revealing their great potential for photovoltaic applications as well as the challenges to be addressed. The present study suggests that effort shall be made in future to mitigate the defects and further boost the performance of antimony chalcogenide based solar cells.

3.2. Impact of Quasi-1D Nature on Photovoltaic Performance

3.2.1. Introduction

The anisotropic nature of these ribbon-like chalcogenides, though potentially beneficial to solar cell performance, requires careful growth to suspend the needle or flake growth. To overcome this challenge, various growth technologies were introduced for antimony chalcogenides, such as rapid thermal evaporation (RTE),[17, 18] and solution-based technology.[102, 103] However, these approaches are not fully compatible with high-throughput manufacturing technology. For example, commercial CdTe technology from *First Solar* is based on a VTD process, which is on a par with the CSS process for CdTe manufacturing and allows for high-throughput deposition onto moving substrates.[104] Meanwhile, CSS technique directly vaporizes the solid raw materials, which has been widely used in the lab to achieve the scalability of chalcogenide photovoltaics and could greatly reduce the cost.

In this section, we theoretically investigated the anisotropic electronic and optical properties of Sb_2Se_3, and experimentally demonstrated that the quasi-one-dimensional ribbons can be tailored by varying CSS growth conditions. It is demonstrated that [211]-oriented Sb_2Se_3 exhibits the best device performance with 4.27% PCE, which is in agreement with the theoretical understanding. Through first-principles calculations, we not only show the orientation-dependent optical properties of Sb_2Se_3, but also identify a more beneficial ribbon orientation ([211]-orientation) than the previoius reported one ([221]-orientation).[17] The [211]-oriented ribbons have also been experimentally synthesized by CSS in our work, together with other oriented ribbons. In addition, the success of CSS technology in the non-cubic anisotropic materials opens up avenues for

integrating these ribbon/layer-like materials into the most successful large-scale chalcogenide solar cell manufacturing process.

3.2.2. Computational Details

Atomistic, electronic structures, and orientation-dependent optical properties were calculated using first-principles DFT as implemented in the VASP.[80] Since van der Waals interaction is present between neighboring $(Sb_4Se_6)_n$ ribbons, we adopted optB86-vdW non-local correlation functional that approximately accounts for dispersion interactions. The structural optimization and electronic relaxation were calculated using a Γ-centered Monkhorst-Pack k-point sampling grid of 12×4×4.[83] The maximal residual force of each atom is less than 0.02 eV $Å^{-1}$, and the convergence criteria for electronic relaxation was set to 10^{-6} eV. For optical property calculations, a k-point grid of 28×12×12 is used in the mBJ calculations.

3.2.3. Orientation-Dependent Transport Behavior and Optical Absorption

To analyze the ribbon structures along different orientation, we first conduct bulk structure optimization using first-principles DFT. The calculated lattice constants for bulk Sb_2Se_3 are in good agreement with the experiments. Then we extracted different ribbon configuration from the bulk. As shown in Figure 3.7a-b, the one-dimensional $(Sb_4Se_6)_n$ ribbons stack along c axis by strong Sb-Se bonds, while the ribbons are weakly bonded by vdW forces along a and b directions, without dangling bonds, in agreement with the results of Zhou *et al.*[17] Figure 3.7c-e illustrate the carrier transport along $(Sb_4Se_6)_n$ chains in different orientations. When the $(Sb_4Se_6)_n$ ribbons are grown parallel to the substrate (*i.e.* grown along [120] direction with (120) plane parallel to the substrate, as illustrated in

Figure 3.7c), the vdW gap between the ribbons will exert potential barriers for carrier transport towards top and bottom substrates where carriers are collected. However, when the ribbons are [211]- and [221]-oriented on top of the substrate (Figure 3.7d and e), the charge carrier can easily transport along the ribbons, which will reduce photogenerated carrier recombination. Obviously, the series resistivity is much higher in [120]-oriented grain than in [211]- and [221]-oriented grains.[17] Therefore, to promote the carrier transport and improve the device performance, these $(Sb_4Se_6)_n$ ribbons should be grown normal to the substrate, *e.g.* [211]- and/or [221]-direction, as shown in Figure 3.7f and g. Additionally, the [211]-oriented grain in principle should be better than that of [221]-oriented grain in terms of charge transport, because the angle between the ribbon and the surface is 52.6° in the [211]- oriented grain, higher than 46.1° in the [211]-oriented grain (Figure 3.7f and g).

To further understand the impact of quasi-one-dimensional $(Sb_4Se_6)_n$ ribbons on the optical properties, we calculated the orientation-dependent optical absorption. We firstly calculated the frequency dependent dielectric function $\epsilon(\omega)$, including both the real and imaginary parts, within the independent particle approximation implemented in VASP. The calculated dielectric function is closely related to the extinction coefficient K and refractive index n as

$$\epsilon(\omega) = (n + iK)^2.$$

Then the optical absorption coefficient α can be obtained from extinction coefficient K,

$$\alpha = \frac{4\pi K\omega}{c},$$

where *c* is the speed of light. The calculated absorption coefficient along different ribbon orientation is shown in Figure 3.8a. It clearly demonstrates that the [211]-oriented films have higher absorption than that of the [221]-oriented films, providing theoretical evidence for higher light absorption when the $(Sb_4Se_6)_n$ ribbons are vertically grown against the substrate. Our theoretical findings were further verified by the UV-Vis spectra of CSS-deposited Sb_2Se_3 from optical characterization. The calculated absorption coefficient as a function of the grain orientation from the absorbance measurement is shown in the Figure 3.8b, which match well with the theoretical predictions (Figure 3.8a).

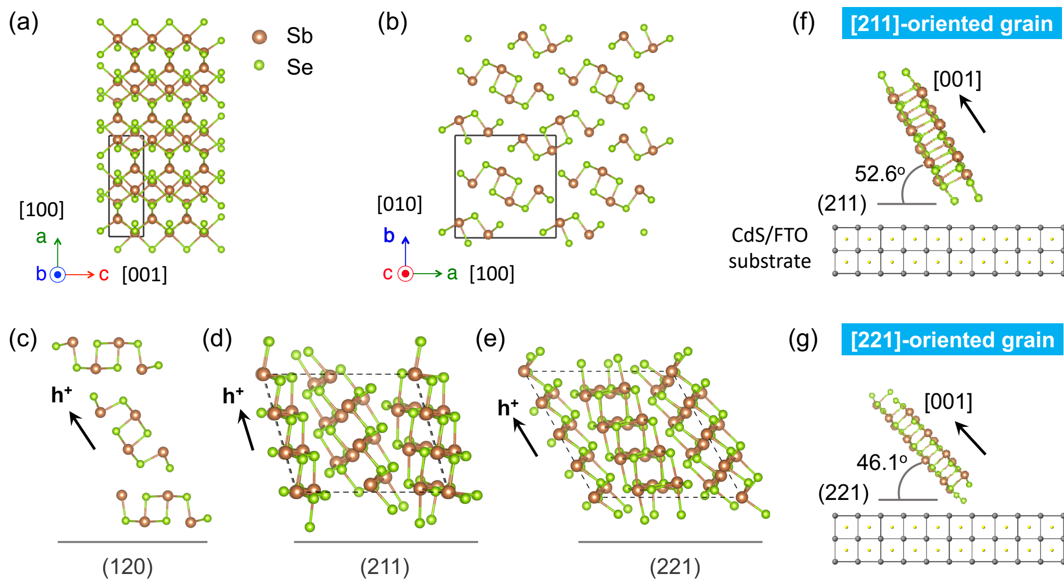

Figure 3.7. Sb_2Se_3 van der Waals crystals with tunable ribbons $(Sb_4Se_6)_n$ showing anisotropic transport behavior. (a) and (b) Atomic configuration from the side and top view, respectively. (c)-(e) Atomic structures of [120]-, [211]-, and [221]-oriented Sb_2Se_3 ribbons on the CdS-coated FTO glass substrate. (f) and (g) Comparison between [211]- and [221]-oriented grains on CdS substrate. The ribbons in the [211]-oriented grains are aligned closer to the plane normal compared to the ribbons in the [221]-oriented ones, suggesting a more facile carrier transport along [211]-oriented grains.

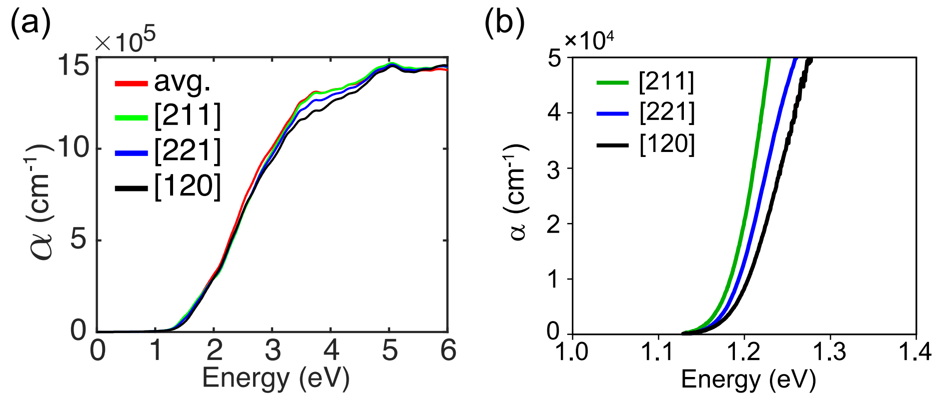

Figure 3.8. Orientation-dependent optical absorption coefficient from (a) theoretical calculations, and (b) UV-vis absorbance spectra for the films with [120]-, [221]-, and [211]-oriented grains.

3.2.4. Orientation-Dependent Device Performance

Next, the dependence of the Sb_2Se_3 solar cell device performance on the orientation of $(Sb_4Se_6)_n$ ribbons has been investigated. The Sb_2Se_3/CdS heterojunction solar cells were fabricated with graphite and Ag electrode (Figure 3.9a). The energy level alignment in the device is shown in Figure 3.9b, which is efficient for charge transfer (graphite work function of 5.0 eV *vs*. Au of 5.1 eV). The device performance with different ribbon orientation is shown in Figure 3.9c, and the device characteristics are listed in Table 3.6. Here, we selected the Sb_2Se_3 films grown at different substrate temperature with various $(Sb_4Se_6)_n$ ribbon orientation for device fabrication. The main focus here is the orientation dependent device performance, and other contributions to the device performance, such as the improved crystallinity and reduced defects at various substrate temperature, may not be discussed here. The strong correlation between the device performance and the ribbon orientation was established through the *J-V* measurement. As

expected, the film with [211] preferred orientation shows the best device performance with 4.27% PCE, which is originated from the improved open-circuit voltage V_{oc} and short-circuit current J_{sc}. The reduced series resistance (R_{oc}, resistance at V_{oc}) dominates the device performance, while the shunt resistance (R_{sh}) keeps almost constant. This device behavior can be explained by the [211]-oriented grain consisting of tilted $(Sb_4Se_6)_n$ ribbons, where the carrier transport in the [211]-oriented grains is more facile than in the [221]- and [120]-oriented grains (as shown in Figure 3.7c-e and inset of Figure 3.9c with different vdW boundaries). This observation is in agreement with the previous RTE devices,[17] where better device performance may be achieved using Au electrode with better ohmic contact between the metal and semiconductor than graphite paste. The higher intensity of (120) peaks indicate more $(Sb_4Se_6)_n$ ribbons parallel with the substrate, which significantly increases the serial resistance of the device and thus lowers the device performance (e.g., reduce V_{oc} and J_{sc}). Here, further evidence of the benefit from the ribbon orientation dependent light trap is provided by the external quantum efficiency (EQE) measurement (see Figure 3.9d). The ribbon orientation dependent light absorption is in agreement with the UV-Vis absorption spectra as shown in Figure 3.8c and f. The [211]-oriented grains could absorb more light in the range of 400 to 850 nm. In particular, the [211]- and [221]-oriented film significantly improve the light absorption than that of [120]-oriented film. The photocurrent with integrated EQE is consistent with the J_{sc} determined by the *J-V* curve.

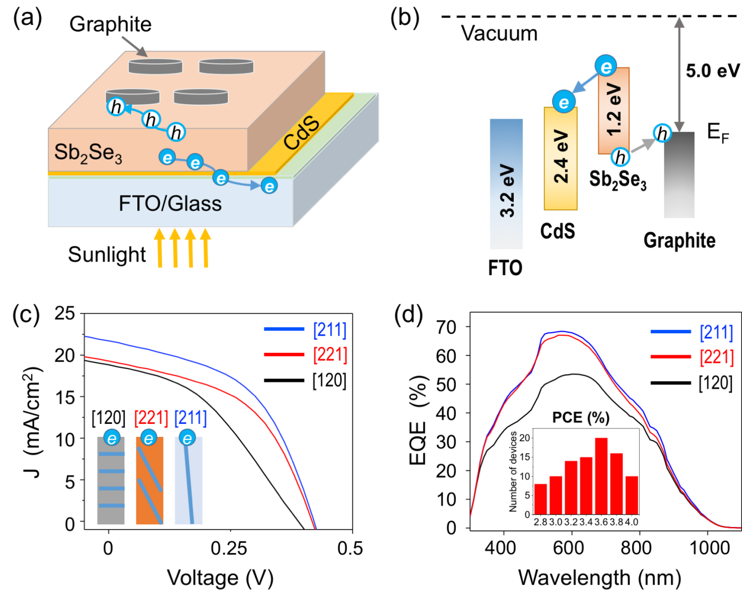

Figure 3.9. Device performance of the Sb_2Se_3 cells. (a) Schematic solar cell geometry. (b) Energy level diagram of the layers in the cells. (c) and (d) the current density-voltage (J-V curve) and EQE spectra of the orientation dependent films. The inset of (c) illustrates the films with different ribbon orientation. The inset of (d) shows the histogram of device efficiencies from various fabricated devices.

Table 3.6. Device performance parameters of champion device with varying ribbon orientations.

Grain orientation	V_{oc}, V	J_{sc}, mA cm^{-1}	FF, %	R_{oc}, Ω cm^2	R_{sh}, Ω cm^2	PCE, %
[211]	0.421	21.74	46.65	59.25	1087	4.27
[221]	0.415	19.26	49.43	66.75	1006	3.92
[120]	0.386	18.82	39.75	144.57	1025	2.91

3.2.5. Conclusions

In summary, we demonstrate that the tunable $(Sb_4Se_6)_n$ ribbon orientation can enhance the light absorption and enable the Sb_2Se_3 thin film solar cells with 4.27% PCE.

The Sb_2Se_3 thin film can be successfully grown by the low-cost close-space sublimation. We found that the light absorption in the Sb_2Se_3 film was correlated with the ribbon direction and the device performance is significantly influenced by the orientation of the $(Sb_4Se_6)_n$ ribbons. Our results demonstrate that environment-friendly Sb_2Se_3 thin film solar cells can be manufactured in large scale at a low cost with low energy consumption thanks to the earth-abundant elements and the low deposition temperature, and it can be directly integrated into the recent vapor transport deposition technology for thin film photovoltaics.

3.3. Interface Engineering via Sputtered Oxygenated CdS:O Window Layer

3.3.1. Introduction

We have shown that the $(Sb_4Se_6)_n$ ribbon orientation is significantly impacted by the film deposition parameters, such as substrate temperature, source temperature and the post-sensitization of the deposited film.[17, 105-107] Remarkably, a wide range of the window layer materials (*e.g.*, ZnO, and CdS) have been utilized to tune the ribbon orientation and suspend the device degradation.[18, 107, 108] However, the champion device performance is still far from its theoretical PCE limit (~31%).[109] The photovoltaic device performance is severely limited by the low open circuit voltage (V_{OC}) of ~0.4 V in contrast to its bandgap of 1.1 eV due to abundant deep defects,[70] although the short circuit current density (J_{SC}) was improved to ~ 30 mA cm^{-2}.[110] Given the well-known CIGS PV technology with PCE of above 22%, although CIGS has similar bandgap (~1.1 eV) but its V_{OC} record is as high as ~0.744 V, We believe that there is plenty of room to improve V_{oc} and PCE in Sb_2Se_3 solar cells. In fact, the theoretical limit of V_{oc} and PCE

for a solar absorber with a bandgap of 1.2 eV can reach 0.935 V and 32.74%, based on Shockley-Queisser limit. The current Sb_2Se_3 performance is far below from its limit. Therefore, it is worth developing effective approaches to lift the V_{OC} in Sb_2Se_3 solar cells.[9]

Traditionally, oxygen in the chalcogenide thin film solar cells could contribute to the improved device performance. For example, oxygen in CdTe solar cells can increase the acceptor concentration and lifetime, and oxygen in the CdS/CdTe interface could prevent the interdiffusion.[111-113] Sputtered oxygenated CdS (CdS:O) window layer is able to improve the V_{OC} in CdTe and other chalcogenide solar cells (such as Cu_2BaSnS_4) due to its high resistivity and transparency.[114-117] The sputtered oxygenated CdS:O window layer is composed by CdS and $CdSO_x$ with a wide bandgap range (2.4 to 3.7 eV), which can be achieved by engineering oxygen composition during the sputtering deposition.[116] Moreover, the high resistivity of CdS:O window layers can passivate the absorber/CdS interface and suspend the interface recombination.[116] Thus, both V_{OC} and J_{SC} can be improved by introducing CdS:O to CdTe devices.[114] Currently, the most widely used window layer for Sb_2Se_3 cells is chemical bath deposited (CBD) CdS window layer.[68, 114, 118-121] It was reported that introducing oxygen during the Sb_2Se_3 deposition could passivate interface defects and lead to enhanced device performance with ~4.8% PCE.[118] However, the role of oxygen in the CdS:O/Sb_2Se_3 interface has not been elucidated well.

We have conducted our first-principles theoretical calculations and experimental studies to understand the role of interfacial oxygen in the CdS:O/Sb_2Se_3 heterostructure.

Our first-principles calculations indicate the interdiffusion mechanism and defect chemistry associated with the oxygenated CdS:O window layer based Sb_2Se_3 solar cells. Oxygen has a higher diffusion barrier across $(Sb_4Se_6)_n$ ribbons (*i.e.* perpendicular to the ribbon direction) than that along the ribbons inside the vdW gap. Controlling oxygen content in the interfacial area of CdS:O/Sb_2Se_3 can effectively passivate the vdW gap of Sb_2Se_3, thereby blocking the Cd diffusion into Sb_2Se_3 to form *n*-type Cd_i interstitials. Our theoretical study suggests that higher V_{OC} can be achieved in the Sb_2Se_3 thin film solar cells with interface engineering. Following the theoretical prediction, we then propose to replace the CBD CdS layer by sputtered oxygenated CdS:O window layer in order to passivate the interface between window layer and Sb_2Se_3. By systematic tuning of oxygen concentration in the sputtered oxygenated CdS:O layer, we achieved the highest V_{OC} (~0.432 V), J_{SC} (~29.9 mA cm^{-2}) and PCE (~7.01%) in the CSS-grown Sb_2Se_3 devices with the superstrate F:SnO_2/CdS:O/Sb_2Se_3/graphite/Ag device architecture. The reactively sputtered CdS:O window layer effectively enhances the bandgap of CdS:O and tailors the $(Sb_4Se_6)_n$ ribbons to [211]-textured orientation. The grain size of Sb_2Se_3 grown on the sputtered CdS:O is larger than that on CBD CdS, suggesting that the oxygen in the CdS:O can also impact the Sb_2Se_3 growth. The interfacial element distribution analysis indicates that the interfacial oxygen can suppress the CdS/Sb_2Se_3 interdiffusion, which prevents the Cd interstitial formation in Sb_2Se_3 absorber layer. In addition, the device physics analysis demonstrated that the increased V_{OC} stem from the improved built-in voltage, and the improved J_{SC} comes from the thicker depletion region and the reduced interfacial recombination in the CdS:O/Sb_2Se_3 device. This study of extrinsic point defects

based on first-principles DFT further proves that oxygen associated defects, substitutional defects (O_{Sb}) and (O_{Se}) and interstitial defect (O_i), hardly become *n*-type. However, Cd interstitial (Cd_i) is donor defect, therefore, to reduce its concentration the Se-rich condition is desired. These theoretical and experimental findings demonstrate that the interface engineering is an effective approach to improve device performance of Sb_2Se_3 thin film solar cells, which can be used to break the photovoltage limit in Sb_2Se_3 solar cells.

3.3.2. Computational Details

Cd and O diffusion energy barriers in Sb_2Se_3 were calculated using the climbed image nudged elastic band (NEB) method.[122] The total energy calculations were based on first-principles DFT[51, 52] as implemented in VASP.[80] The PPBE[81] form of exchange-correlation functional within the GGA[82] and a plane wave basis set with a 400 eV energy cutoff were employed in the DFT calculations. The structural optimization of bulk Sb_2Se_3 was performed with a Γ-centered Monkhorst-Pack k-point sampling grid of 4×4×12, maximal residual force of less than 0.01 eV $Å^{-1}$,[83] and an energy convergence criteria of 10^{-6} eV for electronic relaxation. The optB86-vdW nonlocal correlation functional was adopted to account for the weak vdW interactions between ribbons.[88-90] The calculated lattice parameters *a*, *b*, and *c* of the unit cell are 11.482 Å, 11.870 Å and 4.014 Å, respectively. A supercell of 1×1×3 was constructed to determine the diffusion energy barrier in the dilute limit.

For defect formation energy and transition levels, we employed the finite-size correction scheme proposed by Freysoldt *et al.*[57] and Oba *et al.*[58]. The unit cell structure was enlarged to 2×2×6 supercell, containing 480 atoms, to minimize the errors

caused by image charge interaction. The charged defect formation energy is defined by $\Delta E^f = E(D,q) - E(bulk) - \sum n_i \mu_i + q\epsilon_F + E_{corr}$. Here $E(D,q)$ is the total energy of the defect supercell with charge q and $E(bulk)$ is the total energy of pristine cell without any defect. μ_i represents the chemical potential of species i involved in the defect, and n_i corresponds to the number of atoms added (n_i< 0) or removed ($n_i < 0$). ϵ_F is the Fermi level using the valence band maximum as the reference. E_{corr} refers to the correction term. It mainly consists of two parts: the electrostatic potential alignment between the defect cell and the bulk, and the interaction between the charge and its images due to the periodic boundary condition used in the DFT calculations. More details is given in Chapter 2.

3.3.3. Interdiffusion and Defect Chemistry Associated with CdS:O

To elucidate the role of oxygen in the interface between CdS and Sb_2Se_3, we first investigate the diffusion behavior using first-principles DFT calculations. Two diffusion pathways were considered in the calculations for both Cd and O atoms (Figure 3.10). One diffusion pathway is along the $(Sb_4Se_6)_n$ ribbons as shown in Figure 3.10a, and b for Cd and O, respectively. The other diffusion pathway is across the $(Sb_4Se_6)_n$ ribbons, as shown in Figure 3.10d,e. The calculated diffusion energy barriers are shown in Figure 3.10c,f for the diffusion across and along ribbons, respectively. As shown in Table 3.7, the diffusion barrier of Cd along ribbons is ~0.6 eV, while Cd diffusion across ribbons is about 0.8 eV. The diffusion barrier of O across ribbons is ~1.7 eV, much higher than ~1 eV for O diffusion along ribbons. In both cases, Cd has lower diffusion barrier than that of O, suggesting that Cd diffusion is relatively faster than O. It may be related to their degraded

stabilities due to diffusion.[118] The high diffusion energy barriers of oxygen suggests that oxygenating the CdS/Sb_2Se_3 interface may fill the vdW gaps and block Cd diffusion.

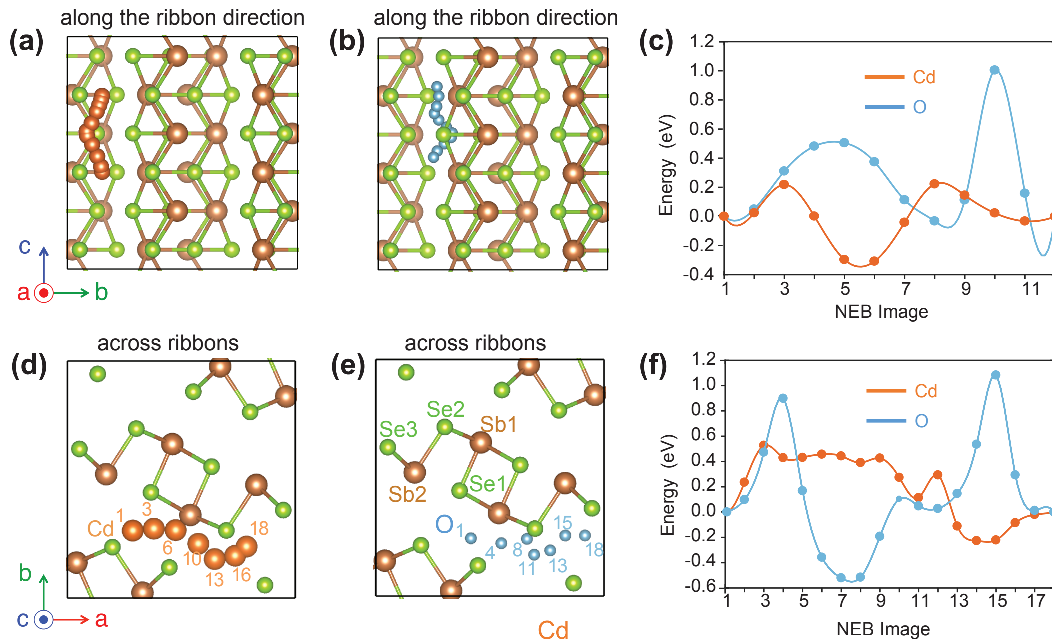

Figure 3.10. Calculated Cd and O diffusion pathways and energy barriers in Sb_2Se_3. (a) Cd and (b) O diffusion along with ribbons. (c) Diffusion energy barrier along with ribbons. (d) Cd and (e) O diffusion across ribbons. (f) Diffusion energy barrier across ribbons. Symmetrically inequivalent Sb and Se sites are labeled in (e), including Sb1, Sb2, Se1, Se2, and Se3.

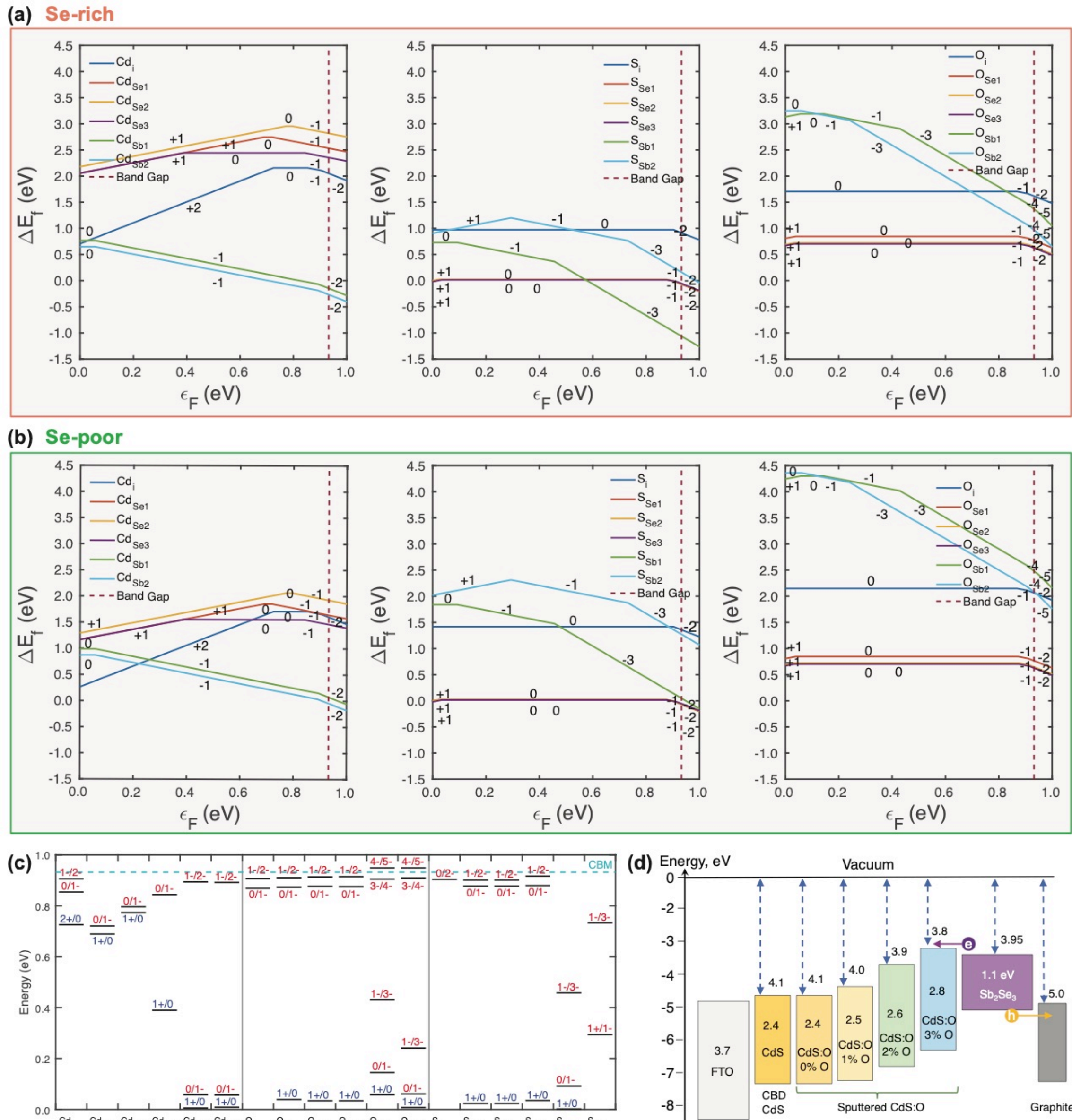

Figure 3.11. Defect analysis of Sb_2Se_3 thin-film solar cells and interface engineering with CdS:O window layer. (a) and (b) The calculated formation energy of point defects as a function of Fermi level for Sb-rich and Se-poor condition, respectively. (c) Transition levels of potential extrinsic point defects in the Sb_2Se_3 absorbers. (d) Band alignment diagram for interfacial engineering with sputtered oxygenated CdS:O at 0%, 1%, 2%, and 3% oxygen partial pressure.

Table 3.7. Diffusion energy barrier for Cd and O across and along with the $(Sb_4Se_6)_n$ ribbons.

Diffusion Element	Energy barrier (eV)	
	across ribbons	along with ribbons
Cd	0.8	0.6
O	1.7	1.0

In experiments, Cd and S could be unintentionally introduced from the buffer layer CdS to the absorber layer Sb_2Se_3. We therefore study the formation energies of three potential impurity elements in Sb_2Se_3, namely O, Cd, and S, and their associated point defects, including substitution and interstitial defect types. Two extreme conditions were considered: (1) Se-rich condition and (2) Se-poor condition, as shown in Figure 3.11a and b, respectively. Since the intrinsic defects in the Sb_2Se_3 absorbers have been investigated,[105] we focus on nine types of extrinsic defects, including three interstitial defects Cd_i, S_i, and O_i and six substitutional defects Cd_{Se}, Cd_{Sb}, S_{Se}, S_{Sb}, O_{Se}, and O_{Sb}. Under the Se-rich condition (Figure 3.11a), O_{Se}, S_{Se}, O_i and Cd_{Sb} have relatively low formation energies below 1.0 eV. For the Cd related defects (e.g., Cd_i, Cd_{Se}, and Cd_{Sb}), the donor defects Cd_i, and Cd_{Se} have relatively high defect formation energy, while the Cd_{Sb} substitutional defect is a shallow acceptor defect with transition level of $\epsilon(-1/0)=0.1$ eV above the VBM (Figure 3.11c). It also shows that Cd_{Sb} could improve the *p*-type conduction of the Sb_2Se_3. However, it was recently reported that the Cd atoms diffusing into the Sb_2Se_3 and forming Cd_i could produce a buried homojunction and lead to *n*-type conduction in Sb_2Se_3.[123] Indeed, our results reveals that, when Cd stays in the vdW gap between $(Sb_4Se_6)_n$ ribbons as Cd_i defect, it becomes shallow donor with a relatively low

defect formation energy (0.7 eV). For the S-induced point defects (*i.e.*, S_i, S_{Sb}, and S_{Se}), both S_i and S_{Sb} have formation energy above 1 eV, but the S_{Se} substitutional defect has almost zero defect formation energy, suggesting that S could randomly replace Se in the Sb_2Se_3. This low S_{Se} substitutional defect formation energy can also be explained by the complete solid solution of ternary $Sb_2(S, Se)_3$.[124] Finally, among three O-related point defects (*i.e.*, O_i, O_{Se}, and O_{Sb}), O_{Se} has the lowest formation energy, indicating that O tends to replace Se. O_i interstitial defect has relatively low formation energy, implying that it is very likely that oxygen will be located at the vdW gaps between the $(Sb_4Se_6)_n$ ribbons. Under the Se-poor condition, the S_{Se} defects have the lowest defect formation energy, and the Cd_i defects are also easy to form due to its low formation energy, while the other defects associated with CdS:O window layers have higher formation energy (above 1 eV). This observation agrees with the reported data that Sb_2Se_3 under the Se-poor condition has poor conductivity and low device performance in general. To improve the device performance, it is necessary to perform post-selenization for the deposited films to suppress the donor defects like Cd_i at the Se-poor condition.[125]

The above first-principles electronic structure calculations indicate that introducing oxygen at the CdS/Sb_2Se_3 interface can form stable O_i owing to relatively low defect formation energy, high O diffusion barrier, and filled the vdW gaps between Sb_2Se_3 ribbons with benign transition levels. The latter can effectively reduce Cd_i induced *n*-type conduction. More specifically, the oxygenated sputtered CdS:O window layer could also provide oxygen to occupy the Se sites (O_{Se}) in the Sb_2Se_3 where O_{Se} has the lowest formation energy without generating detrimental charge defect (Figure 3.11a). Partial

oxygen can also enter into the vdW gaps between the $(Sb_4Se_6)_n$ ribbons, which will block and suppress the Cd diffusion, thereby preventing the formation of Cd_i defect in the bulk of Sb_2Se_3. In fact, the oxygen diffusion barrier across and along ribbons are high (~ 1.7 and 1.0 eV) as shown in Figure 3.10. Therefore, the oxygen will accumulate at the CdS:O/Sb_2Se_3 interface. Considering that Cd_i possesses a shallow *n*-type transition level which is ~ 0.2 eV from CBM (Figure 3.11c), the suppressed Cd_i formation will reduce the *n*-type buried heterostructure. Thus, we can expect the enhanced device performance in oxygenated CdS:O/Sb_2Se_3 devices by tuning the interfacial oxygen composition. The schematic energy band diagram is shown in Figure 3.11d.

3.3.4. Improved Device Performance with Sputtered Oxygenated CdS:O

In light of the above theoretical insights, Sb_2Se_3 absorbers were deposited on sputtered oxygenated CdS:O films at slightly Se-rich condition during the CSS process and investigate the impact of oxygen content in the Sb_2Se_3 solar absorber material. Figure 3.12a shows the UV-Vis absorption spectra of the sputtered oxygenated CdS:O films. The inset shows the optical image of CdS:O films with $O_2/(O_2+Ar)$ of 0%, 1%, 2%, and 3%. The transmittance increases with increasing oxygen partial pressure. The as-deposited CdS, *i.e.*, $O_2/(O_2+Ar)$ ~ 0%, shows a strong absorption at the blue range (<500 nm). The bandgap, indicated by the dashed line in Figure 3.12b, increases from 2.4 eV to 2.85 eV as more oxygen was introduced in the CdS:O layer during sputtering, in agreement with previous reports.[19] The increased bandgap was attributed to the formation of the Cd sulfate ($CdSO_4$) and sulfur compounds ($CdSO_x$) with wide bandgaps.[116] Figure 3.12c shows the XRD pattern of CdS:O/Sb_2Se_3 films deposited at identical CSS conditions by

controlling the oxygenated CdS:O window layers only. The Sb_2Se_3 films show orthorhombic structure (space group *Pbnm*) in agreement with the PDF-0015-0861. To inspect the texture effect by the CdS:O window layer, the texture coefficients (TCs) were calculated, as shown in Figure 3.12d. It was observed that the TCs gradually change to [211]-orientation, while the [120]-orientation was reduced when more oxygen was introduced into CdS:O. The increased TCs of [211]-textured orientation with increasing oxygen in the oxygenated sputtered CdS:O can be associated with the decreased CdS:O grain size and crystallinity. It is known that [211]-textured orientation can benefit the device performance with lower series resistivity.[17]

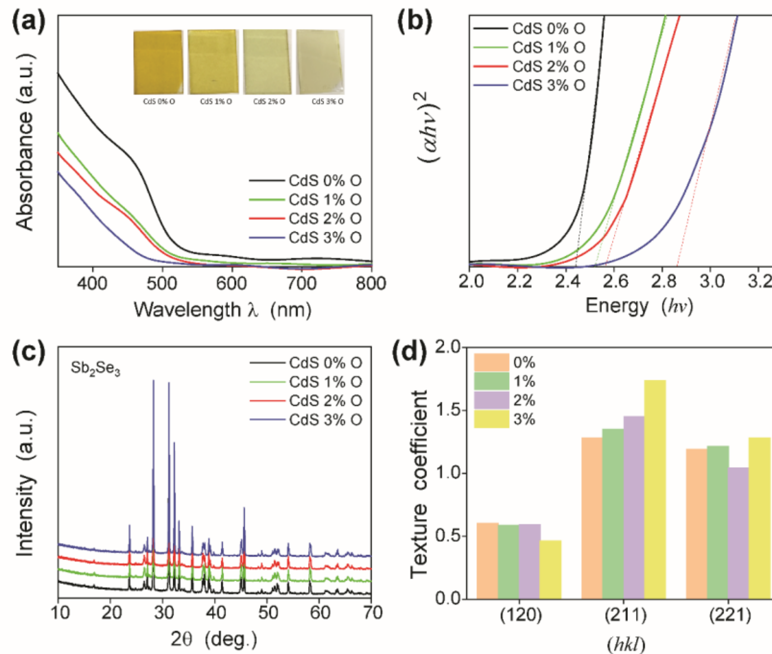

Figure 3.12. (a) UV-Vis absorbance spectra for the oxygenated CdS and the inset shows the oxygenated CdS:O samples with increasing oxygen partial pressure of 0%, 1%, 2%, 3% O_2 during deposition. (b) Absorption coefficient extracted from the optical transmittance. (c) XRD pattern of the CSS deposited Sb_2Se_3 films. (d) Texture coefficient determined from the Sb_2Se_3 films grown on oxygenated CdS:O window layer.

Figure 3.13a shows the *J-V* curves of champion Sb_2Se_3 cells with the CdS:O window layers sputtered with varying oxygen partial pressure at ambient temperature. The corresponding cell parameters were listed in Table 3.8. The best CdS:O/Sb_2Se_3 device was obtained using the window layer sputtered at 2% O_2, where a PCE of 7.01%, a V_{OC} of 0.432 V, an *FF* of 54%, and a J_{SC} of ~ 29.87 mA cm^{-2} were achieved with CdS:O bandgap of ~2.6 eV. Figure 3.13b shows that the EQE curves of these CdS:O/Sb_2Se_3 devices, where the blueshift of EQE at short wavelength is originated from the increased bandgap of sputtered oxygenated CdS:O window layers, while the EQE response at long wavelength (> 900 nm) remains unchanged. Besides the gain at the short wavelength from the increased bandgap of CdS:O, the EQE response at shorter wavelength (*e.g.* from 500 to 900 nm) is also improved to 90% at 570 nm when oxygen partial pressure is increased from 0% to 2%, which can be attributed to the low recombination loss of photoexcited carriers (or long carrier diffusion length) in the bulk Sb_2Se_3 with CdS:O sputtered at 2% oxygen partial pressure.

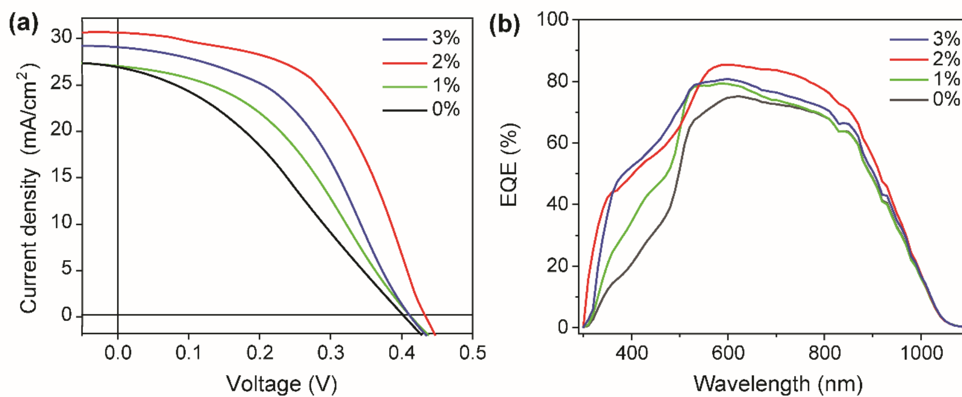

Figure 3.13. (a) J-V curves and (b) EQE curves of FTO/CdS:O/Sb_2Se_3/graphite/Ag solar cells with sputtered oxygenated CdS:O window layers grown in the O_2/Ar+O_2 ratio at 0%, 1%, 2% and 3% at ambient temperature.

Table 3.8. Device performance parameters of FTO/CdS:O/Sb_2Se_3/graphite/Ag solar cells with sputtered oxygenated CdS:O window layers grown in the O_2/Ar+O_2 ratio at 0%, 1%, 2% and 3% at ambient temperature.

CdS:O	V_{OC}, V	J_{SC}, mA cm^{-2}	*FF*, %	PCE, %	R_S, Ω cm^2	R_{SH}, Ω cm^2
0 %	0.402	26.75	33.27	3.59	163.58	1077.55
1%	0.419	26.71	40.34	4.52	146.86	1535.97
2%	0.432	29.87	54.00	7.01	71.26	1916.95
3%	0.424	28.24	46.32	5.56	117.12	1423.92

To characterize the microstructure origin of the improved device performance in CdS:O/Sb_2Se_3 solar cells, scanning electron microscopy (SEM) is employed to analyze the surface morphology and crystallization of Sb_2Se_3 films. Figure 3.14a and b show the top view images of Sb_2Se_3 with CBD CdS and sputtered CdS:O (2%), respectively. The cross-sectional SEM image and EDS elemental mapping are shown in Figure 3.14c for the Sb_2Se_3 grown on sputtered CdS:O film (2%), suggesting that film thickness around 900 nm and the Sb/Se elements stabilize in the film. The grain size of the Sb_2Se_3 film grown on the sputtered CdS:O window layer is larger than that of the Sb_2Se_3 with the CBD CdS window layer, although the CSS growth conditions are identical. The grain size distributions of the two SEM morphology images are shown in Figure 3.14d. The average grain size of Sb_2Se_3 with CBD CdS window layer is about 290 nm, while that of Sb_2Se_3 grown on sputtered CdS:O window layer is about 480 nm. The larger grain size of Sb_2Se_3 on the sputtered CdS:O window layer suggests that the grain growth process is kinetically faster than that of Sb_2Se_3 on the CBD CdS. The surface states of the Sb_2Se_3 grown on the sputtered CdS:O layer was characterized using the X-ray photoelectron spectroscopy

(XPS). The Sb *3d* and Se *3d* spectra in Figure 3.14e and f indicate no clear trace of Sb_2O_3 and residual Se.

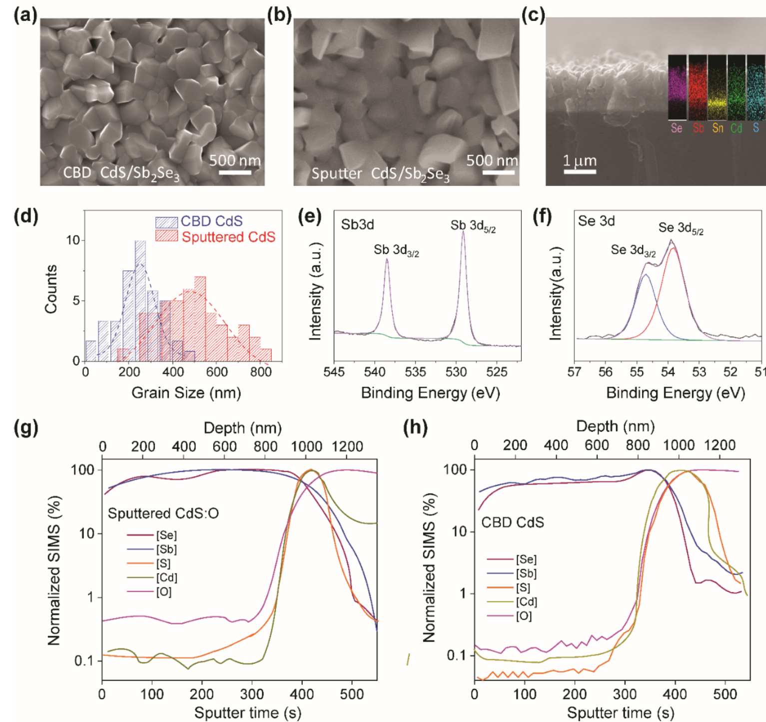

Figure 3.14. (a) and (b) Top view of the SEM images with EDS spectra in the inset of Sb_2Se_3 with the CBD deposited CdS and sputtered oxygenated CdS:O window layer, respectively. (c) Cross-sectional SEM images of the oxygenated CdS:O buffered Sb_2Se_3 with EDS mapping for the selected area. (d) Histogram distribution of grain size for CBD and Sputtered oxygenated CdS buffered Sb_2Se_3 film. (e) and (f) XPS data for the Sb *3d* and Se *3d* in the oxygenated CdS/Sb_2Se_3 film; and (g)-(h) SIMS spectra for the sputtered oxygenated and CBD CdS based Sb_2Se_3 devices, respectively.

The local oxygen distribution at the interfacial area of these devices is investigated by secondary ion mass spectroscopy (SIMS) measurement. Figure 3.14g-h show the SIMS spectra of Sb, Se, Cd, S, and O in CBD CdS/Sb_2Se_3 and sputtered CdS:O/Sb_2Se_3 devices, respectively. We may rule out the substrate temperature influence since it is identical during Sb_2Se_3 CSS deposition. However, the oxygen level is higher and the Cd level is

lower in Sb_2Se_3 with the sputtered CdS:O window layer than those with the CBD CdS window layer, confirming our theoretical results and suggesting that the oxygen from the CdS:O layer can suppress the Cd diffusion into Sb_2Se_3 at the junctions and prevent *n*-type buried homojunction located deep inside the Sb_2Se_3 absorber due to Cd interstitials.[123] Note that the oxygen in the sputtered oxygenated CdS:O window layer is in the SO_x^{2-} bonding environments, while the oxygen in the CBD CdS may be in trace level which is not incorporated with the Cd and S ions.[126] Thus, higher oxygen concentration gradient at the interface of CdS:O/Sb_2Se_3 will drive a deeper oxygen diffusion in the Sb_2Se_3 and block the Cd diffusion.

3.3.5. Conclusions

In summary, through a combined theoretical and experimental study, we have demonstrated an effective interface engineering approach to increase the Sb_2Se_3 photovoltaic device performance by employing sputtered oxygenated CdS (CdS:O) as a window layer. The open circuit voltage, photocurrent, and fill factor are all improved with the best PCE of ~7.01% (V_{OC} of 0.432 V, *FF* of 54%, and J_{SC} of ~ 29.87 mA cm^{-2}) in the CdS:O/Sb_2Se_3 device. The benefit of the sputtered oxygenated CdS:O window layer for the Sb_2Se_3 devices originates from the improved bandgap of CdS:O with high resistivity of $CdSO_x$, and the higher transmittance that allows more light absorption in the Sb_2Se_3 absorber. Meanwhile, both theoretical calculations and experimental results show that the sputtered oxygenated CdS:O window layer can also prevent the formation of Cd interstitial defects in the Sb_2Se_3 layer owing to the accumulation of the oxygen at the interface between CdS:O and Sb_2Se_3 layers. Our work suggests that the optimization of the window

layer can greatly improve the open circuit voltage and enhance the device performance of the emerging antimony chalcogenide Sb_2Se_3 and Sb_2S_3 thin film solar cells.

3.4. Sb_2S_3 Solar Cell Device Performance

3.4.1. Introduction

Combined theoretical calculations and experimental characterization, we have successfully demonstrated the Sb_2Se_3 based thin-film solar cells with up to 7% efficiency using CSS growth method. Based on the similar approach, the Sb_2S_3 based device performance has also been investigated. As for Sb_2S_3 solar cells, a variety of growth technologies have been developed to achieve high-quality absorber of the ribbons aligned with the buffer layer for desired charge transport.[127] For example, Sb_2S_3 solar cells can achieve PCE of 3.5% with RTE.[128] Recently, high efficiency Sb_2S_3 solar cells using the solution-based process were reported. For instance, sensitized solar cells have PCE of 6.4% using a solution-based technology. Solution processing for highly efficient Sb_2S_3 with PCE of 6.78% to 7.5% with varying starting precursors.[129] Sb_2S_3 solar cell fabricated by ALD in planar structure can achieve PCE of ~5.7%.[130] However, it is highly desired to employ the physical vapor deposition technologies to integrate the Sb_2S_3 into the commercial thin film solar cells manufacturing. In particular, fast deposition techniques with independent control of the substrate and sources temperature are highly demanded for integrating Sb_2S_3 into the high-throughput manufacturing technology. The CSS technique can greatly reduce the cost and improve the absorber quality.[67] Recently, the CSS technology has been successfully applied to Sb_2Se_3 thin film solar cells with PCE of 6.8%.[68]

Herein, the performance of CSS-grown Sb_2S_3 solar cells have been studied. It is demonstrated that Sb_2S_3 can be successfully grown using the CSS technique. The best device performance is 3.8% PCE. Theoretical study based on first-principles DFT was performed to elucidate its electronic and optical property. This work further paves the way of Sb_2S_3 based emerging cost-effective and earth-abundant thin-film photovoltaics for solar energy applications.

3.4.2. Electronic Structure and Optical Property from First-Principles Calculations

The crystal structure of Sb_2S_3 is similar to Sb_2Se_3, which has the orthorhombic structure with *Pnma* space group, as shown in Figure 3.15a. Figure 3.15b shows the calculated electronic structure and orbital-resolved projected density of states (PDOS). The PDOS indicates that the valence band is dominated by S-*p* orbitals and the conduction band is dominated by Sb-*p* and Sb-*s* orbitals. Moreover, the DFT-mBJ results predicted that the indirect and direct bandgap of Sb_2S_3 are 1.71 and 1.74 eV, respectively, which agrees with the experimental optical bandgap (1.56 and 1.71 eV, as shown in Figure 3.15c).

The optical absorption properties were characterized using UV-Vis spectroscopy. The direct and indirect bandgap can be determined as 1.71 and 1.56 eV by extracting the Tauc fitting, as shown in Figure 3.15c and the inset. The experimental direct bandgap is in good agreement with the theoretical calculation. Figure 3.15d and inset are the calculated absorption coefficient of Sb_2S_3 compared with Sb_2Se_3. It is shown that both materials exhibit excellent light absorption, while Sb_2S_3 shows slightly better absorption than that Sb_2Se_3 in higher energy range. Overall, the optical absorption calculation

demonstrates that Sb_2S_3 is a promising absorber material for non-cubic chalcogenide solar cells.

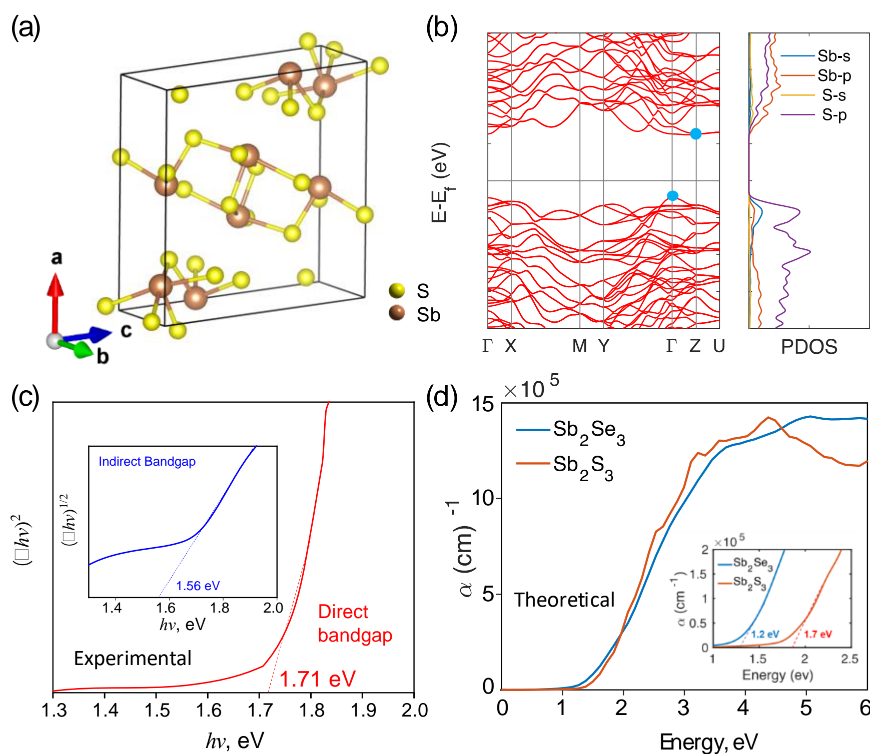

Figure 3.15. Electronic structure and optical absorption of Sb_2S_3. (a) Crystal structure of Sb_2S_3 with *Pnma* space group. (b) Electronic structure and orbital-resolved projected density of states calculated by DFT-mBJ functional. (c) The direct and indirect bandgaps extracted from the optical spectra. (d) Optical absorption coefficients of Sb_2S_3 calculated by DFT-mBJ functional.

3.4.3. Performance of CSS-Deposited Sb_2S_3 Solar Cells

The Sb_2S_3 solar cell was fabricated in an FTO/CdS/Sb_2S_3/graphite cell structure, and their device performance was measured accordingly. Figure 3.16a-c show the energy level alignment, the *J-V* curve, and the EQE of the device, respectively. The typical device performance is listed in Table 3.9. The best device performance is 3.83% with the V_{oc} of

0.66 V, J_{sc} of ~13 mA/cm2 and *FF* of ~44.65%. Therefore, the CSS-grown Sb_2S_3 film device performance is on par with the thermal evaporation deposited Sb_2S_3 solar cells, though still lower than that of the dye-sensitized solar cells.

Table 3.9. Sb_2S_3 solar cell device performance parameters of champion device grown by CSS.

V_{oc}, V	J_{sc}, mA·cm^{-1}	*FF*, %	R_s, Ω cm^2	R_{sh}, Ω cm^2	PCE, %
0.66	13.0	44.65	129.25	1787	3.83

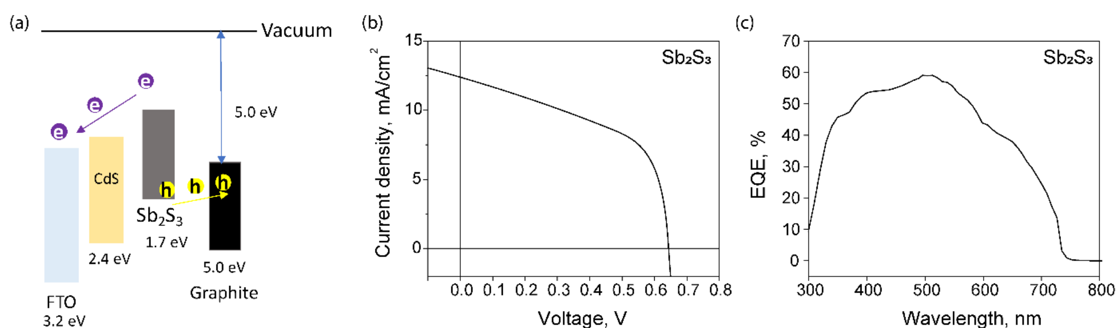

Figure 3.16. Device performance of the Sb_2S_3 solar cells. (a) Illustrative energy level diagram of the layers in the cells. (b) and (c) The *J-V* curve and EQE spectra.

3.4.4. Conclusions

In summary, we demonstrate the Sb_2S_3 thin film solar cells with 3.8% PCE have been successfully fabricated using the scalable close space sublimation deposition technique. The microstructure and optical properties of the CSS grown Sb_2S_3 have been characterized experimentally and studied using theoretical approaches. Our results show that Sb_2S_3 is suitable for large-scale manufacturing at low cost using CSS-like fast vapor transport technology and it is feasible to integrate Sb_2S_3 into the conventional manufacturing process for thin film solar cells. However, the current device performance

is still far below the Shockley-Queisser limit, which has a efficiency of 28.64% for a material with electronic bandgap of 1.7 eV. The main challenge remain in the low V_{oc} and FF. Two critical issues need to be addressed in the future research: high quality absorber layer with less defects and optimal doping density; and high mobility at the interface through interfacial engineering.

4. PHASE-CHANGE VANADIUM DIOXIDES FOR NEUROMORPHIC COMPUTING*

4.1. Introduction

Vanadium dioxide is a strongly correlated electron material, which is well-known for its metal-to-insulator transition (MIT) coupled with a structural phase transition (SPT). Actually, many compounds in the strongly correlated V-O system, such as VO_2, V_2O_5, V_3O_5, and V_8O_{15},[131] exhibit the typical MIT. However, VO_2 has obtained the most extensive investigation since its discovery in 1959,[132] owing to its phase transition temperature (T_c) located at a conveniently accessible temperature ($T_c \approx 340$ K) with the resistivity change of 3-5 orders of magnitude. A thermal hysteresis occurs upon heating and cooling because the transition points of the two processes does not coincide with each other. The MIT can be driven not only through heating or cooling, but also by element doping[7], electric field gating[133], strain[134], and intense optical field.[135] The sharp changes in electrical, optical, magnetic and thermal properties upon MIT endow VO_2 with great possibility in the applications such as neuromorphic computing, thermometry and sensing.

*Part of this chapter is reprinted with permission from "Atomic Hourglass and Thermometer Based on Diffusion of a Mobile Dopant in VO_2" by D. G. Sellers, E. J. Braham, R. Villarreal, B. Zhang, A. Parija, T. D. Brown, T. E. G. Alivio, H. Clarke, L. R. De Jesus, L. Zuin, D. Prendergast, X. Qian, R. Arroyave, P. J. Shamberger and S. Banerjee, Journal of American Chemistry Society 142, 15513 (2020). Copyright © 2020, American Chemistry Society.

4.1.1. Crystal Structure of Vanadium Dioxides

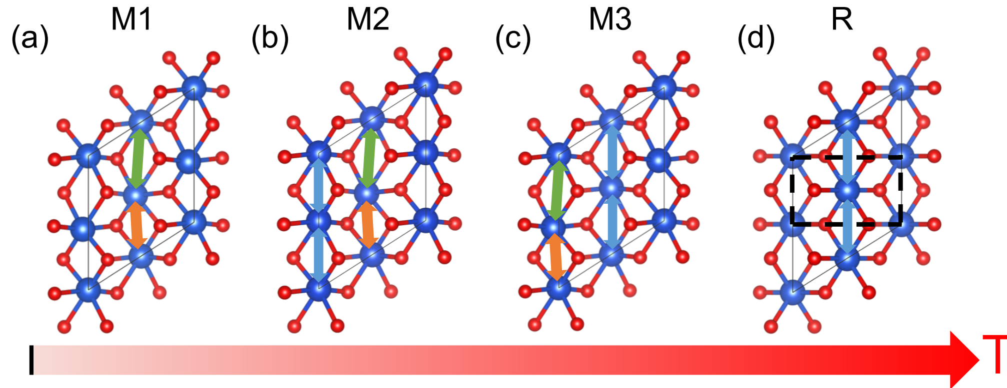

Figure 4.1. Crystal structures of different polymorphs of VO_2. (a) Low-temperature insulating M1 phase. (b) High-temperature metallic R phase. (c) Intermediate M2 and (d) M3 phases with alternating dimerized/undimerized V-V chains.

VO_2 can exhibit many different crystal structures upon different growth conditions. Among those polymorphs, the M1 and R phases are the major ones due to the reversible transition near room temperature. Above T_c, VO_2 adopts a tetragonal rutile (R) phase with space group $P4_2/mnm$; below T_c, the crystal structure is monoclinic (M1) with space group $P2_1/C$. The semiconducting M1 structure is characterized by a doubling of the unit cell volume compared to the rutile, and a dimerization pattern of V chains along the c-direction of the parent rutile phase, which shows a zig-zag pattern, as shown in Figure 4.1a. The experimentally measured bond lengths of the two V-V chains are 2.65 Å and 3.12 Å, respectively.[136] The highly symmetrical metallic rutile phase, in contrast, shows equal V-V bond length (Figure 4.1b), with the bond length of 2.85 Å.[137] By the contrary, the oxygen atom positions are only slightly perturbed in the MIT process. The low-temperature M1 phase has an insulating bandgap of 0.6-0.7 eV. Additional insulating

phases such as M2 and M3 have also been discovered through experiments, which can be stabilized under certain conditions. Those phases are characterized by alternating dimerized/undimerized V-V chains (Figure 4.1c and d).

4.1.2. Phase Transition Mechanism: Peierls vs. Mott Scenarios

The mechanism of the MIT phase transition in VO_2 has been a focus of research for a few decades. Despite great effort, a complete understanding of the transition mechanism remains elusive. Over the years, the controversial issues mainly confront two alternate scenarios: a lattice distortion driven (Peierls-like) transition vs. an electron correlation driven (Mott-like) transition.

4.1.2.1. Peierls Scenario

Peierls' theorem states that a 1D crystal with a periodic lattice is not stable, and a lattice distortion occurs at low temperature. This theorem is espoused by Rudolf Peierls in the 1930s.[138] The Peierls instability of a 1D metal is the consequence of strong electron-phonon coupling. In the absence of electron-electron and electron-phonon interaction, the lattice of the ground state 1D metal is a periodic array of atoms with lattice constant a. However, due to electron-lattice coupling, a periodic lattice distortion in the 1D metal is energetically favorable, and the period λ is related to the Fermi wave vector k_F by $\lambda = \frac{\pi}{k_F}$, where $k_F = \frac{\pi}{a}$. Consequently, the distortion opens up a bandgap at the Fermi level, thereby lowering the energy of occupied electron states and raising the energy of empty states. When the gain by creating energy gaps overcomes the energy cost of Coulomb and elastic energy, the energy of the whole system is reduced. Therefore, the transition from a conductor to an insulator is self-sustaining.

Goodenough attributed the MIT transformation to the lattice distortion, which can be interpreted as the result of Peierls transition.[139] In Goodenough's model, crystal field and molecular orbital theories were used. The transition metal vanadium has five *d* orbitals, that is, d_{xy}, d_{yz}, d_{xz}, $d_{x^2-y^2}$, and d_{z^2}. When isolated or surrounded by a spherical field, those five orbitals are energetically degenerate. In the presence of an octahedral crystal field, which is the case for rutile VO_2 phase, the 3d orbitals of V are split into three-fold degenerate t_{2g} states, contributed by d_{xy}, d_{yz}, and d_{xz}, and two-fold degenerate e_g states, composed by $d_{x^2-y^2}$ and d_{z^2} orbitals. Due to the orthorhombic component of the local crystal field, the t_{2g} states are further split into two d_π orbitals and one $d_{||}$ orbital. In the phase transformation process, V-V chain dimerization lifts up the π^* state in energy above the Fermi level, and results in the splitting of $d_{||}$ into filled bonding and empty antibonding states (see Figure 4.2). Finally, a band gap appears as the result of lattice distortion driven by the strong electron-phonon interaction. Goodenough's model later on was supported by theoretical calculations using DFT-LDA functional. Wentzcovitch *et al.* calculated the electron and crystal structures before and after the VO_2 phase transformation and the results indicated V-V bond dimerization resulted in the appearance of the electronic gap in M1 phase.[140]

The early description of electronic structure based on band theory proposed by Goodenough qualitatively explained that the V-V chain distortion and dimerization is the cause of the opening of the bandgap, and has provided useful insight. Nevertheless, the MIT in VO_2 seems to be more complex and Peierls transition fails to explain several behaviors. For example, this mechanism is unable to explain a bandgap of 0.6 eV in M1-

VO_2,[140, 141] the magnetic properties for all phases,[142] and the existence of other polymorphs besides M1 and R phases.[143] These facts led to an alternative description based on electronic correlation rooted in Mott-Hubbard theory.

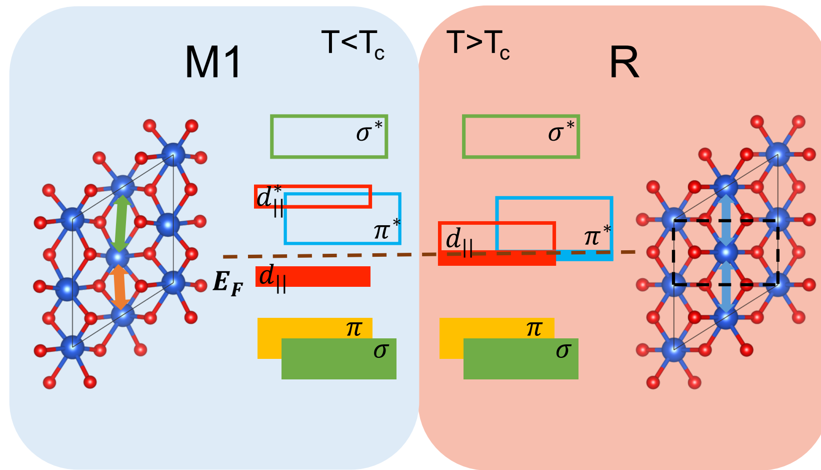

Figure 4.2. Schematic of the electronic band structures of R-VO_2 and M1-VO_2 based on Goodenough's model.

4.1.2.2. Mott Scenario

The conventional DFT calculations assume that the electron-electron interaction can be represented by an average periodic effective potential. The electron-electron repulsion in the Kohn-Sham equation is based on a single-particle approximation. However, when dealing with d and f electrons, the exchange-correlation functional based on the single-particle approximation fails to fully take the correlation effect into consideration. The on-site Coulomb repulsion between these electrons becomes comparable to the single-electron bandwidth, which makes it necessary to include additional correction. Therefore, the band diagrams based on traditional single-band

theory shows no obvious bandgap, which is contradictory to the experimental bandgap of 0.6-0.7 eV.

In 1975, Zylbersztejn and Mott proposed a Mott-Hubbard's model to interpret the phase transition in VO_2.[142] In this scenario, VO_2 is a Mott insulator, and the electron correlations is the primary effect resulting in the opening of the bandgap. An additional Hubbard energy (U) is introduced to take into account the repulsion of *d/f* electrons. It represents the separation of an upper Hubbard band and a lower Hubbard band due to the splitting of a half- or partially filled band caused by the Coulombic repulsion. When the width of the Hubbard band is greater than U, metallic behavior is observed. On the other hand, when the width of the Hubbard band is smaller than U, an electronic bandgap is opened up. The formulation of this concept was first proposed by Mott in the form

$$E_{gap} = U - \frac{1}{2}(B1 + B2),$$

where U is the Hubbard energy, B1 and B2 are the band widths of the empty upper and occupied lower Hubbard bands.

The bandgap obtained from DFT+U method successfully reproduced the experimental value.[144] However, a few questions still remain, such as the failure of predictions of the conduction and magnetism in rutile VO2. Fortunately, as the rapid development of computational methods, other functionals such as hybrid functionals have been employed to this system. Those functionals are more capable of describing the electronic and magnetic properties of VO2 due to the more accurate description of exchange-correlation energy.[145, 146]

4.1.3. Modulation of MIT in VO_2

The uncontrollable phase transition temperature of VO_2 (T_c ~ 340 K) limits its practical applications. Therefore, multiple approaches have been investigated for the modulation of VO_2 MIT. For example, element doping is a common method to tune the carrier density in materials, and has been demonstrated as an effective way to regulate the phase transition temperature and modify the energy landscape of VO_2 in terms of phase stabilities and transformation barriers.[147, 148] Extensive work has been focused on extrinsic doping by substituting the vanadium atom with another metal element. Typically, a substitutional metal dopant with the valence higher than 4+ of vanadium tends to lower the MIT temperature, while dopants with the valence less than 4+ is likely to increase the transition temperature. It is because electron donors tend to screen the electron-electron correlation in the insulating phase, hence reducing T_c; electron acceptors, on the other hand, weakens the screening, thereby promoting T_c. Among those metal dopants, a lowest T_c has been achieved in W-doped VO_2, in which the heating T_c locates at ~310 K and the cooling T_c locates at ~250 K.[149] Ge doping significantly increase the transition temperature, and the highest T_c is up to 400 K.[150] Additionally, there are also other approaches reported to be powerful for MIT regulation, such as strain engineering,[151, 152] external electric field,[152] electrical current heating,[153] light irradiation,[154] *etc*.

4.1.4. Application of VO_2 in Neuromorphic Computing

VO_2 and NbO_2 have been favorite materials to emulate neurons in the solid state owing to their pronounced MIT by strong electronic correlation coupled with a structural phase change. Their capability of emulating neural circuits have been demonstrated

through both experiments and simulations very recently.[36-39] Compared to NbO_2 with MIT temperature as high as 1081 K, the MIT in VO_2 occurs at a more accessible temperature of around 340 K. Nevertheless, the operating temperature of modern computing architectures is around 400 K,[124] which indicates that NbO_2 has a transition temperature that is too high and consumes too much energy, whereas VO_2 has a transition temperature that is too low for practical applications of neuromorphic computing. In order for these materials to serve better in the devices, it is worth conducting comprehensive study of the mechanism of their MIT via different modulation methods, such as element doping, strain, interfacial charge and external field. Our research mainly focuses on doping for tuning the phase transition in VO_2. Using combined theoretical calculations and experimental characterization, we systematically investigate the doping mechanism of a series of elements.

4.2. Assessment of DFT Functionals for Predictions of VO_2 Properties

The debate of whether the strongly correlated VO_2 could be described by band theory is still not settled yet. In order to study the MIT mechanism of VO_2, we assessed the capability of a variety of DFT functionals for the predictions of VO_2 structural, electronic and magnetic properties. We first calculated the lattice constants, electronic structures and magnetic orders of insulating monoclinic (M1) and metallic rutile (R) VO_2 based on PBE+U method. In strong correlated materials, one reason for the failure of DFT is the delocalization or self-interaction error. This can be partially fixed by adding a Hubbard U using the DFT+U approach. A Hubbard U of 3 eV is applied here to correct the PBE functional as proposed by Dudarev *et al*.[155] The results are summarized in

Table 4.1. Similar results have been reported in a few references.[145, 156-158] PBE+U recovers the insulating state of M1 phase (bandgap of 0.7 eV) and metallic R phase upon exclusion of spin polarization. It also gives quite accurate results for structural parameters. However, the R-M1 energy difference disagrees with experiment. PBE+U with spin polarization fails to capture the dimerization of V-V chain in the M1 phase. The nonmagnetic M1 phase has a bandgap of 1.1 eV which is larger than the experimental value (0.6-0.7 eV). Additionally, PBE+U gives a ferromagnetic state for R phase with a bandgap of 0.9 eV. In conclusion, PBE+U functional is not able to describe simultaneously the structure, energy, magnetic and electronic properties of the two stable polymorphs.

Table 4.1. PBE+U method calculated lattice constants, electronic bandgaps, and magnetic orders of monoclinic (M1) and rutile (R) VO_2 with and without spin polarization compared to experiments.

	Methods	Magnetic order	a	b	c	α, γ	β	Bandgap (eV)
M1	Expt.[136]	NM	5.75	4.45	5.38	90	122.65	0.6-0.7
	PBE+U	N/A	5.45	4.63	5.40	90	117.58	0.7
	PBE+U+spin	NM	6.05	4.52	5.44	90	123.77	1.14
R	Expt.[137]	NM	4.55	4.55	2.85	90	90	metallic
	PBE+U	N/A	4.62	4.62	2.77	90	90	metallic
	PBE+U+spin	FM	4.51	4.51	3.04	90	90	0.9

Recently, hybrid functionals have attracted a lot of attention as they often provie better description of the physical properties of many semiconductors and insulators, including VO_2. Hybrid functionals provide more accurate description for exchange-

correlation energy because of the incorporation of a portion of exact exchange. It has been demonstrated that Heyd-Scuseria-Ernzerhof (HSE) functional could correctly describe the electronic and magnetic structures of VO_2 phases.[145] One of the characteristics of M1-VO_2 is the V-V dimerization. According to our HSE calculations, HSE06 functional is capable of capturing the dimerization with the bond lengths of 2.87 Å and 3.11 Å, which is in agreement of experimental observations. However, upon inclusion of spin polarization, HSE functional gives a magnetic ground state for the M1 phase and a nonmetallic ground state for R phase. Additionally, the R-M1 energy difference is in significant disagreement with experiment.[159]

Table 4.2. Calculated V-V bond lengths compared to experimental data.

	V-V bond lengths
Expt.[136]	2.65, 3.12
PBE-U	3.024, 3.025
HSE06	2.87, 3.11
PBE0	2.44, 3.14

Very recently, an unified band theory with modified hybrid exchange functional PBE0 was proposed which provides the structure, electronic and magnetic properties of the M1, M2 and R phases consistent with experiments.[146] The difference between PBE0 and HSE06 functionals lies in the exchange-correlation energy functional. The exchange-correlation energy in PBE0 functional is given by

$$E_{xc}^{PBE0} = \frac{1}{4}E_x + \frac{3}{4}E_x^{PBE} + E_c^{PBE},$$

where E_x^{PBE} and E_c^{PBE} denote the exchange and correlation parts of the PBE energy functional, respectively. The exchange-correlation energy in HSE06 functional is written as

$$E_{xc}^{HSE06} = \frac{1}{4}E_x^{SR}(\mu) + \frac{3}{4}E_x^{PBE,SR}(\mu) + E_x^{PBE,LR}(\mu) + E_c^{PBE},$$

where the electron-electron exchange interaction is separated into a short- and long-ranged part, labeled *SR* and *LR*, respectively. The range separation is defined by the parameter screening factor μ. Two important parameters are introduced to their approach: (1) harder pseudopotentials for both oxygen and vanadium – 13 electrons were treated as valence electrons for V ($3s^2 3p^6 3d^4 4s^1$) and 6 electrons were treated for O ($2s^2 2p^4$) with smaller core radius; and (2) a tuned mixing parameter for exchange-correlation potential with 7% exact exchange. Based on this approach, we successfully reproduced experimental lattice constants, electronic structures, and magnetism (see Table 4.3). Additionally, the method outperforms DFT+U and HSE06 in terms of the success of capturing dimerized V-V chain in M1 phase. Table 4.2 summarizes the V-V bond lengths from different functionals. The PBE0 with harder pseudopotentials provides the V-V bond lengths that are in good agreement with experimental data.

In conclusion, our study shows that VO_2 exhibits the unusual large coupling between magnetic and structural degrees of freedom, that is magneto-elastic coupling, in the sense that the initial magnetic state has strong influence on the optimized crystal structures.

Table 4.3. Lattice constants, electronic bandgaps, and magnetic orders of monoclinic (M1) and rutile (R) VO_2 calculated by PBE0 with 7% Hartree-Fock exchange functional.

	Magnetic order	a	b	c	α, γ	β	Bandgap (eV)
M1	NM [Expt.][136]	5.75	4.45	5.38	90	122.65	0.6-0.7
	NM	5.53	4.51	5.28	90	121.93	0.63
R	NM [Expt.][137]	4.55	4.55	2.85	90	90	metallic
	FM	4.42	4.42	2.80	90	90	metallic

4.3. Native Defects in M1 VO_2

It is demonstrated that oxygen non-stoichiometry can affect the physical properties in VO_2.[148] For example, the MIT temperature is sensitive to the stoichiometry. The T_c is reduced with oxygen deficiency and increased with oxygen enrichment.[160] The carrier density can also increase with oxygen deficiency, as oxygen vacancies are electron-donor defects and introduce more free electrons to the insulating VO_2. Actually, the native defects in semiconductors, including vacancy, antisite and interstitial defects, not only donate free carriers, but also trap and scatter free carriers, hence playing an important role in the materials electrical and thermal conductivities. In this dissertation, based on first-principles calculations, we systematically investigated the intrinsic defects in insulating monoclinic VO_2. Our results revealed the dominate defects and their impact on the physical properties, and suggested the favorable growth condition to suppress the harmful defects formation. We also provided an understanding of the effect of native defects on the MIT.

The atomistic, electronic structures and total energies were calculated using first-principles DFT as implemented in the VASP. [51,52] The projector augmented wave (PAW)[53] method was used to describe the electronic configurations of the relevant elements and the exchange-correlation energy functional was modeled using the GGA with the PBE form.[54] A plane wave basis set with an energy cutoff of 533 eV was employed. Considering the strongly correlated d electrons for vanadium, a Hubbard parameter U is applied to the PBE functional in the approach proposed by Dudarev *et al.*[55], with $U_{\text{eff}} = 3.4$ eV. This value of U captures the insulating nature of the monoclinic polymorph and the metallic nature of the tetragonal polymorph. We did not use hybrid functional as their computational cost is too high for large supercell. The doped 97-atom supercells were generated by replicating the monoclinic and rutile unit cells by 2×2×2 and 2×2×4, respectively. The pristine $V_{32}O_{64}$ supercells were fully relaxed. The convergence tolerance for electronic relaxation was set to 10^{-7} eV, and the maximum residual force for ionic relaxation was set to <0.01 eV $Å^{-1}$. A Monkhorst-Pack mesh with at least 5000 k-points per reciprocal atom was used for the Brillouin zone integration.

To mimic the dilute limit, the unit cell structure is enlarged to 2×2×2 supercell, and due to the high computational cost the k-point sampling is reduced to 2×2×2 accordingly. Spin polarization is included for all the defect calculations. The defect formation energy is defined by $\Delta E^f(D,q) = E(D,q) - E(\text{bulk}) - \Sigma n_i \mu_i + q(\epsilon_F + \epsilon_{\text{VBM}}) + E_{\text{corr}}$,[56] where $E(D,\text{q})$ and $E(\text{bulk})$ refer to the total energy of the pristine host cell and the supercell with defect D in charge state q, respectively. μ_i is the chemical potential of species i involved in the defect, and n_i is the number of the atoms added ($n_i >$

0) or removed ($n_i < 1$). Herein, we consider three types of defects: vacancies, substitutional defects, and interstitial defects. $q\epsilon_F$ represents the electron reservoir, and ϵ_F is the Fermi level with respect to the valence band maximum ϵ_{VBM} in the perfect cell. The range of the chemical potential for each species is determined by the stability of VO_2 relative to the elemental phases and other competing compounds. The last term E_{corr} in the above equation is the correction to the formation energy caused by the interaction between the defect charge and its images and the potential alignment between the defect and host cells under the periodic boundary condition employed in the DFT calculations.[57] More details for point defect calculations is presented in Chapter 2.

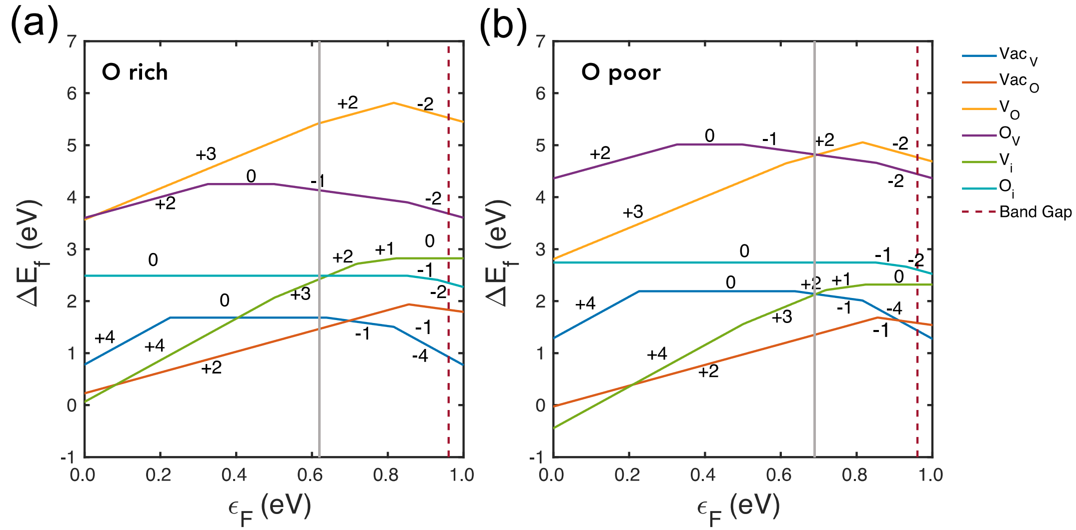

Figure 4.3. Native defect diagrams under (a) O-rich and (b) O-poor conditions. The grey line indicates where Fermi level is pinned by the native defects.

The results are summarized in Figure 4.3. Each line represents each defect type and the slope of the line reflects the charge state. As for the chemical potential, we consider two extreme conditions, that is, O-rich and O-poor conditions. The donor defects oxygen

vacancies (Vac_{O}) and vanadium interstitials (V_i) are dominant in the O-rich condition. These two defects have even lower formation energies in the O-poor condition. In both cases, the antisite defects V_O and O_V are difficult to form. To suppress the formation of Vac_O and V_i, o-rich growth condition is recommended. The presence of native donor defects contribut electrons to conduction bands, and result in the n-type conductivity in M1 VO_2. The conductivity can be increased when more native defects are introduced.

Our results are consistent with experimental observations.[148] It is found that when more native defects are introduced, the insulating phase has higher conductivity, attributed to more free electrons donated by donor defects. On the other hand, the metallic phase becomes less conducting when more native defects are present, owing to the reduced mobility of free carriers.[161] Additionally, the native defects can affect the MIT characteristics. It is found that the vacancies can serve as new phase nucleation sites in the first-order phase transformation.[162, 163] Therefore, the MIT hysteresis can be narrowed or widened through introduction of more defects or suppression of defect formation. For example, in single-crystal VO_2 nanoparticles, the defects created by high-energy ion irradiation facilitates the MIT and moderates the super-cooling and super-heating.[163] And substitutional incorporation of tungsten in VO_2 increases the hysteresis and induces greater super-cooling, resulting from a decrease of oxygen vacancy density.[149]

4.4. Extrinsic Doping in VO_2

For the application of memristor in neuromorphic computing, two characteristics of VO_2 MIT requires to overcome: the transition temperature that is below the operation temperature of modern computing units, and the uncontrollable thermal hysteresis width

(ΔT_c). [124] A smaller hysteresis suggests less energy dissipation and faster dynamics, while a larger hysteresis benefits nonvolatile on/off states.[7] Through extrinsic doping, deterministic control over ΔT_c can be achieved. In the following section, we will discuss the impact of extrinsic doping in boron- and germanium-VO_2 on the MIT from the perspective of point defects.

4.4.1. Extrinsic Defects in B-doped VO_2

Experiments show that incorporation of mobile boron interstitials dopants weakly coupled to the crystal lattice provides a means of dynamically modulating the MIT temperature in VO_2. Specifically, a remarkable time- and temperature-dependent evolution of the relative phase stabilities of insulating monoclinic (M_1) and metallic rutile (R) phases of VO_2 in an “hourglass” fashion is observed as interstitial boron species relax from high-energy sites wherein they are situated upon a thermally induced phase transition. The relaxation process corresponds to a 50°C range of the transition temperature achieved within the same sample as a function of residence time and temperature. The dynamic modulation of the transition temperature is explicable considering that the most energetically favored sites for B atoms vary throughout the transition between the M_1 and R polymorphs with an intermediate metastable trigonal state (Figure 4.4). Given sufficient time and thermal energy, the metastable state can relax through a thermally activated process to the lowest-energy quasi-equilibrium state of the M1 phase, which is substantially lower in energy as compared to the metastable state and thereby transitions at a higher temperature.

Given the absence of significant changes in the average structure of the VO_2 lattice and in light of the relatively long relaxation timescales between metastable and quenched states, the specific sites occupied by B atoms warrant further attention and have been evaluated with the help of DFT calculations at the GGA+Hubbard U theory level. While DFT is limited in its treatment of electron correlated materials, the large supercells required to model the low dopant concentrations render the materials here intractable by dynamical mean field theory approaches.[164, 165] We have converged on a U parameter (U = 3.4 eV) that captures the electronic structure of the two polymorphs (Figure 4.6a-b). The use of a large unit cell and a U parameter that accounts for electron correlation enables us to use the DFT calculations to guide spectral interpretation and to develop a physically intuitive albeit inevitably reductionist (in the absence of accurate determination of energetics) model of the phenomena under consideration.

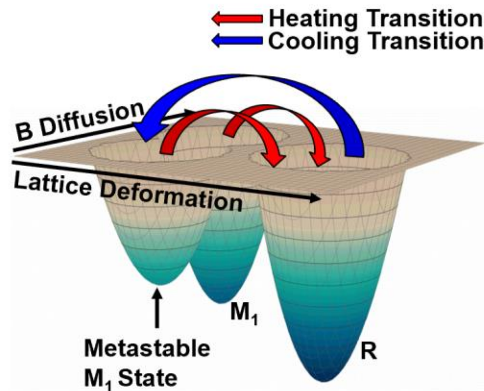

Figure 4.4. Illustration of energy landscape of the MIT transition as a function of temperature of the system and diffusion of B atoms between interstitial sites.

Within their respective unit cells, six M_1 and three R unique interstitial sites have been identified by applying symmetry operations (defined by the respective space groups)

on the 68 geometrically determined sites located using the AFLOW software package.[166] The formation energies (E_f) of each unique interstitial site has been calculated using DFT such that E_f is defined as:

$$E_f = E(BVO_2) - E(VO_2) - E(B),$$

where $E(BVO_2)$ is the total energy of a VO_2 supercell containing one B atom ($BV_{32}O_{64}$, corresponding to 3.1 at.% B incorporation in VO_2), $E(VO_2)$ is the energy of an undoped VO_2 supercell, and $E(B)$ is the energy of a single B atom based on a 36 atom unit cell. This supercell size is in the range of experimentally observed B concentrations while still being computationally tractable in DFT+U calculations. Upon transition from a rutile state, the doped supercell adopts a metastable distortion around the boron atom that does not occur when substituting boron into a monoclinic M1 lattice as a starting point. To simulate the generation of possible metastable states caused by the boron defect across the R to M1 phase transition, a rutile-like configuration was used as a starting point for the relaxation. This structure was generated by shifting the vanadium atoms of a monoclinic supercell by linear interpolation towards the R structure, which increases uniform spacing along the *c*-axis and reduces twisting of the vanadium pairs. From this starting configuration, the ions were relaxed back to a monoclinic configuration resulting in the metastable M1 configuration. This metastable state has a different lowest energy configuration for the boron position than is found in the relaxed monoclinic M1 phase or the R phase. Figure 4.5a-c depict the lowest energy interstitial sites for B atoms in the R phase, metastable M1 phase, and relaxed M_1 phase, respectively. Figure 4.5e shows normalized E_f values for the interstitial locations of B sites in the R and metastable M_1, and M_1 supercells where M1(1)

and M1(1)* as well as M1(5) and M1(5)* are the symmetrically equivalent sites with the asterisk denoting the metastable M1 distortion. All stable sites have a tetrahedral coordination with neighboring oxygen atoms, except the trigonally-coordinated M1(6)*, which is the lowest energy boron position of the distorted metastable M1 state shown in Figure 4.5c. The three lowest energy sites highlighted in red in Figure 4.5e are posited to correspond to the path traversed by boron atoms from the transition from rutile to unrelaxed monoclinic to relaxed monoclinic. Notably, a small thermal population of boron atoms may occupy higher energy sites, but given the relative energetics the most stable sites are expected to be strongly favored.

To better understand the nature of the interstitial boron atoms, the formation energies have been evaluated for different charged states of boron and contrasted to the stability of substitutional defects on the cation and anion sublattice. Figure 4.5f and g show the defect diagrams of boron associated interstitial and substitutional defects under O-rich and O-poor conditions, respectively. The equilibrium Fermi level is determined from the native defects (Figure 4.3) at synthesis temperature. The Fermi level under O-rich and O-poor condition is pinned around 0.5 eV and 0.55 eV at synthesis temperature. In both environments the most stable defect is a 3+ charged boron interstitial defect (B_i) although a substitutional boron on the vanadium site (B_V) may be occupied with some probability as a minority defect type. The density of states for the monoclinic and rutile phases are shown in Figure 4.6a-b, confirming that the calculations accurately capture the insulating nature of the monoclinic phase and the metallic nature of the rutile phase.

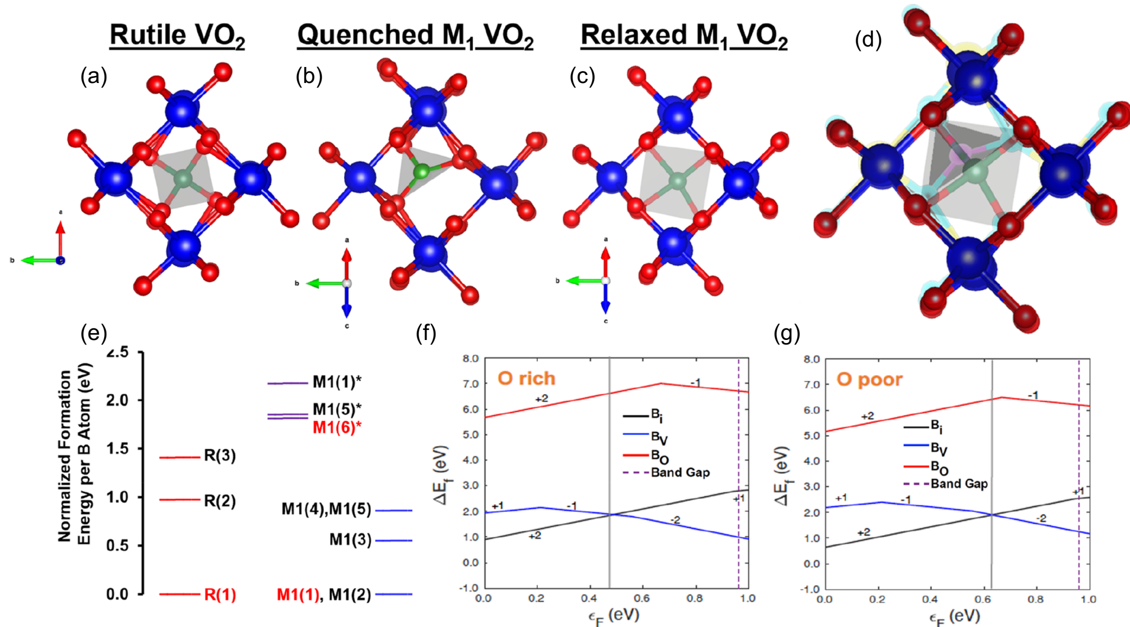

Figure 4.5. Energetics of boron interstitial sites in VO_2 and delineation of spectroscopic signatures. (a)−(c) DFT calculated coordination environments for B-doped VO_2, illustrating the most thermodynamically favorable interstitial sites for B incorporation for R (A, R(1)), quenched M1 (B, M1(6)), and relaxed M1 (C, M1(1)). Vanadium atoms are depicted as blue spheres, oxygen atoms as red spheres, and B atoms as green spheres. (d) Overlay of quenched (inverted) and relaxed (blue/red/green) states to illustrate distortion (e) Normalized formation energies of B incorporation into different interstitial location within the R (red), metastable M1 (violet), and relaxed M1 (blue) supercells. Panels (f) and (g) display the formation energies of charged defects for oxygen rich and oxygen poor conditions, respectively. The energies were calculated for substitutional boron defects at the oxygen sites (B_o), substitutional boron defects at the vanadium sites (B_v), and interstitial boron defects (B_i). For both oxygen-rich and oxygen-poor environments, the most stable defect at the calculated Fermi level (Figure 4.3) of ϵ_F = 0.48 and 0.62 is a 2+ interstitial boron defect B_i.

We note in Figure 4.3a and b that (+1/−1) transition levels of B_V are located ~0.2 eV above the valence band maximum, which is potentially indicative of negative U behavior. A similar behavior is observed for substitutional boron atoms in lattice oxygen sites (B_O). As such, further analysis is warranted to determine the origins of this unusual

form. Conventional negative U behavior is often associated with localized charges created around defects and the significant local relaxation of the lattice in proximity of the defect. In our case, we find neither localized charge states nor large lattice relaxations near the B atom. Figure 4.6c and d plots the charge density of the top valence band states for various charged B_V defects (+2, +1, 0, −1, and −2). The valence electrons are not localized around the boron defect but are instead seen to be delocalized across the lattice, as expected in the case of shallow defects. Indeed, this is consistent with the orbital-resolved DOS plot in Figure 4.6e-h, which reveals that the electronic states associated with the B atom are localized deep within the valence band and are thus unlikely to contribute to the valence/conduction states near the Fermi level. Hence, the charged defects do not have a charged state localized on the defect atom as often observed in the case of deep defects of large bandgap insulators. In light of the absence of localized electronic states on the B atom, no strong B-related lattice relaxation is expected. Hence, the "negative U" like behavior observed in the defect formation energy diagram is not a result of Anderson's lattice relaxation. In other words, although DFT+U captures the essentials of the band gap of the M1 and R phases of VO_2, it is still challenging to predict the total energy of such strongly correlated system accurately, which is beyond the scope of this work. The large size of the unit cell renders this system intractable to more accurate dynamical mean field theory approaches.

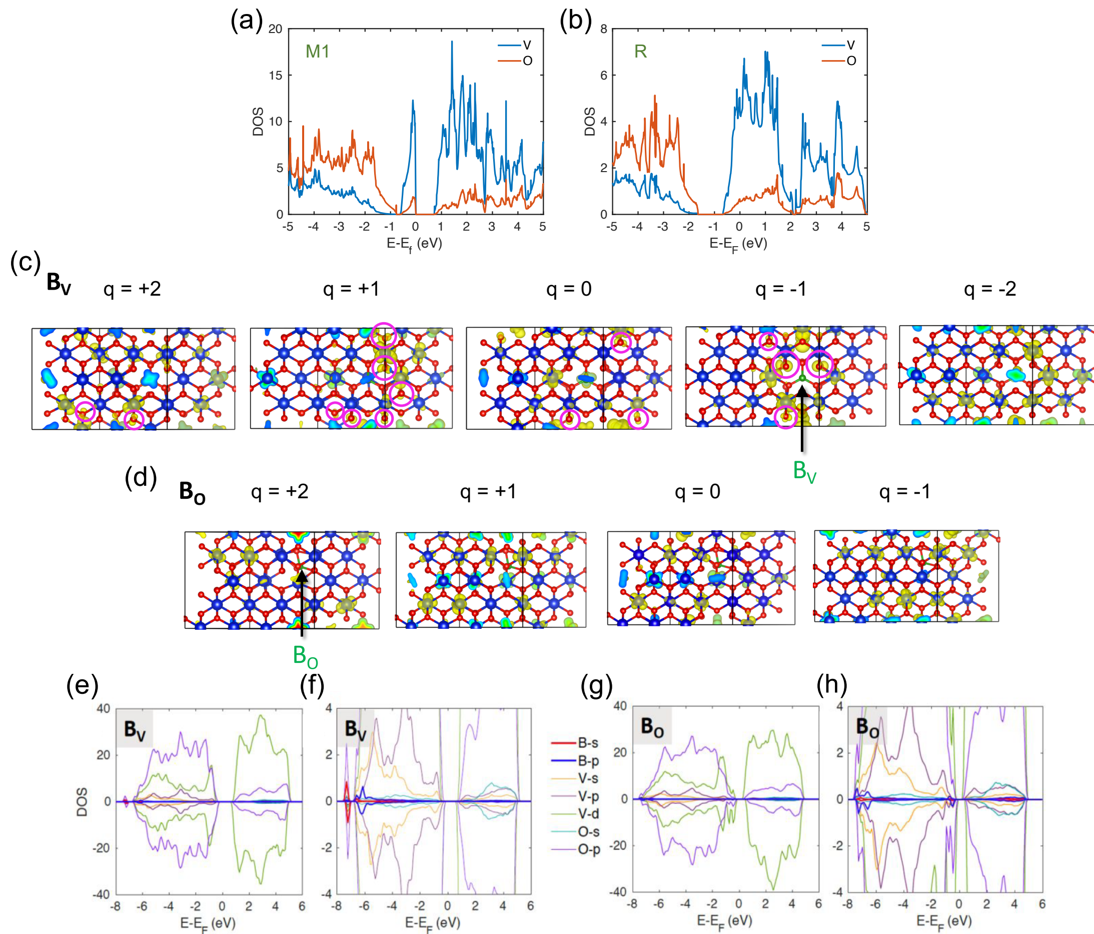

Figure 4.6. Density of states for (a) M1 and (b) R phases respectively, using a U value of 3.4 eV, which captures the insulating nature of the M1 polymorph and the metallic nature of the rutile polymorph. Charge density of the highest energy valence states for (c) B_V and (d) B_O defects with various charge states. In all cases, the charge is delocalized on V and O atoms instead of being localized around the B atom, which is expected from shallow defects. Purple circles indicate the electron density on oxygen atoms in the B_V defect cell. Analogous to the discussion of the B_V defect, the charges associated with B_O defect are delocalized also indicated in the also the 0 charge state orbital-resolved DOS plots for (e)-(f) B_V and (g)-(h) B_O defects. Hence, no significant lattice distortion is observed in proximity of the B atom. (f) and (h) are respective magnified views of (e) and (g) orbital-resolved projected DOS plots. The electronic states associated with the boron atom are mainly located within the deep valence band around -8 to -6 eV below the Fermi level, making it unlikely to induce significant electron density around the B atom near the Fermi level. This is consistent with Figure 4.3 where the top valence electrons are mostly delocalized across the V and O atoms instead of the B defects.

4.4.2. Extrinsic Defects in Ge-doped VO_2

Ge^{4+} can raise the MIT temperature to 90 °C,[150] close to the function operating temperatures of 80-100°C, which endows Ge-doped VO_2 with great potential in neuromorphic computing. To better control the MIT temperature and hysteresis, we combined experimental characterization and theoretical calculations to study the mechanism of Ge doping.

Our first-principles study was carried out to determine the dominant extrinsic defects associated with Ge doping. We consider three types of Ge-doping induced defects, including Ge-on-O (Ge_O) and Ge-on-V (Ge_V) substitutional defects, and interstitials (Ge_i). As shown in Figure 4.7a-b, the formation energy of Ge_V is significantly lower than Ge_O and Ge_i in both O-rich and O-poor growth conditions. It suggests that Ge_V is the dominant defects, consistent with experimental observation.

Point defects such as oxygen vacancies are known to often serve as nucleation sites of new phases in the MIT process.[149, 163] In order to investigate the impact of dominant defect Ge_V on the formation energy of oxygen vacancies (vac_O), we calculated the formation energies of vac_O with and without the presence of Ge_V (Figure 4.7c-d). When there is a single defect in the system, Ge_V is easier to form than $vac_{O,}$ due to the lower formation energy around 0 eV, especially in the O rich condition. The formation energy of the complex defect scenario, where vac_O and Ge_V exist spontaneously, is greater than Ge_V or $vac_{O,}$ and increases as the Fermi level shifts towards the conduction band, corresponding to *n*-type semiconductor. Therefore, we conclude that the formation of Ge substation defects will reduce the oxygen vacancy density. As such, the nucleation in the

phase transformation can be hindered and a greater supercooling is expected. Our theoretical findings explain a larger hysteresis width observed in the differential scanning calorimetry traces of the heating and cooling processes.

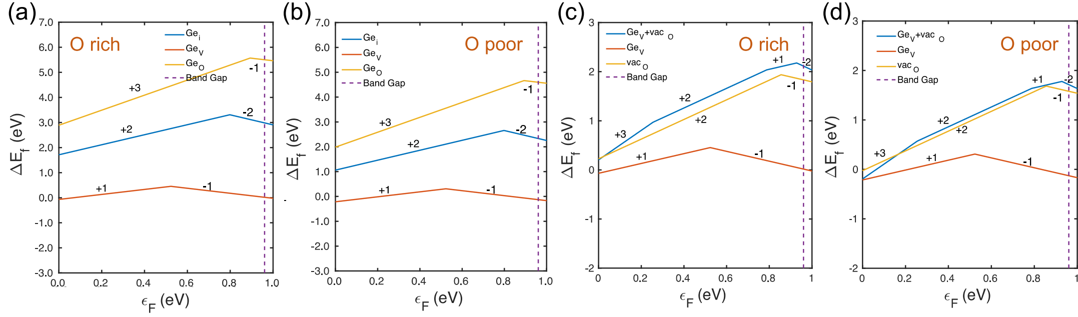

Figure 4.7. (a) and (b) Defect formation energy diagrams of Ge associated extrinsic defects under O-rich and O-poor poor growth conditions, respectively. (c) and (d) show the impact of Ge_V on the formation energy of oxygen vacancy (vac_O).

4.5. Conclusions

In summary, based on first-principles calculations, we study the electronic and magnetic properties of insulating monoclinic and metallic rutile VO_2 phases, and the native and extrinsic point defects in the monoclinic phase. By assessing the ability of different functionals for descripting the physical properties in VO_2, we reveal the challenges for PBE+U and HSE06 functionals to recover the structural, electronic, and magnetic features of M1 and R phases. Hybrid functionals such as PBE0 with more accurate exchange-correlation interaction and meta-GGA functionals such as the Strongly Constrained and Appropriately Normed (SCAN) semilocal density functional seem to outperform conventional DFT+U approach, which will be examined in future work.[167, 168]

The study of intrinsic defects of insulating VO_2 confirms that it is an *n*-type semiconductor with oxygen vacancies and vanadium interstitials as dominant defects. The extrinsic doping including boron and germanium has been investigated. Both computations and experiments demonstrate that boron dopants tend to stay at interstitial sites instead of substitutional sites in VO_2, and the dynamical diffusion of boron imbues means of dynamically modulating the MIT temperature. Finally, Ge substitutional defects will suppress the formation of oxygen vacancies, and enlarge the hysteretic width of MIT. Our first-principles study of intrinsic and extrinsic defects in VO_2 provides an approach of understanding the MIT in VO_2 and further modulating its transition temperature. Future research will continue to explore the effective methods for phase transition modulation, such as co-doping and strain engineering.

5. FERROELECTRIC AND PIEZOELECTRIC FEW-LAYER TRANSITION METAL DICHALCOGENIDES

5.1. Ferroelectric Materials for Neuro-Inspired Computing

Ferroelectricity and piezoelectricity have been recently discovered in 2D materials. Materials with such behaviors have great potential for applications in electronics, optoelectronics, and energy harvesting systems. Compared with conventional bulk materials, 2D systems have their own advantages, such as tunability, sizable bandgaps, and flexibility, which has drawn growing interest for advanced devices.[169] In this chapter, we study the van de Waals stacking induced ferroelectricity and piezoelectricity in few-layer transition metal dichalcogenides, and the potential applications in brain-inspired logic circuits and other electronic and optoelectronic devices.

The emulation of neuronal logic and memory function is the major target in neuromorphic computing. A solid state system with sharp spiking behavior is crucial for building artificial neurons and synapses. Other factors such as energy dissipation, hysteresis, and state switching magnitude during the phase transformation are also the key to the success of mimicking the brain-like behavior. Recent demonstrations show that ferroelectric materials can be utilized in neuromorphic computing and neuron network hardware, owing to its nonvolatile memory characteristic.[170, 171] The ferroelectric neurons have been applied to a variety of devices, in the form of ferroelectric transistors,[172, 173] and ferroelectric tunnel junctions.[174] One of the examples is HfO_2 based memristors, which has been demonstrated in various device structures.[175-177]

5.2. Ferroelectricity in Few-Layer WTe_2

Ferroelectric materials are a subset of materials that have spontaneous polarization, and their ferroelectric polarization can be switched upon external electric field. Despite of promising applications in non-volatile memories, the research on 2D ferroelectrics is still in infancy stage, compared to the widely used ferroelectric ceramics. Limited 2D ferroelectrics have been experimentally demonstrated, including SnTe,[178] $CuInP_2S_6$ (CIPS),[179] HfO_2,[180] ZrO_2,[181] and In_2Se_3.[182] As considerable recent attention has focused on identification of novel 2D ferroelectric materials, it is believed that many other materials with ferroelectricity will be discovered in the near future.

5.2.1. Origin of Ferroelectricity in Few-Layer WTe_2 from Group Theory

Very recently, ferroelectricity in few-layer semimetal WTe_2 has been discovered.[183-185] The experimentally measured polarization along out-of-plane direction in bilayer WTe_2 is ~1.6×10^{-2} nm μC/cm^2. In order to understand ferroelectric transition in few-layer WTe_2, previous study analyzed the origin of the spontaneous polarization from the viewpoint of group theory.[186]

As shown in Figure 5.1, monolayer 1T' WTe_2 possesses inversion symmetry (*i.e.* two-fold screw rotation symmetry C_{2y}) with C_{2h} point group. Through vdW stacking, bilayer and trilayer WTe_2 lose the inversion symmetry because the rotation axes of different layers within each layer cannot be related. Hence, multilayer WTe_2 only hold M_y symmetry. The breaking of centrosymmetry in bilayer and trilayer WTe_2 gives rise to an out-of-plane polarization.

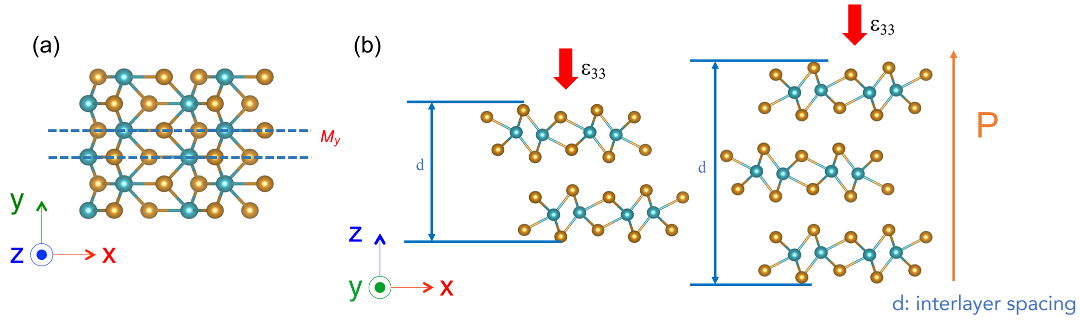

Figure 5.1. Crystal structures of few-layer 1T' WTe_2. (a) Top view of monolayer WTe_2 crystal structure with M_y mirror plane. (b) Side view of bilayer and trilayer WTe_2 crystal structure without inversion symmetry. The red arrow indicates the applied strain. The orange arrow indicates the polarization direction, which is out-of-plane. D is the interlayer spacing.

The DFT calculated electric polarization (P_z) for bilayer and trilayer WTe_2 is 1.17×10^{-2} nm μC/cm^2 and 1.02×10^{-2} nm μC/cm^2, respectively. It is within the same order of the values from previous DFT calculation[186] and experimental measurements.[169] The slight difference between our DFT results and the previous calculation by Wang and Qian implies the sensitivity of the electric polarization to the crystal structure. Note that the total polarization here is obtained by summing the ionic and electronic contributions as follows,

$$P_z = \frac{1}{A}\left(\sum_i Q_i \times (z_i - \boldsymbol{R_0}) - e\int \rho(\boldsymbol{r})(z - \boldsymbol{R_0})d^3r\right),$$

where A is the area of the unit cell, Q is the ionic charge, and ρ is the electronic charge density directly output from DFT calculations. $\boldsymbol{R_0}$ refers to the reference point, which is the origin of the unit cell in the present work. The above approach is suitable for evaluating the polarization along the out-of-plane direction of 2D materials where it is simply the vacuum. In this case, we do not need to use Berry phase approach.

5.2.2. Ferroelectric Transition in Few-Layer WTe_2

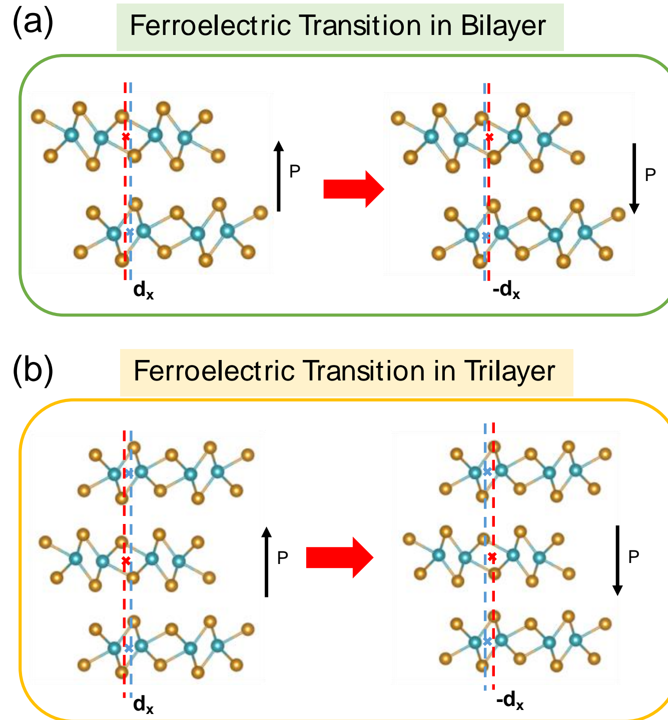

Figure 5.2. Ferroelectric transition in (a) bilayer and (b) trilayer WTe_2. The two FE states with opposite polarization direction can be transformed through interlayer sliding as indicated by the red arrow. The intermediate state with polarization vanishing appears when two dashed lines (red and blue) superimposed.

Next we analyze the ferroelectric transition pathway for bilayer and trilayer WTe_2. As shown in Figure 5.2a and b, the ferroelectric switching is induced by interlayer sliding. When the adjacent layer slides by $2d_x$, a ferroelectric state (FE) can switch to the other FE state. The intermediate paraelectric state appears at d_x=0. The transition energy profile for bilayer WTe_2 has also been calculated using NEB, where a barrier of 0.04 meV/unit cell occurs along the pathway. Considering the area and thickness of the material in the practical experiment, an energy barrier of coherent transition in the order of ~3×10^{-4}

aJ/nm^2 can be expected.[183] However, the ferroelectric phase transition in few-layer WTe_2 is likely to involve many unit cells, hence the true energy barrier for the ferroelectric phase transition can be quite different from the above value.

5.3. Piezoelectricity in Few-Layer WTe_2

5.3.1. Piezoelectricity in 2D Materials

Piezoelectricity refers to the property of electric polarization upon the applied external mechanical stress. It only occurs in the materials without inversion symmetry. Materials with piezoelectric response have potential applications in sensors, actuators, energy converters and harvesters. Generally, piezoelectricity can be considered as a coupling of mechanical and electrical behaviors described by

$$S_{ij} = d_{kij}E_k,$$

where *S* is the second rank strain tensor, *E* refers to the electric field, and *d* represents the third rank piezoelectric coefficient. Here Einstein summation convention is adopted. The indexes *i*, *j*, and *k* are corresponding to the *x*, *y*, and *z* of the Cartesian coordinates, respectively. Consequently, the electric field (or the piezoelectric polarization) can be tuned by the externally applied strain (or stress). In other words, the linear piezoelectric effect can be viewed as the coupling between the electric displacement along *i* direction (D_i) and the stress (σ_{jk}) or the strain (ϵ_{jk}) tensors. The third-rank piezoelectric tensors d_{ijk} (strain-charge form) and e_{ijk} (stress-charge form) are given by

$$d_{ijk} = \left(\frac{\partial D_i}{\partial \sigma_{jk}}\right)_E = \left(\frac{\partial \epsilon_{jk}}{\partial E_i}\right)_\sigma,$$

$$e_{ijk} = \left(\frac{\partial D_i}{\partial \epsilon_{jk}}\right)_E = -\left(\frac{\partial \sigma_{jk}}{\partial E_i}\right)_\epsilon,$$

d_{ijk} and e_{ijk} are related to each other via the elastic stiffness tensor C_{mnjk},

$$e_{ijk} = \frac{\partial D_i}{\partial \sigma_{mn}} \frac{\partial \sigma_{mn}}{\partial \epsilon_{jk}} = d_{imn} C_{mnjk.}$$

Since its discovery in 1880, many materials have been reported to exhibit piezoelectric response. Among those materials, piezoelectricity in a number of 2D materials have been theoretically predicted or experimentally demonstrated. Based on the polarization direction, we can classify the piezoelectric 2D materials to two groups: in-plane and out-of-plane piezoelectrics. Experimentally confirmed in-plane piezoelectric materials includes hexagonal transition metal dichalcogenides (h-TMDCs), hexagonal boron nitrides (h-BN), and graphene nitrides.[187, 188] There are many other in-plane piezoelectric 2D materials that have been identified from first-principles calculations, including ML group IV monochalcogenides (MX, M = Sn or Ge, X = Se or S), ML group III monochalcogenides (GaS, GaSe and InSe), ML metal dichalcogenides (MX2, M = Cr, Mo, W, Nb, Ta, and X = S, Se, Te), Group II metal oxides (MO, M= Be, Mg, Ca, Zn, Cd, Zn, Cd, Pb), and Group III-V materials (AX, A = B, Al, Ca, In and X = N, P, As, Sb).[189-191] On the other hand, the family piezoelectric 2D materials with out-of-plane polarization is much smaller. In 2018, theoretical calculations suggested that α-In_2Se_3 exhibit both in-plane and out-of-plane piezoelectricity, which was verified by experiments.[192, 193] 2D Janus TMDCs with broken out-of-plane centrosymmetry also shows giant piezoelectric effect in both in-plane and out-of-plane directions.[194] In addition to the intrinsic piezoelectricity as in all of the mentioned materials, the so-called

"extrinsic piezoelectricity" can be induced by element doping or interface interaction.[195, 196] While the piezoelectric effect has been discovered in a wide range of semiconductors and insulators, piezoelectricity in metals and semimetals remains largely underexplored. Here using first-principles DFT calculations, we demonstrate that few-layer topological semimetal WTe_2 possesses piezoelectricity due to the vdW interlayer sliding induced noncentrosymmetry.

5.3.2. Polarization Change Upon Out-of-Plane Strain

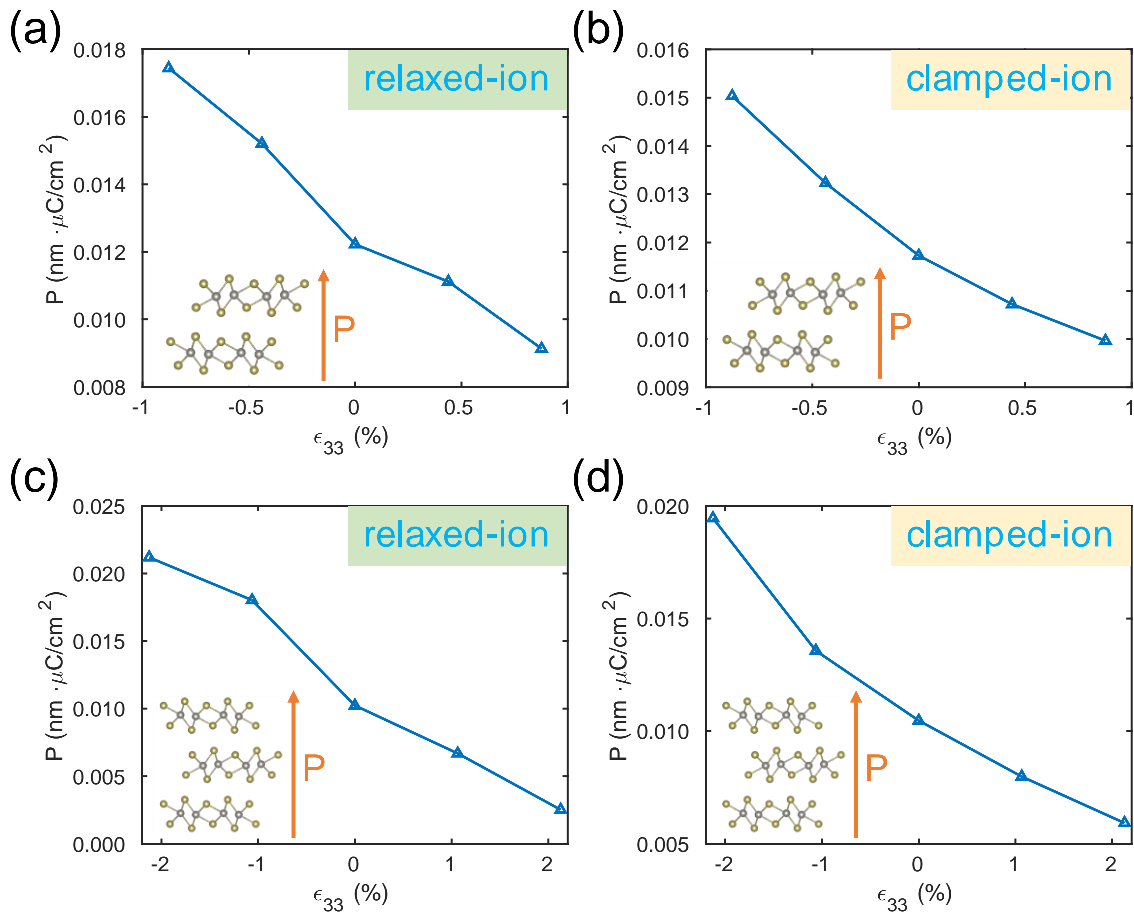

Figure 5.3. Change of out-of-plane polarization with externally applied strain. (a) and (c) Relaxed-ion case for bilayer and trilayer, respectively. (b) and (d) Clamped-ion case for bilayer and trilayer, respectively.

Table 5.1. Piezoelectric coefficient e_{33} in the unit of 10^{-12} C/m for bilayer and trilayer, respectively. It is obtained by a linear fitting of the polarization change with respect to ϵ_{33}.

Piezoelectric coefficient e_{33} (10^{-12} C/m)	Relaxed-ion	Clamped-ion
Bilayer	-0.0466	-0.0286
Trilayer	-0.0533	-0.0263

The piezoelectric effect in bilayer and trilayer WTe_2 can be reflected in the polarization change with applied out-of-plane strain. The polarization is calculated using the same approach as the one described above. The relaxed-ion case refers to the polarization with the fully relaxed structure, while the clamped-ion case is when the polarization is obtained before the structure is relaxed. As shown in Figure 5.3, both the bilayer and trilayer exhibit an out-of-plane polarization that can be generated with a compressive strain. The strain ϵ_{33} is ranging from ~$\pm 1\%$ and ~$\pm 2\%$. More interestingly, the relaxed-ion piezoelectric coefficient is larger than the clamped-ion values, which is different from 2D group-III monochalcogenides. By linear fitting of the polarization change with respect to the strain, the piezoelectric coefficients of relaxed-ion and clamped-ion cases are calculated for bilayer and trilayer structures (see Table 5.1). We further plot the total energy vs. out-of-plane displacement to confirm that our ground state configurations are indeed the most stable (Figure 5.4a and d).

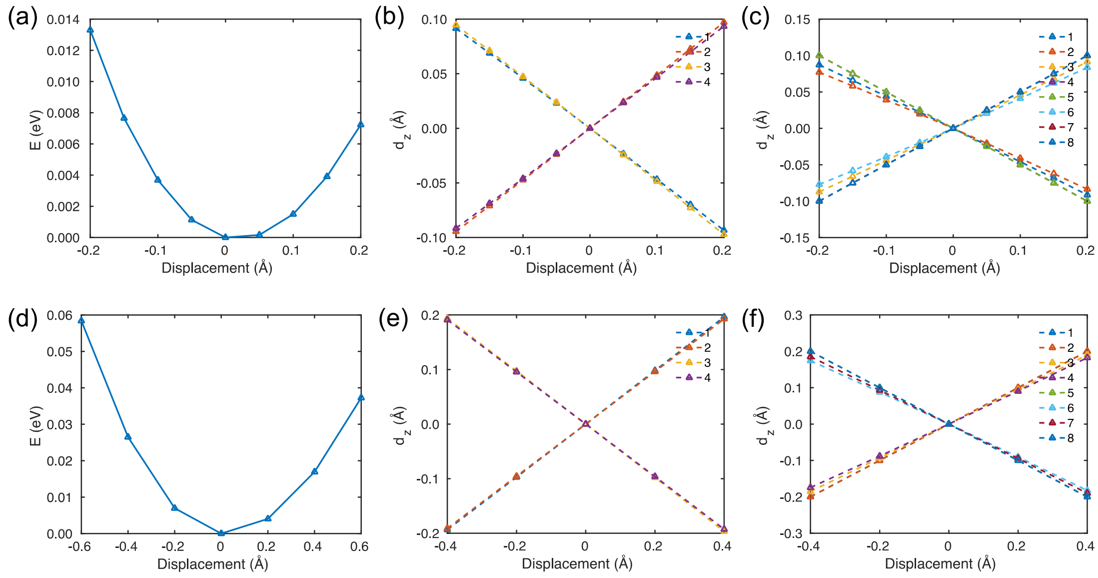

Figure 5.4. (a) Total energy of bilayer WTe_2 with respect to out-of-plane interlayer displacement. (b) Total energy of trilayer WTe_2 with respect to out-of-plane interlayer displacement. (b) and (c) Displacement of W and Te atoms along z direction for bilayer. (e) and (f) The displacement of W and Te atoms along z direction for trilayer.

To further understand the different piezoelectric behavior in the clamped-ion and relaxed-ion cases, we plot the atomic movement along z direction after atom relaxation. In our calculations, the strain is imposed by rigidly shifting the top and bottom WTe_2 layers along the +z and -z direction with equivalent distance, respectively. In the clamped-ion case, the atomic movement within the same layer is exactly the same. However, after fully relaxation by DFT, the lines possessing similar slope, shown in Figure 5.4b, c, e and f, deviate with each other, indicating the inequivalent displacement. In fact, we have found the calculated polarization is very sensitive to the atomic position in this system. Therefore, the inequivalent out-of-plane displacement (d_z) may account for the change of the piezoelectric coefficient after ion relaxation.

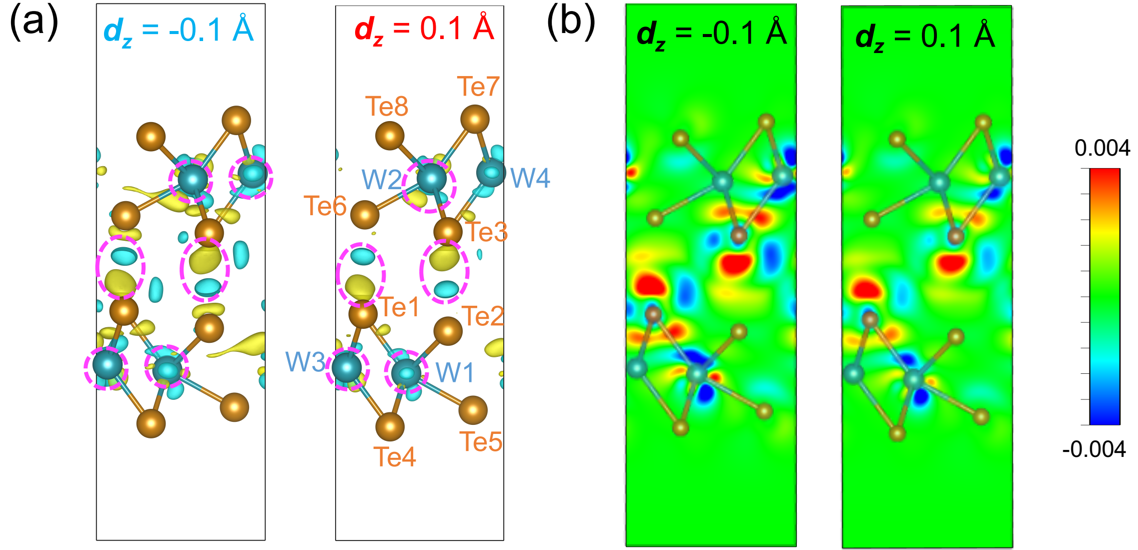

Figure 5.5. Charge redistribution analysis for bilayer WTe_2. (a) Isosurface of charge density difference when the interlayer distance along the z direction is reduced by 0.1 Å (*i.e.* displacement d_z = -0.1 Å) and increased by 0.1 Å (*i.e.* displacement d_z = 0.1 Å), respectively. The label for each atom is indicated in (a). In (a), blue indicates the charge depletion, while yellow indicates the charge accumulation. The isosurface value is 0.00025 e/Bohr^3. (b) 2D (010) cross-section of charge density difference with the displacement d_z of -0.1 and 0.1 Å along the z direction, respectively. Here the (010) plane is cutting through W1 and W3 atoms.

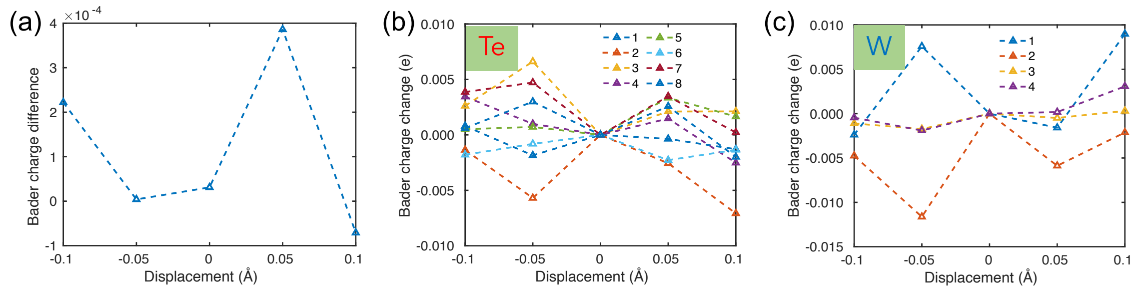

Figure 5.6. (a) Bader charge difference between top layer and bottom layer as a function of displacement. (b) The change of Bader charge as a function of the displacement of each Te atom. (c) The change of Bader charge as a function of the displacement of each W atom.

Next, we investigate the charge redistribution upon the applied strain in the bilayer case. We first study the charge transfer between the top and bottom WTe_2 layers with the decreased interlayer spacing. It is obtained by computing the charge density difference $\Delta\rho$. Here. $\Delta\rho = \rho(bilayer) - \rho(top\ layer) - \rho(bottom\ layer)$. Figure 5.5 a and b show the calculated charge density difference with the interlayer displacement of -0.1 Å along the z direction (*i.e.* upon compressive strain) and 0.1 Å (*i.e.* upon tensile strain), respectively. Figure 5.5a shows the isosurface of charge density difference, while Figure 5.5b displays a 2D (010) cross-section of charge density difference with the displacement d_z of -0.1 and 0.1 Å along the z direction, respectively. The (010) cross-section plane cuts through W1 and W3 atoms. As the interlayer spacing decreases, more charge redistribution appears. It can be explained by strong interlayer interaction due to the reduced interlayer distance. To quantitively study the charge transfer, we further conduct a Bader charge analysis.[100, 101] The Bader charge for the ground state configuration is summarized in Table 5.1. Atoms Te2 and Te6 near the interface of the bilayer structure have the largest Bader charge, showing the highest charge attraction, while their neighboring atoms W1 and W4 have the smallest Bader charge, indicating the highest charge depletion. However, there is no clear trend in the change of the Bader charge difference between the top layer and the bottom layer (Figure 5.6a) and in the charge redistribution on each atom (Figure 5.6b and c) as the strain increases. It implies that in few-layer WTe_2, the change of polarization upon the out-of-plane strain (*i.e.* the piezoelectric effect) cannot be simply attributed to charge transfer between top and bottom

layers. Rather, the piezoelectricity in few-layer WTe_2 is originated from the *local* charge redistribution, thereby inducing polarization change upon the applied strain/stress.

Table 5.2. Bader charge of each atom in the optimized bilayer WTe_2.

Label	Te	W
1	6.4593	5.0637
2	6.4740	5.0800
3	6.4560	5.0745
4	6.4660	5.0652
5	6.4623	-
6	6.4710	-
7	6.4637	-
8	6.4638	-

Finally, we also studied the interlayer sliding (d_x) induced by ϵ_{33} strain. Figure 5.7 presents the d_x as a function of strain. It shows that the out-of-plane strain results in a slight glide along the x direction. As the strain varies from negative to positive, d_x decreases, which agrees with our previous finding that P_z decreases. Additionally, within this strain range, the atomic configuration did not reach the intermediate paraelectric state or the opposite FE state, as the change of d_x is very minimal, around ~0.1 pm for both bilayer and trilayer WTe_2. This suggests that under small strain along the out-of-plane direction, the interlayer sliding is very small. Consequently, the polarization direction will not flip, e.g. transitioning into the opposite FE state.

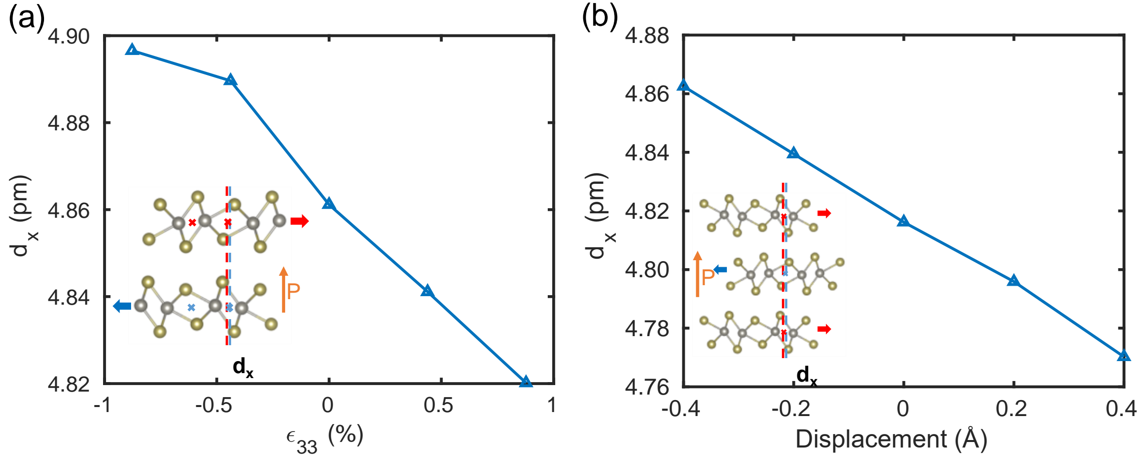

Figure 5.7. Interlayer gliding d_x along the x direction induced by out-of-plane strain in the (a) bilayer and (b) trilayer case. The inset pictures illustrate the interlayer gliding.

5.4. Conclusions and Outlook

In conclusion, we study the vdW interaction induced ferroelectricity and piezoelectricity in bilayer and trilayer 1T' WTe_2. The vdW stacking induced inversion symmetry breaking gives rise to the polarization. We have identified the two FE states with opposite polarization and calculated the transformation barrier for bilayer, which is in the order of 10^{-2} meV. More importantly, we demonstrate the piezoelectric effect in the 2D semimetals. Through a linear fitting of polarization change upon strain, we could obtain the piezoelectric coefficient for bilayer (e_{33} = -0.0466×10^{-12} C/m and -0.0286×10^{-12} C/m for relaxed-ion and clamped-ion cases) and trilayer (e_{33} = -0.0533×10^{-12} C/m and -0.0263×10^{-12} C/m for relaxed-ion and clamped-ion cases).

There are still several questions that need to be resolved in future. The present calculation only considers the *coherent* ferroelectric transition, and the corresponding energy barrier is very small. There is a great need to understand the microscopic mechanism of the ferroelectric transition in reality. For examples, how does the domain

wall structure look like? How do domain walls propagate in these vdW materials? Hence, it is worth carrying out further investigation to better understand the ferroelectric transition in few-layer TMDCs.

6. SUMMARY AND OUTLOOK

In this dissertation, we have investigated electronic structures and defect physics of photovoltaic and neuromorphic materials using first-principles methods. These materials hold great promise for the low-cost renewable energy application and efficient information technology. The first chapter highlights the need of discovery and design of novel functional materials for the development of photovoltaics and brain-inspired advance information technology. In the second chapter, a brief introduction was given regarding the first-principles study of point defects in semiconductors. In Chapter 3-4, the fundamental physical properties and defect chemistry of two emerging classes of functional materials were discussed in detail, including quasi-1D antimony chalcogenides as solar absorbers and correlated vanadium dioxides memristors as nonlinear circuit elements. Chapter 5 focuses on the study of vdW interaction induced ferroelectricity and piezoelectricity in few-layer 2D semimetal WTe_2, revealing the underlying critical role of interlayer sliding in the ferroelectric and piezoelectric effect.

Our study of antimony chalcogenides addresses three fundamental questions: (1) What is the impact of anisotropic structure and the underlying electronic structure of Sb_2X_3, e.g. exciton binding energy and dielectric screening? (2) What are intrinsic defects in Sb_2X_3 and their implications? (3) What may cause the low open circuit voltage of Sb_2X_3 solar cells? How to improve open circuit voltage and PCE? To answer those questions, we systematically investigated the atomistic and electronic structures, dielectric and optical properties, exciton dissociation and carrier transport, defect physics, and defect

concentration and carrier density of Sb_2Se_3 and Sb_2S_3. We show that antimony chalcogenides possess competing electronic structure and complex defect chemistry, that is, suitable electronic bandgaps, excellent optical absorption, and small exciton binding energy in contrast to the vacancies and antisite defects induced mid-gap states that limit the device performance. To further improve the device performance, future research should be conducted to suppress the formation of intrinsic defects by extrinsic doping, understand the role of grain boundaries and their impact on the device performance, and better control the ribbon orientation during growth.

We then presented our theoretical study of MIT in strongly correlated vanadium dioxides by first-principles electronic structure calculations. Hybrid functional PBE0 with an optimized fraction of exact exchange energy is able to provide an accurate description for structural, electronic and magnetic properties of VO_2 polymorphs. We verified the *n*-type conductivity in insulating monoclinic VO_2 by inspecting the native defects. The higher the native donor defect density is, the more conducting the insulating VO_2 will be. This originated from the higher density of donated free electrons. On the contrary, more native defects will reduce the conductivity of metallic rutile phase, because the defects can scatter or trap the free carriers. Since we aim for rational design of neuromorphic materials, we also studied the impact of element doping on the MIT mechanism. Two dopants have been studied, including boron and germanium. Our defect formation energy calculations confirm the experimental finding that boron dopants tend to stay at the interstitial sites instead of substituting vanadium atoms. Experiments further demonstrate a means of dynamically modulating the MIT temperature in B-doped VO_2. Additionally,

the combined experimental characterization and theoretical calculations demonstrated that the hysteretic width VO_2 increases upon Ge doping. This is due to the formation of Ge substitutional defects, which suppress oxygen vacancies, thereby reducing the new phase nucleation sites. The design of neuro-inspired solid-state circuits that emulate biological neuron spiking behaviors requires the deterministic control of MIT transition temperature, hysteresis width, conductance switching magnitude, and a desirably small energy dissipation. Therefore, further efforts will be made for effectively modulating the MIT in VO_2 through different approaches, such as extrinsic doping and strain engineering.

Finally, the vdW interaction induced piezoelectricity was demonstrated in few-layer WTe_2. The broken centrosymmetry in bilayer and trilayer WTe_2 and facile interlayer sliding give rise to the ferroelectric and piezoelectric behaviors. Interlayer sliding along in-plane direction plays an important role on the ferroelectric switching, and can be induced under out-of-plane stress. Our findings underline the possibility of piezoelectric response in 2D materials, although it is non-polar in monolayer and metallic along the in-plane direction. We anticipate that other layered 2D materials may exhibit similar behavior, e.g. in few-layer $MoTe_2$.

REFERENCES

[1] S. Chu, Y. Cui, and N. Liu, *The path towards sustainable energy*, Nature Materials **16**, 16 (2016).

[2] M. A. Green, and S. P. Bremner, *Energy conversion approaches and materials for high-efficiency photovoltaics*, Nature Materials **16**, 23 (2016).

[3] H. Lei, J. Chen, Z. Tan, and G. Fang, *Review of Recent Progress in Antimony Chalcogenide-Based Solar Cells: Materials and Devices*, Solar RRL **3**, 1900026 (2019).

[4] A. J. Nozik, *Quantum dot solar cells*, Physica E: Low-dimensional Systems and Nanostructures **14**, 115 (2002).

[5] D. Wöhrle, and D. Meissner, *Organic Solar Cells*, Advanced Materials **3**, 129 (1991).

[6] M. K. Nazeeruddin, E. Baranoff, and M. Grätzel, *Dye-sensitized solar cells: A brief overview*, Solar Energy **85**, 1172 (2011).

[7] J. L. Andrews, D. A. Santos, M. Meyyappan, R. S. Williams, and S. Banerjee, *Building Brain-Inspired Logic Circuits from Dynamically Switchable Transition-Metal Oxides*, Trends in Chemistry **1**, 711 (2019).

[8] S. G. Kim, J. S. Han, H. Kim, S. Y. Kim, and H. W. Jang, *Recent Advances in Memristive Materials for Artificial Synapses*, Advanced Materials Technologies **3**, 1800457 (2018).

[9] M. A. Green, Y. Hishikawa, E. D. Dunlop, D. H. Levi, J. Hohl-Ebinger, and A. W. Y. Ho-Baillie, *Solar cell efficiency tables (version 52)*, Progress in Photovoltaics: Research and Applications **26**, 427 (2018).

[10] K. Yoshikawa, H. Kawasaki, W. Yoshida, T. Irie, K. Konishi, K. Nakano, T. Uto, D. Adachi, M. Kanematsu, H. Uzu, and K. Yamamoto, *Silicon heterojunction solar cell with interdigitated back contacts for a photoconversion efficiency over 26%*, Nature Energy **2**, 17032 (2017).

[11] X. Xin, M. He, W. Han, J. Jung, and Z. Lin, *Low-Cost Copper Zinc Tin Sulfide Counter Electrodes for High-Efficiency Dye-Sensitized Solar Cells*, Angewandte Chemie International Edition **50**, 11739 (2011).

[12] T. M. Clarke, and J. R. Durrant, *Charge Photogeneration in Organic Solar Cells*, Chemical Reviews **110**, 6736 (2010).

[13] M. A. Green, A. Ho-Baillie, and H. J. Snaith, *The emergence of perovskite solar cells*, Nature Photonics **8**, 506 (2014).

[14] P. V. Kamat, *Quantum Dot Solar Cells. Semiconductor Nanocrystals as Light Harvesters*, The Journal of Physical Chemistry C **112**, 18737 (2008).

[15] R. N. Bhattacharya, and P. Pramanik, *A photoelectrochemical cell based on chemically deposited Sb_2Se_3 thin film electrode and dependence of deposition on various parameters*, Solar Energy Materials **6**, 317 (1982).

[16] O. Savadogo, and K. C. Mandal, *Studies on new chemically deposited photoconducting antimony trisulphide thin films*, Solar Energy Materials and Solar Cells **26**, 117 (1992).

[17] Y. Zhou, L. Wang, S. Chen, S. Qin, X. Liu, J. Chen, D.-J. Xue, M. Luo, Y. Cao, Y. Cheng, E. H. Sargent, and J. Tang, *Thin-film Sb_2Se_3 photovoltaics with oriented one-dimensional ribbons and benign grain boundaries*, Nature Photonics **9**, 409 (2015).

[18] L. Wang, D.-B. Li, K. Li, C. Chen, H.-X. Deng, L. Gao, Y. Zhao, F. Jiang, L. Li, F. Huang, Y. He, H. Song, G. Niu, and J. Tang, *Stable 6%-efficient Sb_2Se_3 solar cells with a ZnO buffer layer*, Nature Energy **2**, 17046 (2017).

[19] Z. Li, X. Liang, G. Li, H. Liu, H. Zhang, J. Guo, J. Chen, K. Shen, X. San, W. Yu, R. E. I. Schropp, and Y. Mai, *9.2%-efficient core-shell structured antimony selenide nanorod array solar cells*, Nature Communications **10**, 125 (2019).

[20] R. Tang, X. Wang, W. Lian, J. Huang, Q. Wei, M. Huang, Y. Yin, C. Jiang, S. Yang, G. Xing, S. Chen, C. Zhu, X. Hao, M. A. Green, and T. Chen, *Hydrothermal deposition of antimony selenosulfide thin films enables solar cells with 10% efficiency*, Nature Energy **5**, 587 (2020).

[21] N. K. Upadhyay, H. Jiang, Z. Wang, S. Asapu, Q. Xia, and J. Joshua Yang, *Emerging Memory Devices for Neuromorphic Computing*, Advanced Materials Technologies **4**, 1800589 (2019).

[22] J. v. Neumann, *First draft of a report on the EDVAC*, IEEE Annals of the History of Computing **15**, 27 (1993).

[23] M. Forshaw, R. Stadler, D. Crawley, and K. Nikoli, *A short review of nanoelectronic architectures*, Nanotechnology **15**, S220 (2004).

[24] G. Indiveri, B. Linares-Barranco, R. Legenstein, G. Deligeorgis, and T. Prodromakis, *Integration of nanoscale memristor synapses in neuromorphic computing architectures*, Nanotechnology **24**, 384010 (2013).

[25] W. Zhang, R. Mazzarello, M. Wuttig, and E. Ma, *Designing crystallization in phase-change materials for universal memory and neuro-inspired computing*, Nature Reviews Materials **4**, 150 (2019).

[26] T. Tuma, A. Pantazi, M. Le Gallo, A. Sebastian, and E. Eleftheriou, *Stochastic phase-change neurons*, Nature Nanotechnology **11**, 693 (2016).

[27] X.-B. Li, N.-K. Chen, X.-P. Wang, and H.-B. Sun, *Phase-Change Superlattice Materials toward Low Power Consumption and High Density Data Storage: Microscopic Picture, Working Principles, and Optimization*, Advanced Functional Materials **28**, 1803380 (2018).

[28] D.-H. Kwon, K. M. Kim, J. H. Jang, J. M. Jeon, M. H. Lee, G. H. Kim, X.-S. Li, G.-S. Park, B. Lee, S. Han, M. Kim, and C. S. Hwang, *Atomic structure of conducting nanofilaments in TiO_2 resistive switching memory*, Nature Nanotechnology **5**, 148 (2010).

[29] Y. Yang, and R. Huang, *Probing memristive switching in nanoionic devices*, Nature Electronics **1**, 274 (2018).

[30] M. Prezioso, F. Merrikh-Bayat, B. D. Hoskins, G. C. Adam, K. K. Likharev, and D. B. Strukov, *Training and operation of an integrated neuromorphic network based on metal-oxide memristors*, Nature **521**, 61 (2015).

[31] S. Mangin, D. Ravelosona, J. A. Katine, M. J. Carey, B. D. Terris, and E. E. Fullerton, *Current-induced magnetization reversal in nanopillars with perpendicular anisotropy*, Nature Materials **5**, 210 (2006).

[32] J. Torrejon, M. Riou, F. A. Araujo, S. Tsunegi, G. Khalsa, D. Querlioz, P. Bortolotti, V. Cros, K. Yakushiji, A. Fukushima, H. Kubota, S. Yuasa, M. D. Stiles, and

J. Grollier, *Neuromorphic computing with nanoscale spintronic oscillators*, Nature **547**, 428 (2017).

[33] C. Liu, X. Yan, X. Song, S. Ding, D. W. Zhang, and P. Zhou, *A semi-floating gate memory based on van der Waals heterostructures for quasi-non-volatile applications*, Nature Nanotechnology **13**, 404 (2018).

[34] M. Wang, S. Cai, C. Pan, C. Wang, X. Lian, Y. Zhuo, K. Xu, T. Cao, X. Pan, B. Wang, S.-J. Liang, J. J. Yang, P. Wang, and F. Miao, *Robust memristors based on layered two-dimensional materials*, Nature Electronics **1**, 130 (2018).

[35] Y. van de Burgt, A. Melianas, S. T. Keene, G. Malliaras, and A. Salleo, *Organic electronics for neuromorphic computing*, Nature Electronics **1**, 386 (2018).

[36] S. Kumar, J. P. Strachan, and R. S. Williams, *Chaotic dynamics in nanoscale NbO2 Mott memristors for analogue computing*, Nature **548**, 318 (2017).

[37] S. Kumar, Z. Wang, N. Davila, N. Kumari, K. J. Norris, X. Huang, J. P. Strachan, D. Vine, A. L. D. Kilcoyne, Y. Nishi, and R. S. Williams, *Physical origins of current and temperature controlled negative differential resistances in* NbO_2, Nature Communications **8**, 658 (2017).

[38] S.-H. Bae, S. Lee, H. Koo, L. Lin, B. H. Jo, C. Park, and Z. L. Wang, *The Memristive Properties of a Single* VO_2 *Nanowire with Switching Controlled by Self-Heating*, Advanced Materials **25**, 5098 (2013).

[39] W. Yi, K. K. Tsang, S. K. Lam, X. Bai, J. A. Crowell, and E. A. Flores, *Biological plausibility and stochasticity in scalable* VO_2 *active memristor neurons*, Nature Communications **9**, 4661 (2018).

[40] X. Yan, K. Wang, J. Zhao, Z. Zhou, H. Wang, J. Wang, L. Zhang, X. Li, Z. Xiao, Q. Zhao, Y. Pei, G. Wang, C. Qin, H. Li, J. Lou, Q. Liu, and P. Zhou, *A New Memristor with 2D* $Ti_3C_2T_x$ *MXene Flakes as an Artificial Bio-Synapse*, Small **15**, 1900107 (2019).

[41] Y. Shi, X. Liang, B. Yuan, V. Chen, H. Li, F. Hui, Z. Yu, F. Yuan, E. Pop, H. S. P. Wong, and M. Lanza, *Electronic synapses made of layered two-dimensional materials*, Nature Electronics **1**, 458 (2018).

[42] X. Zhu, D. Li, X. Liang, and W. D. Lu, *Ionic modulation and ionic coupling effects in* MoS_2 *devices for neuromorphic computing*, Nature Materials **18**, 141 (2019).

[43] K.-A. N. Duerloo, Y. Li, and E. J. Reed, *Structural phase transitions in two-dimensional Mo- and W-dichalcogenide monolayers*, Nature Communications **5**, 4214 (2014).

[44] X. Qian, J. Liu, L. Fu, and J. Li, *Quantum spin Hall effect in two-dimensional transition metal dichalcogenides*, Science **346**, 1344 (2014).

[45] S. Cho, S. Kim, J. H. Kim, J. Zhao, J. Seok, D. H. Keum, J. Baik, D.-H. Choe, K. J. Chang, K. Suenaga, S. W. Kim, Y. H. Lee, and H. Yang, *Phase patterning for ohmic homojunction contact in $MoTe_2$*, Science **349**, 625 (2015).

[46] Y. Tan, F. Luo, M. Zhu, X. Xu, Y. Ye, B. Li, G. Wang, W. Luo, X. Zheng, N. Wu, Y. Yu, S. Qin, and X.-A. Zhang, *Controllable 2H-to-1T′ phase transition in few-layer $MoTe_2$*, Nanoscale **10**, 19964 (2018).

[47] Y. Li, K.-A. N. Duerloo, K. Wauson, and E. J. Reed, *Structural semiconductor-to-semimetal phase transition in two-dimensional materials induced by electrostatic gating*, Nature Communications **7**, 10671 (2016).

[48] Y. Wang, J. Xiao, H. Zhu, Y. Li, Y. Alsaid, K. Y. Fong, Y. Zhou, S. Wang, W. Shi, Y. Wang, A. Zettl, E. J. Reed, and X. Zhang, *Structural phase transition in monolayer $MoTe_2$ driven by electrostatic doping*, Nature **550**, 487 (2017).

[49] Z. Liu, L. Deng, and B. Peng, *Ferromagnetic and ferroelectric two-dimensional materials for memory application*, Nano Research (2020).

[50] E. Yurchuk, J. Müller, J. Paul, T. Schlösser, D. Martin, R. Hoffmann, S. Müeller, S. Slesazeck, U. Schröeder, R. Boschke, R. v. Bentum, and T. Mikolajick, *Impact of Scaling on the Performance of HfO_2-Based Ferroelectric Field Effect Transistors*, IEEE Transactions on Electron Devices **61**, 3699 (2014).

[51] P. Hohenberg, and W. Kohn, *Inhomogeneous Electron Gas*, Physical Review **136**, B864 (1964).

[52] W. Kohn, and L. J. Sham, *Self-consistent equations including exchange and correlation effects*, Physical Review **140**, A1133 (1965).

[53] C. Freysoldt, B. Grabowski, T. Hickel, J. Neugebauer, G. Kresse, A. Janotti, and C. G. Van de Walle, *First-principles calculations for point defects in solids*, Reviews of Modern Physics **86**, 253 (2014).

[54] D. Broberg, B. Medasani, N. E. R. Zimmermann, G. Yu, A. Canning, M. Haranczyk, M. Asta, and G. Hautier, *PyCDT: A Python toolkit for modeling point defects in semiconductors and insulators*, Computer Physics Communications **226**, 165 (2018).

[55] M. Leslie, and N. J. Gillan, *The energy and elastic dipole tensor of defects in ionic crystals calculated by the supercell method*, Journal of Physics C: Solid State Physics **18**, 973 (1985).

[56] G. Makov, and M. C. Payne, *Periodic boundary conditions in ab initio calculations*, Physical Review B **51**, 4014 (1995).

[57] C. Freysoldt, J. Neugebauer, and C. G. Van de Walle, *Fully Ab Initio Finite-Size Corrections for Charged-Defect Supercell Calculations*, Physical Review Letters **102**, 016402 (2009).

[58] Y. Kumagai, and F. Oba, *Electrostatics-based finite-size corrections for first-principles point defect calculations*, Physical Review B **89**, 195205 (2014).

[59] F. Oba, and Y. Kumagai, *Design and exploration of semiconductors from first principles: A review of recent advances*, Applied Physics Express **11**, 060101 (2018).

[60] R. Sun, M. K. Y. Chan, S. Kang, and G. Ceder, *Intrinsic stoichiometry and oxygen-induced p-type conductivity of pyrite* FeS_2, Physical Review B **84**, 035212 (2011).

[61] M. Kumar, A. Dubey, N. Adhikari, S. Venkatesan, and Q. Qiao, *Strategic review of secondary phases, defects and defect-complexes in kesterite CZTS–Se solar cells*, Energy & Environmental Science **8**, 3134 (2015).

[62] H. S. Jung, G. S. Han, N.-G. Park, and M. J. Ko, *Flexible Perovskite Solar Cells*, Joule **3**, 1850 (2019).

[63] M. Jeong, I. W. Choi, E. M. Go, Y. Cho, M. Kim, B. Lee, S. Jeong, Y. Jo, H. W. Choi, J. Lee, J.-H. Bae, S. K. Kwak, D. S. Kim, and C. Yang, *Stable perovskite solar cells with efficiency exceeding 24.8% and 0.3-V voltage loss*, Science **369**, 1615 (2020).

[64] K. S. Kim, Y. Zhao, H. Jang, S. Y. Lee, J. M. Kim, K. S. Kim, J.-H. Ahn, P. Kim, J.-Y. Choi, and B. H. Hong, *Large-scale pattern growth of graphene films for stretchable transparent electrodes*, Nature **457**, 706 (2009).

[65] C. Chen, L. Wang, L. Gao, D. Nam, D. Li, K. Li, Y. Zhao, C. Ge, H. Cheong, H. Liu, H. Song, and J. Tang, *6.5% Certified Efficiency Sb_2Se_3 Solar Cells Using PbS Colloidal Quantum Dot Film as Hole-Transporting Layer*, ACS Energy Letters **2**, 2125 (2017).

[66] L. Guo, B. Zhang, S. Li, Q. Zhang, M. Buettner, L. Li, X. Qian, and F. Yan, *Scalable and efficient Sb_2S_3 thin-film solar cells fabricated by close space sublimation*, APL Materials **7**, 041105 (2019).

[67] L. Guo, B. Zhang, Y. Qin, D. Li, L. Li, X. Qian, and F. Yan, *Tunable Quasi-One-Dimensional Ribbon Enhanced Light Absorption in Sb_2Se_3 Thin-film Solar Cells Grown by Close-Space Sublimation*, Solar RRL **2**, 1800128 (2018).

[68] D.-B. Li, X. Yin, C. R. Grice, L. Guan, Z. Song, C. Wang, C. Chen, K. Li, A. J. Cimaroli, R. A. Awni, D. Zhao, H. Song, W. Tang, Y. Yan, and J. Tang, *Stable and efficient CdS/Sb_2Se_3 solar cells prepared by scalable close space sublimation*, Nano Energy **49**, 346 (2018).

[69] L. Guo, B. Zhang, S. Ranjit, J. Wall, S. Saurav, A. J. Hauser, G. Xing, L. Li, X. Qian, and F. Yan, *Interface Engineering via Sputtered Oxygenated CdS:O Window Layer for Highly Efficient Sb_2Se_3 Thin-Film Solar Cells with Efficiency Above 7%*, Solar RRL **3**, 1900225 (2019).

[70] X. Wen, C. Chen, S. Lu, K. Li, R. Kondrotas, Y. Zhao, W. Chen, L. Gao, C. Wang, J. Zhang, G. Niu, and J. Tang, *Vapor transport deposition of antimony selenide thin film solar cells with 7.6% efficiency*, Nature Communications **9**, 2179 (2018).

[71] H. Wedemeyer, J. Michels, R. Chmielowski, S. Bourdais, T. Muto, M. Sugiura, G. Dennler, and J. Bachmann, *Nanocrystalline solar cells with an antimony sulfide solid absorber by atomic layer deposition*, Energy & Environmental Science **6**, 67 (2013).

[72] L. Guo, B. Zhang, S. Li, A. Montgomery, L. Li, G. Xing, Q. Zhang, X. Qian, and F. Yan, *Interfacial engineering of oxygenated chemical bath–deposited CdS window layer for highly efficient Sb_2Se_3 thin-film solar cells*, Materials Today Physics **10**, 100125 (2019).

[73] Christopher N. Savory, and D. O. Scanlon, *The complex defect chemistry of antimony selenide*, Journal of Materials Chemistry A **7**, 10739 (2019).

[74] M. Huang, P. Xu, D. Han, J. Tang, and S. Chen, *Complicated and Unconventional Defect Properties of the Quasi-One-Dimensional Photovoltaic Semiconductor* Sb_2Se_3, ACS Applied Materials & Interfaces **11**, 15564 (2019).

[75] A. V. Krukau, O. A. Vydrov, A. F. Izmaylov, and G. E. Scuseria, *Influence of the exchange screening parameter on the performance of screened hybrid functionals*, The Journal of Chemical Physics **125**, 224106 (2006).

[76] S. Grimme, J. Antony, S. Ehrlich, and H. Krieg, *A consistent and accurate ab initio parametrization of density functional dispersion correction (DFT-D) for the 94 elements H-Pu*, The Journal of Chemical Physics **132**, 154104 (2010).

[77] A. Stoliaroff, A. Lecomte, O. Rubel, S. Jobic, X. Zhang, C. Latouche, and X. Rocquefelte, *Deciphering the Role of Key Defects in* Sb_2Se_3*, a Promising Candidate for Chalcogenide-Based Solar Cells*, ACS Applied Energy Materials **3**, 2496 (2020).

[78] Z. Cai, C.-M. Dai, and S. Chen, *Intrinsic Defect Limit to the Electrical Conductivity and a Two-Step p-Type Doping Strategy for Overcoming the Efficiency Bottleneck of* Sb_2S_3*-Based Solar Cells*, Solar RRL **4**, 1900503 (2020).

[79] T. D. C. Hobson, L. J. Phillips, O. S. Hutter, K. Durose, and J. D. Major, *Defect properties of* Sb_2Se_3 *thin film solar cells and bulk crystals*, Applied Physics Letters **116**, 261101 (2020).

[80] G. Kresse, and J. Furthmüller, *Efficient iterative schemes for ab initio total-energy calculations using a plane-wave basis set*, Physical Review B **54**, 11169 (1996).

[81] J. P. Perdew, K. Burke, and M. Ernzerhof, *Generalized Gradient Approximation Made Simple*, Physical Review Letters **77**, 3865 (1996).

[82] D. C. Langreth, and M. J. Mehl, *Beyond the local-density approximation in calculations of ground-state electronic properties*, Physical Review B **28**, 1809 (1983).

[83] H. J. Monkhorst, and J. D. Pack, *Special points for Brillouin-zone integrations*, Physical Review B **13**, 5188 (1976).

[84] A. D. Becke, and E. R. Johnson, *A simple effective potential for exchange*, The Journal of Chemical Physics **124**, 221101 (2006).

[85] F. Tran, and P. Blaha, *Accurate Band Gaps of Semiconductors and Insulators with a Semilocal Exchange-Correlation Potential*, Physical Review Letters **102**, 226401 (2009).

[86] A. Goyal, P. Gorai, E. S. Toberer, and V. Stevanović, *First-principles calculation of intrinsic defect chemistry and self-doping in PbTe*, npj Computational Materials **3**, 42 (2017).

[87] Y. Kumagai, N. Tsunoda, and F. Oba, *Point Defects and p-Type Doping in ScN from First Principles*, Physical Review Applied **9**, 034019 (2018).

[88] M. Dion, H. Rydberg, E. Schröder, D. C. Langreth, and B. I. Lundqvist, *Van der Waals Density Functional for General Geometries*, Physical Review Letters **92**, 246401 (2004).

[89] J. Klimeš, D. R. Bowler, and A. Michaelides, *Van der Waals density functionals applied to solids*, Physical Review B **83**, 195131 (2011).

[90] G. Román-Pérez, and J. M. Soler, *Efficient Implementation of a van der Waals Density Functional: Application to Double-Wall Carbon Nanotubes*, Physical Review Letters **103**, 096102 (2009).

[91] M. R. Filip, C. E. Patrick, and F. Giustino, *GW quasiparticle band structures of stibnite, antimonselite, bismuthinite, and guanajuatite*, Physical Review B **87**, 205125 (2013).

[92] S. Lardhi, D. Noureldine, M. Harb, A. Ziani, L. Cavallo, and K. Takanabe, *Determination of the electronic, dielectric, and optical properties of sillenite $Bi_{12}TiO_{20}$ and perovskite-like $Bi_4Ti_3O_{12}$ materials from hybrid first-principle calculations*, The Journal of Chemical Physics **144**, 134702 (2016).

[93] O. Madelung, *Semiconductors: Data Handbook* (Springer Science & Business Media, 2012).

[94] N. Tideswell, F. Kruse, and J. McCullough, *The crystal structure of antimony selenide, Sb_2Se_3*, Acta Crystallographica **10**, 99 (1957).

[95] A. Kyono, M. Kimata, M. Matsuhisa, Y. Miyashita, and K. Okamoto, *Low-temperature crystal structures of stibnite implying orbital overlap of Sb $5s^2$ inert pair electrons*, Physics and Chemistry of Minerals **29**, 254 (2002).

[96] K. F. Young, and H. P. R. Frederikse, *Compilation of the Static Dielectric Constant of Inorganic Solids*, Journal of Physical and Chemical Reference Data **2**, 313 (1973).

[97] A. Zunger, *Practical doping principles*, Applied Physics Letters **83**, 57 (2003).

[98] P. W. Anderson, *Model for the Electronic Structure of Amorphous Semiconductors*, Physical Review Letters **34**, 953 (1975).

[99] Q. Yan, A. Janotti, M. Scheffler, and C. G. Van de Walle, *Role of nitrogen vacancies in the luminescence of Mg-doped GaN*, Applied Physics Letters **100**, 142110 (2012).

[100] W. Tang, E. Sanville, and G. Henkelman, *A grid-based Bader analysis algorithm without lattice bias*, Journal of Physics: Condensed Matter **21**, 084204 (2009).

[101] R. F. W. Bader, *Atoms in Molecules*, Accounts of Chemical Research **18**, 9 (1985).

[102] Y. C. Choi, D. U. Lee, J. H. Noh, E. K. Kim, and S. I. Seok, *Highly Improved Sb_2S_3 Sensitized-Inorganic–Organic Heterojunction Solar Cells and Quantification of Traps by Deep-Level Transient Spectroscopy*, Advanced Functional Materials **24**, 3587 (2014).

[103] Y. C. Choi, and S. I. Seok, *Efficient Sb_2S_3-Sensitized Solar Cells Via Single-Step Deposition of Sb_2S_3 Using S/Sb-Ratio-Controlled $SbCl_3$-Thiourea Complex Solution*, Advanced Functional Materials **25**, 2892 (2015).

[104] N. R. Paudel, C. Xiao, A. El-Amin, R. Zartman, M. J. Heben, and Y. Yan, in *2013 IEEE 39th Photovoltaic Specialists Conference (PVSC)*2013), pp. 1161.

[105] X. Liu, X. Xiao, Y. Yang, D.-J. Xue, D.-B. Li, C. Chen, S. Lu, L. Gao, Y. He, M. C. Beard, G. Wang, S. Chen, and J. Tang, *Enhanced Sb_2Se_3 solar cell performance through theory-guided defect control*, Progress in Photovoltaics: Research and Applications **25**, 861 (2017).

[106] S. Messina, M. T. S. Nair, and P. K. Nair, *Antimony Selenide Absorber Thin Films in All-Chemically Deposited Solar Cells*, J Electrochem Soc **156**, H327 (2009).

[107] C. Chen, Y. Zhao, S. C. Lu, K. H. Li, Y. Li, B. Yang, W. H. Chen, L. Wang, D. B. Li, H. Deng, F. Yi, and J. Tang, *Accelerated Optimization of TiO_2/Sb_2Se_3 Thin Film*

Solar Cells by High-Throughput Combinatorial Approach, Adv Energy Mater **7**, 1700866 (2017).

[108] X. X. Wen, Y. S. He, C. Chen, X. S. Liu, L. Wang, B. Yang, M. Y. Leng, H. B. Song, K. Zeng, D. B. Li, K. H. Li, L. Gao, and J. Tang, *Magnetron sputtered ZnO buffer layer for Sb_2Se_3 thin film solar cells*, Solar Energy Materials and Solar Cells **172**, 74 (2017).

[109] K. Zeng, D. J. Xue, and J. Tang, *Antimony selenide thin-film solar cells*, Semicond Sci Tech **31**, 063001 (2016).

[110] L.-y. Lin, L.-q. Jiang, Y. Qiu, and B.-d. Fan, *Analysis of Sb_2Se_3/CdS based photovoltaic cell: A numerical simulation approach*, Journal of Physics and Chemistry of Solids **122**, 19 (2018).

[111] D. H. Rose, D. H. Levi, R. J. Matson, D. S. Albin, R. G. Dhere, and P. Sheldon, in *Conference Record of the Twenty Fifth IEEE Photovoltaic Specialists Conference - 1996*1996), pp. 777.

[112] T. M. Hsu, R. J. Jih, P. C. Lin, H. Y. Ueng, Y. J. Hsu, and H. L. Hwang, *Oxygen doping in close - spaced - sublimed CdTe thin films for photovoltaic cells*, Journal of Applied Physics **59**, 3607 (1986).

[113] B. Korevaar, J. R. Cournoyer, O. Sulima, A. Yakimov, and J. N. Johnson, *Role of oxygen during CdTe growth for CdTe PV devices* 2014), Vol. 22, Progress in Photovoltaics: Research and Applications.

[114] A. Gupta, K. Allada, S. H. Lee, and A. D. Compaan, *Oxygenated CdS Window Layer for Sputtered CdS/CdTe Solar Cells*, MRS Proceedings **763**, B8.9 (2003).

[115] D. M. Meysing, C. A. Wolden, M. M. Griffith, H. Mahabaduge, J. Pankow, M. O. Reese, J. M. Burst, W. L. Rance, and T. M. Barnes, *Properties of reactively sputtered oxygenated cadmium sulfide (CdS:O) and their impact on CdTe solar cell performance*, J Vac Sci Technol A **33**, 021203 (2015).

[116] J. Ge, P. Koirala, C. R. Grice, P. J. Roland, Y. Yu, X. X. Tan, R. J. Ellingson, R. W. Collins, and Y. F. Yan, *Oxygenated CdS Buffer Layers Enabling High Open-Circuit Voltages in Earth-Abundant Cu_2BaSnS_4 Thin-Film Solar Cells*, Adv Energy Mater **7**, 1601803 (2017).

[117] J. M. Kephart, R. Geisthardt, and W. S. Sampath, in *2012 38th IEEE Photovoltaic Specialists Conference*2012), pp. 000854.

[118] X. S. Liu, C. Chen, L. Wang, J. Zhong, M. Luo, J. Chen, D. J. Xue, D. B. Li, Y. Zhou, and J. Tang, *Improving the performance of Sb_2Se_3 thin film solar cells over 4% by controlled addition of oxygen during film deposition*, Prog Photovoltaics **23**, 1828 (2015).

[119] H. Metin, and R. Esen, *Annealing studies on CBD grown CdS thin films*, Journal of Crystal Growth **258**, 141 (2003).

[120] L. Wang, M. Luo, S. K. Qin, X. S. Liu, J. Chen, B. Yang, M. Y. Leng, D. J. Xue, Y. Zhou, L. Gao, H. S. Song, and J. Tang, *Ambient $CdCl_2$ treatment on CdS buffer layer for improved performance of Sb_2Se_3 thin film photovoltaics*, Applied Physics Letters **107**, 143902 (2015).

[121] N. R. Paudel, and Y. F. Yan, *Enhancing the photo-currents of CdTe thin-film solar cells in both short and long wavelength regions*, Applied Physics Letters **105** (2014).

[122] G. Henkelman, B. P. Uberuaga, and H. Jónsson, *A climbing image nudged elastic band method for finding saddle points and minimum energy paths*, The Journal of chemical physics **113**, 9901 (2000).

[123] Y. Zhou, Y. Li, J. J. Luo, D. B. Li, X. S. Liu, C. Chen, H. B. Song, J. Y. Ma, D. J. Xue, B. Yang, and J. Tang, *Buried homojunction in CdS/Sb_2Se_3 thin film photovoltaics generated by interfacial diffusion*, Applied Physics Letters **111**, 013901 (2017).

[124] W. Wang, X. Wang, G. Chen, B. Chen, H. Cai, T. Chen, S. Chen, Z. Huang, C. Zhu, and Y. Zhang, *Promising $Sb_2(S,Se)_3$ Solar Cells with High Open Voltage by Application of a TiO_2/CdS Double Buffer Layer*, Solar RRL **2**, 1800208 (2018).

[125] M. Leng, M. Luo, C. Chen, S. Qin, J. Chen, J. Zhong, and J. Tang, *Selenization of Sb_2Se_3 absorber layer: An efficient step to improve device performance of CdS/Sb_2Se_3 solar cells*, Applied Physics Letters **105**, 083905 (2014).

[126] F. Lisco, P. M. Kaminski, A. Abbas, K. Bass, J. W. Bowers, G. Claudio, M. Losurdo, and J. M. Walls, *The structural properties of CdS deposited by chemical bath deposition and pulsed direct current magnetron sputtering*, Thin Solid Films **582**, 323 (2015).

[127] V. Janošević, M. Mitrić, N. Bundaleski, Z. Rakočević, and I. L. Validžić, *High-efficiency Sb_2S_3-based hybrid solar cell at low light intensity: cell made of synthesized Cu and Se-doped Sb_2S_3*, Progress in Photovoltaics: Research and Applications **24**, 704 (2016).

[128] L. Zheng, K. Jiang, J. Huang, Y. Zhang, B. Bao, X. Zhou, H. Wang, B. Guan, L. M. Yang, and Y. Song, *Solid-state nanocrystalline solar cells with an antimony sulfide absorber deposited by an in situ solid–gas reaction*, Journal of Materials Chemistry A **5**, 4791 (2017).

[129] R. Tang, X. Wang, C. Jiang, S. Li, G. Jiang, S. Yang, C. Zhu, and T. Chen, *Vacuum assisted solution processing for highly efficient Sb_2S_3 solar cells*, Journal of Materials Chemistry A **6**, 16322 (2018).

[130] D.-H. Kim, S.-J. Lee, M. S. Park, J.-K. Kang, J. H. Heo, S. H. Im, and S.-J. Sung, *Highly reproducible planar Sb_2S_3-sensitized solar cells based on atomic layer deposition*, Nanoscale **6**, 14549 (2014).

[131] M. Imada, A. Fujimori, and Y. Tokura, *Metal-insulator transitions*, Reviews of Modern Physics **70**, 1039 (1998).

[132] F. J. Morin, *Oxides Which Show a Metal-to-Insulator Transition at the Neel Temperature*, Physical Review Letters **3**, 34 (1959).

[133] J. Jeong, N. Aetukuri, T. Graf, T. D. Schladt, M. G. Samant, and S. S. P. Parkin, *Suppression of Metal-Insulator Transition in VO_2 by Electric Field–Induced Oxygen Vacancy Formation*, Science **339**, 1402 (2013).

[134] J. H. Park, J. M. Coy, T. S. Kasirga, C. Huang, Z. Fei, S. Hunter, and D. H. Cobden, *Measurement of a solid-state triple point at the metal–insulator transition in VO_2*, Nature **500**, 431 (2013).

[135] A. Cavalleri, C. Tóth, C. W. Siders, J. A. Squier, F. Ráksi, P. Forget, and J. C. Kieffer, *Femtosecond Structural Dynamics in VO_2 during an Ultrafast Solid-Solid Phase Transition*, Physical Review Letters **87**, 237401 (2001).

[136] J. M. Longo, P. Kierkegaard, C. Ballhausen, U. Ragnarsson, S. Rasmussen, E. Sunde, and N. Sørensen, *A refinement of the structure of VO_2*, Acta Chem. Scand **24**, 420 (1970).

[137] D. B. McWhan, M. Marezio, J. P. Remeika, and P. D. Dernier, *X-ray diffraction study of metallic VO_2*, Physical Review B **10**, 490 (1974).

[138] R. E. Peierls, *Quantum Theory of Solids* (Clarendon Press, 1996).

[139] J. B. Goodenough, *The two components of the crystallographic transition in VO_2*, Journal of Solid State Chemistry **3**, 490 (1971).

[140] R. M. Wentzcovitch, W. W. Schulz, and P. B. Allen, *VO_2: Peierls or Mott-Hubbard? A view from band theory*, Physical Review Letters **72**, 3389 (1994).

[141] V. Eyert, *The metal-insulator transitions of VO_2: A band theoretical approach*, Annalen der Physik **11**, 650 (2002).

[142] A. Zylbersztejn, and N. F. Mott, *Metal-insulator transition in vanadium dioxide*, Physical Review B **11**, 4383 (1975).

[143] N. F. Mott, and L. Friedman, *Metal-insulator transitions in VO_2, Ti_2O_3 and $Ti_{2-x}V_xO_3$*, The Philosophical Magazine: A Journal of Theoretical Experimental and Applied Physics **30**, 389 (1974).

[144] T. M. Rice, H. Launois, and J. P. Pouget, *Comment on "VO_2: Peierls or Mott-Hubbard? A View from Band Theory"*, Physical Review Letters **73**, 3042 (1994).

[145] V. Eyert, *VO_2: A Novel View from Band Theory*, Physical Review Letters **107**, 016401 (2011).

[146] S. Xu, X. Shen, K. A. Hallman, R. F. Haglund, and S. T. Pantelides, *Unified band-theoretic description of structural, electronic, and magnetic properties of vanadium dioxide phases*, Physical Review B **95**, 125105 (2017).

[147] Z. Shao, X. Cao, H. Luo, and P. Jin, *Recent progress in the phase-transition mechanism and modulation of vanadium dioxide materials*, NPG Asia Materials **10**, 581 (2018).

[148] K. Liu, S. Lee, S. Yang, O. Delaire, and J. Wu, *Recent progresses on physics and applications of vanadium dioxide*, Materials Today **21**, 875 (2018).

[149] E. J. Braham, D. Sellers, E. Emmons, R. Villarreal, H. Asayesh-Ardakani, N. A. Fleer, K. E. Farley, R. Shahbazian-Yassar, R. Arròyave, P. J. Shamberger, and S.

Banerjee, *Modulating the Hysteresis of an Electronic Transition: Launching Alternative Transformation Pathways in the Metal–Insulator Transition of Vanadium(IV) Oxide*, Chemistry of Materials **30**, 214 (2018).

[150] A. Krammer, A. Magrez, W. A. Vitale, P. Mocny, P. Jeanneret, E. Guibert, H. J. Whitlow, A. M. Ionescu, and A. Schüler, *Elevated transition temperature in Ge doped VO_2 thin films*, Journal of Applied Physics **122**, 045304 (2017).

[151] M. Fiebig, K. Miyano, Y. Tomioka, and Y. Tokura, *Visualization of the Local Insulator-Metal Transition in $Pr_{0.7}Ca_{0.3}MnO_3$*, Science **280**, 1925 (1998).

[152] J. D. Budai, A. Tselev, J. Z. Tischler, E. Strelcov, A. Kolmakov, W. J. Liu, A. Gupta, and J. Narayan, *In situ X-ray microdiffraction studies inside individual VO_2 microcrystals*, Acta Materialia **61**, 2751 (2013).

[153] G. Stefanovich, A. Pergament, and D. Stefanovich, *Electrical switching and Mott transition in VO_2*, Journal of Physics: Condensed Matter **12**, 8837 (2000).

[154] M. F. Becker, A. B. Buckman, R. M. Walser, T. Lépine, P. Georges, and A. Brun, *Femtosecond laser excitation dynamics of the semiconductor‐metal phase transition in VO_2*, Journal of Applied Physics **79**, 2404 (1996).

[155] S. L. Dudarev, G. A. Botton, S. Y. Savrasov, C. J. Humphreys, and A. P. Sutton, *Electron-energy-loss spectra and the structural stability of nickel oxide: An LSDA+U study*, Physical Review B **57**, 1505 (1998).

[156] A. Liebsch, H. Ishida, and G. Bihlmayer, *Coulomb correlations and orbital polarization in the metal-insulator transition of VO_2*, Physical Review B **71**, 085109 (2005).

[157] Y. Cui, B. Liu, L. Chen, H. Luo, and Y. Gao, *Formation energies of intrinsic point defects in monoclinic VO_2 studied by first-principles calculations*, AIP Advances **6**, 105301 (2016).

[158] X. Yuan, Y. Zhang, T. A. Abtew, P. Zhang, and W. Zhang, *VO_2: Orbital competition, magnetism, and phase stability*, Physical Review B **86**, 235103 (2012).

[159] R. Grau-Crespo, H. Wang, and U. Schwingenschlögl, *Why the Heyd-Scuseria-Ernzerhof hybrid functional description of VO_2 phases is not correct*, Physical Review B **86**, 081101 (2012).

[160] W. Brückner, W. Moldenhauer, H. Wich, E. Wolf, H. Oppermann, U. Gerlach, and W. Reichelt, *The range of homogeneity of VO_2 and the influence of the composition on the physical properties. II. The change of the physical properties in the range of homogeneity*, physica status solidi (a) **29**, 63 (1975).

[161] D. Fu, K. Liu, T. Tao, K. Lo, C. Cheng, B. Liu, R. Zhang, H. A. Bechtel, and J. Wu, *Comprehensive study of the metal-insulator transition in pulsed laser deposited epitaxial VO_2 thin films*, Journal of Applied Physics **113**, 043707 (2013).

[162] H. Karl, J. Dreher, and B. Stritzker, *Semiconductor-metal phase transition in doped ion beam synthesized VO_2 nanoclusters*, MRS Online Proceedings Library **1174**, 98 (2009).

[163] W. Fan, J. Cao, J. Seidel, Y. Gu, J. W. Yim, C. Barrett, K. M. Yu, J. Ji, R. Ramesh, L. Q. Chen, and J. Wu, *Large kinetic asymmetry in the metal-insulator transition nucleated at localized and extended defects*, Physical Review B **83**, 235102 (2011).

[164] W. H. Brito, M. C. O. Aguiar, K. Haule, and G. Kotliar, *Dynamic electronic correlation effects in NbO_2 as compared to VO_2*, Physical Review B **96**, 195102 (2017).

[165] S. Mukherjee, N. F. Quackenbush, H. Paik, C. Schlueter, T. L. Lee, D. G. Schlom, L. F. J. Piper, and W.-C. Lee, *Tuning a strain-induced orbital selective Mott transition in epitaxial VO_2*, Physical Review B **93**, 241110 (2016).

[166] S. Curtarolo, W. Setyawan, G. L. W. Hart, M. Jahnatek, R. V. Chepulskii, R. H. Taylor, S. Wang, J. Xue, K. Yang, O. Levy, M. J. Mehl, H. T. Stokes, D. O. Demchenko, and D. Morgan, *AFLOW: An automatic framework for high-throughput materials discovery*, Computational Materials Science **58**, 218 (2012).

[167] I. Kylänpää, J. Balachandran, P. Ganesh, O. Heinonen, P. R. C. Kent, and J. T. Krogel, *Accuracy of ab initio electron correlation and electron densities in vanadium dioxide*, Physical Review Materials **1**, 065408 (2017).

[168] B. Stahl, and T. Bredow, *Critical Assessment of the DFT + U Approach for the Prediction of Vanadium Dioxide Properties*, Journal of Computational Chemistry **41**, 258 (2020).

[169] C. Cui, F. Xue, W.-J. Hu, and L.-J. Li, *Two-dimensional materials with piezoelectric and ferroelectric functionalities*, npj 2D Materials and Applications **2**, 18 (2018).

[170] M.-K. Kim, Y. Park, I.-J. Kim, and J.-S. Lee, *Emerging Materials for Neuromorphic Devices and Systems*, iScience **23**, 101846 (2020).

[171] S. Oh, H. Hwang, and I. K. Yoo, *Ferroelectric materials for neuromorphic computing*, APL Materials **7**, 091109 (2019).

[172] I. H. Im, S. J. Kim, and H. W. Jang, *Memristive Devices for New Computing Paradigms*, Advanced Intelligent Systems **2**, 2000105 (2020).

[173] M.-K. Kim, and J.-S. Lee, *Ferroelectric Analog Synaptic Transistors*, Nano Letters **19**, 2044 (2019).

[174] L. Chen, T.-Y. Wang, Y.-W. Dai, M.-Y. Cha, H. Zhu, Q.-Q. Sun, S.-J. Ding, P. Zhou, L. Chua, and D. W. Zhang, *Ultra-low power $Hf_{0.5}Zr_{0.5}O_2$ based ferroelectric tunnel junction synapses for hardware neural network applications*, Nanoscale **10**, 15826 (2018).

[175] G. González-Cordero, M. Pedro, J. Martin-Martinez, M. B. González, F. Jiménez-Molinos, F. Campabadal, N. Nafría, and J. B. Roldán, *Analysis of resistive switching processes in TiN/Ti/HfO_2/W devices to mimic electronic synapses in neuromorphic circuits*, Solid-State Electronics **157**, 25 (2019).

[176] E. Covi, S. Brivio, A. Serb, T. Prodromakis, M. Fanciulli, and S. Spiga, in *2016 IEEE International Symposium on Circuits and Systems (ISCAS)*2016), pp. 393.

[177] V. Milo, C. Zambelli, P. Olivo, E. Pérez, M. K. Mahadevaiah, O. G. Ossorio, C. Wenger, and D. Ielmini, *Multilevel HfO_2-based RRAM devices for low-power neuromorphic networks*, APL Materials **7**, 081120 (2019).

[178] K. Chang, J. Liu, H. Lin, N. Wang, K. Zhao, A. Zhang, F. Jin, Y. Zhong, X. Hu, W. Duan, Q. Zhang, L. Fu, Q.-K. Xue, X. Chen, and S.-H. Ji, *Discovery of robust in-plane ferroelectricity in atomic-thick SnTe*, Science **353**, 274 (2016).

[179] F. Liu, L. You, K. L. Seyler, X. Li, P. Yu, J. Lin, X. Wang, J. Zhou, H. Wang, H. He, S. T. Pantelides, W. Zhou, P. Sharma, X. Xu, P. M. Ajayan, J. Wang, and Z. Liu, *Room-temperature ferroelectricity in $CuInP_2S_6$ ultrathin flakes*, Nature Communications **7**, 12357 (2016).

[180] T. S. Böscke, J. Müller, D. Bräuhaus, U. Schröder, and U. Böttger, *Ferroelectricity in hafnium oxide thin films*, Applied Physics Letters **99**, 102903 (2011).

[181] J. Müller, T. S. Böscke, U. Schröder, S. Mueller, D. Bräuhaus, U. Böttger, L. Frey, and T. Mikolajick, *Ferroelectricity in Simple Binary ZrO_2 and HfO_2*, Nano Letters **12**, 4318 (2012).

[182] C. Zheng, L. Yu, L. Zhu, J. L. Collins, D. Kim, Y. Lou, C. Xu, M. Li, Z. Wei, Y. Zhang, M. T. Edmonds, S. Li, J. Seidel, Y. Zhu, J. Z. Liu, W.-X. Tang, and M. S. Fuhrer, *Room temperature in-plane ferroelectricity in van der Waals In_2Se_3*, Science Advances **4**, eaar7720 (2018).

[183] J. Xiao, Y. Wang, H. Wang, C. D. Pemmaraju, S. Wang, P. Muscher, E. J. Sie, C. M. Nyby, T. P. Devereaux, X. Qian, X. Zhang, and A. M. Lindenberg, *Berry curvature memory through electrically driven stacking transitions*, Nature Physics **16**, 1028 (2020).

[184] Q. Yang, M. Wu, and J. Li, *Origin of Two-Dimensional Vertical Ferroelectricity in WTe_2 Bilayer and Multilayer*, The Journal of Physical Chemistry Letters **9**, 7160 (2018).

[185] Z. Fei, W. Zhao, T. A. Palomaki, B. Sun, M. K. Miller, Z. Zhao, J. Yan, X. Xu, and D. H. Cobden, *Ferroelectric switching of a two-dimensional metal*, Nature **560**, 336 (2018).

[186] H. Wang, and X. Qian, *Ferroelectric nonlinear anomalous Hall effect in few-layer WTe 2*, npj Computational Materials **5**, 119 (2019).

[187] K.-A. N. Duerloo, M. T. Ong, and E. J. Reed, *Intrinsic Piezoelectricity in Two-Dimensional Materials*, The Journal of Physical Chemistry Letters **3**, 2871 (2012).

[188] M. Zelisko, Y. Hanlumyuang, S. Yang, Y. Liu, C. Lei, J. Li, P. M. Ajayan, and P. Sharma, *Anomalous piezoelectricity in two-dimensional graphene nitride nanosheets*, Nature Communications **5**, 4284 (2014).

[189] W. Li, and J. Li, *Piezoelectricity in two-dimensional group-III monochalcogenides*, Nano Research **8**, 3796 (2015).

[190] R. Fei, W. Li, J. Li, and L. Yang, *Giant piezoelectricity of monolayer group IV monochalcogenides: SnSe, SnS, GeSe, and GeS*, Applied Physics Letters **107**, 173104 (2015).

[191] M. N. Blonsky, H. L. Zhuang, A. K. Singh, and R. G. Hennig, *Ab Initio Prediction of Piezoelectricity in Two-Dimensional Materials*, ACS Nano **9**, 9885 (2015).

[192] F. Xue, J. Zhang, W. Hu, W.-T. Hsu, A. Han, S.-F. Leung, J.-K. Huang, Y. Wan, S. Liu, J. Zhang, J.-H. He, W.-H. Chang, Z. L. Wang, X. Zhang, and L.-J. Li, *Multidirection Piezoelectricity in Mono- and Multilayered Hexagonal α-*In_2Se_3, ACS Nano **12**, 4976 (2018).

[193] Y. Zhou, D. Wu, Y. Zhu, Y. Cho, Q. He, X. Yang, K. Herrera, Z. Chu, Y. Han, M. C. Downer, H. Peng, and K. Lai, *Out-of-Plane Piezoelectricity and Ferroelectricity in Layered α-*In_2Se_3 *Nanoflakes*, Nano Letters **17**, 5508 (2017).

[194] L. Dong, J. Lou, and V. B. Shenoy, *Large In-Plane and Vertical Piezoelectricity in Janus Transition Metal Dichalchogenides*, ACS Nano **11**, 8242 (2017).

[195] G. da Cunha Rodrigues, P. Zelenovskiy, K. Romanyuk, S. Luchkin, Y. Kopelevich, and A. Kholkin, *Strong piezoelectricity in single-layer graphene deposited on SiO2 grating substrates*, Nature Communications **6**, 7572 (2015).

[196] H.-J. Jin, W. Y. Yoon, and W. Jo, *Virtual Out-of-Plane Piezoelectric Response in* MoS_2 *Layers Controlled by Ferroelectric Polarization*, ACS Applied Materials & Interfaces **10**, 1334 (2018).